

**IMPROVING THE PERFORMANCE OF PRECISE POINT
POSITIONING WITH MULTI-GNSS**

**ÇOKLU-GNSS İLE HASSAS NOKTA KONUMLAMA
PERFORMANSININ İYİLEŞTİRİLMESİ**

BERKAY BAHADUR

Asst. Prof. Dr. METİN NOHUTCU

Supervisor

Submitted to Graduate School of Science and Engineering of Hacettepe University
as a Partial Fulfilment to the Requirements
for the Award of the Degree Master of Science
in Geomatics Engineering

2017

This work named ”Improving the Performance of Precise Point Positioning with Multi-GNSS” by BERKAY BAHADUR has been approved as a thesis for the Degree of **MASTER OF SCIENCE IN GEOMATICS ENGINEERING** by the below mentioned Examining Committee Members.

Prof. Dr. Mustafa TÜRKER

Head

Asst. Prof. Dr. Metin NOHUTCU

Supervisor

Assoc. Prof. Dr. Aydın ÜSTÜN

Member

Assoc. Prof. Dr. Sultan KOCAMAN

Member

Asst. Prof. Dr. Kamil TEKE

Member

This thesis has been approved as a thesis for the Degree of **MASTER OF SCIENCE IN GEOMATICS ENGINEERING** by Board of Directors of the Institute for Graduate School of Science and Engineering.

Prof. Dr. Menemşe GÜMÜŞDERELİOĞLU

Director of the Institute of

Graduate School of Science and Engineering

YAYINLAMA VE FİKRİ MÜLKİYET HAKLARI BEYANI

Enstitü tarafından onaylanan lisansüstü tezimin/raporumun tamamını veya herhangi bir kısmını, basılı (kağıt) ve elektronik formatta arşivleme ve aşağıda verilen koşullarla kullanıma açma iznini Hacettepe üniversitesine verdiğimi bildiririm. Bu izinle Üniversiteye verilen kullanım hakları dışındaki tüm fikri mülkiyet haklarım bende kalacak, tezimin tamamının ya da bir bölümünün gelecekteki çalışmalarda (makale, kitap, lisans ve patent vb.) kullanım hakları bana ait olacaktır.

Tezin kendi orijinal çalışmam olduğunu, başkalarının haklarını ihlal etmediğimi ve tezimin tek yetkili sahibi olduğumu beyan ve taahhüt ederim. Tezimde yer alan telif hakkı bulunan ve sahiplerinden yazılı izin alınarak kullanması zorunlu metinlerin yazılı izin alarak kullandığımı ve istenildiğinde suretlerini Üniversiteye teslim etmeyi taahhüt ederim.

Tezimin/Raporumun tamamı dünya çapında erişime açılabilir ve bir kısmı veya tamamının fotokopisi alınabilir.

(Bu seçenekle teziniz arama motorlarında indekslenebilecek, daha sonra tezinizin erişim statüsünün değiştirilmesini talep etmeniz ve kütüphane bu talebinizi yerine getirirse bile, tezinin arama motorlarının önbelleklerinde kalmaya devam edebilecektir.)

Tezimin/Raporumun tarihine kadar erişime açılmasını ve fotokopi alınmasını (İç Kapak, Özet, İçindekiler ve Kaynakça hariç) istemiyorum.

(Bu sürenin sonunda uzatma için başvuruda bulunmadığım takdirde, tezimin/raporumun tamamı her yerden erişime açılabilir, kaynak gösterilmek şartıyla bir kısmı ve ya tamamının fotokopisi alınabilir)

Tezimin/Raporumun tarihine kadar erişime açılmasını istemiyorum, ancak kaynak gösterilmek şartıyla bir kısmı veya tamamının fotokopisinin alınmasını onaylıyorum.

Serbest Seçenek/Yazarın Seçimi

16/06/2017



Berkay Bahadır

ETHICS

In this thesis study, prepared in accordance with the spelling rules of Institute of Graduate Studies in Science of Hacettepe University,

I declare that

- all the information and documents have been obtained in the base of the academic rules
- all audio-visual and written information and results have been presented according to the rules of scientific ethics
- in case of using others Works, related studies have been cited in accordance with the scientific standards
- all cited studies have been fully referenced
- I did not do any distortion in the data set
- and any part of this thesis has not been presented as another thesis study at this or any other university.

16/06/2017



BERKAY BAHADUR

ABSTRACT

IMPROVING THE PERFORMANCE OF PRECISE POINT POSITIONING WITH MULTI-GNSS

Berkay BAHADUR

Master of Science, Department of Geomatics Engineering

Supervisor: Asst. Prof. Dr. Metin NOHUTCU

June 2017, 97 pages

Precise Point Positioning (PPP) is the positioning technique which enables centimetre-level positioning accuracy with only one receiver in static mode. The main strength of PPP lies behind the employment of precise orbit and clock products acquired from a global network. Over the past ten years, PPP has been a popular topic within the Global Navigation Satellite Systems (GNSS) community and widely used in a range of GNSS applications, such as precise surveying, atmospheric monitoring and modelling, aerial triangulation, geohazard monitoring, etc. However, long initial time which is required to converge an optimal solution is still the main restriction of PPP. In recent years, the emergence of new navigation systems has offered the prospect of overcoming the limitation of PPP. The combination of multi-GNSS provides additional satellite resources for satellite navigation and positioning. Therefore, the combination of multi-GNSS makes it possible to improve the satellite geometry and to increase the number of visible satellites. Nevertheless, the combination of multi-GNSS entails new modelling approaches and more complex processing strategies. The principal objective of this study is to investigate the influence of multi-GNSS on PPP performance. For this purpose, the multi-GNSS approach containing both the functional and stochastic models were presented, and some improvements were introduced to optimize the implementation of the Kalman filter on PPP. Furthermore, a PPP software package, named PPPH, was developed to evaluate the performance of multi-GNSS. PPPH was designed to perform multi-GNSS PPP solution, which includes the observations from GPS, GLONASS, Galileo, and BeiDou. Further, PPPH enables to specify modelling and filtering options and also includes several tools to analyse the results. A comparison between PPPH and online PPP services was performed to validate PPPH's

results. It was confirmed that PPPH provides centimetre-level positioning accuracy in static mode and convergence time is similar to the solutions obtained from online PPP services. The influence of multi-GNSS on PPP performance was investigated in terms of positioning accuracy and convergence time. The results showed that the GPS/GLONASS PPP and the multi-GNSS PPP improves the positioning accuracy at the rate of 16.2% and 21.6%, respectively in relative to GPS-only PPP. On the other hand, the GPS/GLONASS PPP and multi-GNSS PPP was reduced the convergence time obtained from GPS-only PPP by 28.1% and 33.2%, respectively.

Keywords: Precise Point Positioning (PPP), Multi-GNSS, Convergence Time, Kalman Filter, MATLAB

ÖZET

ÇOKLU GNSS İLE HASSAS NOKTA KONUMLAMA PERFORMANSININ İYİLEŞTİRİLMESİ

Berkay BAHADUR

Yüksek Lisans, Geomatik Mühendisliği Bölümü

Tez Danışmanı: Yrd. Doç. Dr. Metin NOHUTCU

Haziran 2017, 97 sayfa

Hassas Nokta Konumlama (PPP), yalnızca bir alıcı kullanarak statik modda santimetre seviyesinde doğruluk sağlayabilen konum belirleme tekniğidir. Global bir ağdan elde edilen hassas yörünge ve saat ürünlerinin kullanılması bu tekniği güçlü kılan en büyük etkidir. PPP, GNSS kullanıcıları arasında son on senedir popüler bir konu olmuştur ve hassas ölçmeler, atmosferin izlenmesi ve modellenmesi, hava triyagülasyonu, yer kaynaklı tehlikelerin izlenmesi gibi bir çok alanda yaygın olarak kullanılmaktadır. Ancak, optimum sonuca ulaşmak için gereken uzun başlangıç süresi hala PPP'nin en büyük kısıtıdır. Son dönemlerde yeni navigasyon sistemlerinin ortaya çıkması bu kısıtların ortadan kaldırılması için iyi bir fırsat sunmaktadır. Çoklu-GNSS kombinasyonu uydu navigasyonu ve konumlaması için ek uydu kaynağı sağlamaktadır. Buna bağlı olarak, Çoklu-GNSS kombinasyonu uydu geometrisini iyileştirmeyi ve görünür uydu sayısını arttırmayı mümkün kılar. Bununla birlikte, çoklu-GNSS kombinasyonu yeni modelleme yaklaşımları ve daha karmaşık işleme stratejilerini gerektirir. Bu çalışmanın öncelikli amacı çoklu-GNSS kombinasyonunun PPP üzerindeki etkisini araştırmaktır. Bu amaçla, fonksiyonel and stokastik modelleri içeren çoklu-GNSS yaklaşımı sunulmuş ve Kalman filtresinin PPP uygulamasını geliştirmek için bazı iyileştirmeler yapılmıştır. Ek olarak, çoklu-GNSS'in PPP performansına olan etkisini araştırmak için PPPH adında bir yazılım geliştirilmiştir. Bu yazılım, GPS, GLONASS, Galileo ve BDS gözlemlerini içeren çoklu-GNSS PPP çözümünü gerçekleştirmek üzere tasarlanmıştır. Dahası, PPPH kullanıcılara modelleme ve filtreleme seçeneklerini belirleme imkanı sağlar ve ek olarak sonuçları analiz etmek için bir çok araca sahiptir. PPPH yazılımının sonuçlarını doğrulamak için PPPH ve online PPP servisleri arasında bir karşılaştırma yapılmıştır. Bu analizlerin sonucunda, PPPH'in statik modda santimetre seviyesinde konum doğruluğu sağladığı ve online PPP servislerine benzer yakınsama süresine ulaştığı

görülmüştür. Ayrıca, çoklu-GNSS analizinin PPP üzerine olan etkisi doğruluk ve yakınsama süresi açısından incelenmiştir. Sonuçlar, GPS/GLONASS PPP ve çoklu-GNSS PPP çözümlerinin GPS PPP çözümüne göre konum doğruluğunu sırasıyla %16,2 ve %21,6 iyileştirdiğini göstermiştir. Diğer taraftan, GPS/GLONASS PPP ve çoklu-GNSS PPP, GPS PPP ile elde edilen yakınsama sürelerini sırasıyla %28,1 ve %33,2 azaltmıştır.

Keywords: Hassas Nokta Konumlama (PPP), Çoklu-GNSS, Yakınsama Süresi, Kalman Filtresi, MATLAB

ACKNOWLEDGEMENTS

First of all, I would like to express my great gratitude to my supervisor, Asst. Prof. Dr. Metin Nohutcu, for his guidance, support and encouragement during the period of my graduate study. At every stage of this thesis, he supported me with his knowledge, experience, and motivation by showing patience and tolerance.

I would like to thank my thesis committee members, Prof. Dr. Mustafa Türker, Assoc. Prof. Dr. Aydın Üstün, Assoc. Prof. Dr. Sultan Kocaman and Asst. Prof. Dr. Kamil Teke for their valuable contributions and advice.

I would like to extend my thanks to all colleagues at the Department of Geomatics Engineering for their support.

Finally, a special thank goes to my wife, Özge, for her endless support and tolerance throughout this thesis. I also would like to thank my family for their unconditional love and support.

CONTENTS

	<u>Page</u>
ABSTRACT	i
ÖZET	iii
ACKNOWLEDGEMENTS	v
CONTENTS	vi
LIST OF TABLES	ix
LIST OF FIGURES	xi
1 INTRODUCTION	1
1.1 Background	1
1.2 Research Objectives	2
1.3 Thesis Outline	3
2 GNSS OVERVIEW	5
2.1 GNSS System Descriptions	5
2.1.1 GPS	5
2.1.2 GLONASS	7
2.1.3 GALILEO	8
2.1.4 BEIDOU	9
2.1.5 Comparison of GNSS	10
2.2 GNSS Observations	12
2.2.1 Code Pseudorange	13
2.2.2 Carrier Phase	14
2.3 Linear Combinations of GNSS Observations	15
2.3.1 Ionosphere-free Combination	15
2.3.2 Geometry-free Combination	16
2.3.3 Wide-lane Combination	16
2.3.4 Narrow-lane Combination	17
2.3.5 Melbourne-Wübbena Combination	17

2.4	GNSS Positioning with Single Receiver	18
2.4.1	Absolute Point Positioning	18
2.4.2	Precise Point Positioning	18
3	PPP ERROR SOURCES AND THEIR MITIGATION STRATEGIES	20
3.1	Satellite Orbit and Clock	20
3.2	Receiver Clock	23
3.3	Troposphere	25
3.4	Ionosphere	28
3.5	Relativistic Effects	29
3.6	Antenna Phase Center	30
3.7	Phase Wind-up	32
3.8	Solid Earth Tide	32
3.9	Ocean Loading	34
3.10	Polar Tide	34
3.11	Differential Code Biases	35
3.12	Cycle Slips	35
3.13	Summary	39
4	TRADITIONAL AND MULTI-GNSS PPP APPROACHES	40
4.1	Extended Kalman Filter	41
4.2	Traditional PPP Approach	44
4.2.1	Functional Model	44
4.2.2	Stochastic Modelling	47
4.2.3	Quality Control	49
4.3	Multi-GNSS PPP Approach	51
4.3.1	Functional Model	52
4.3.2	Stochastic Modelling	54
4.3.3	Quality Control	56
4.4	Further Improvements	56
4.4.1	Adaptive Robust Kalman Filter	57
4.4.2	Initialisation of Kalman Filter	58
5	SOFTWARE DEVELOPMENT	60
5.1	Data Importing	60
5.2	Preprocessing	62
5.3	Modelling Options	63
5.4	Filtering Options	64
5.5	Analysis	65

6	TESTS AND RESULTS	70
6.1	Data Description	70
6.2	Validating the Positioning Performance of PPPH	71
6.3	Integrating Multi-GNSS to Improve the PPP Performance	78
6.4	Initialization of Kalman Filter using Least Squares Adjustment	83
7	CONCLUSIONS	86
7.1	Conclusions	86
7.2	Recommendations	88
	REFERENCES	89
	CURRICULUM VITAE	96

LIST OF TABLES

2.1	The essential specifications of the carrier frequencies employed in GPS.	6
2.2	GLONASS slot and frequency channel numbers.	8
2.3	The basic features of Galileo signals.	9
2.4	The basic specifications of BDS signals.	10
2.5	The main features of GNSS.	11
2.6	Ellipsoidal parameters of GNSS reference frames.	12
3.1	Standard IGS satellite orbit and clock products.	21
3.2	A list of MGEX products.	22
3.3	Types of clock jumps.	24
3.4	The parameters required for computing coefficient c of the GMF dry mapping function	28
3.5	PPP error sources, their mitigation strategies and possible effects on line of sight direction.	39
4.1	GPS observation noise levels	48
4.2	Stochastic properties of the estimated parameter for traditional PPP approach	50
5.1	Corrections and handling strategies provided by the modelling sections of PPPH.	64
6.1	Daily average Kp indices of the days between 10-14 May and 2-6 June 2015.	71
6.2	Ten days positioning errors of six stations obtained from PPPH estimates at the end of 24 hours processing	73
6.3	Agencies and URLs of online PPP processing services.	74
6.4	Main processing strategies of PPPH, GAPS, CSRS-PPP	75
6.5	Five days averaged PPP results for PPPH, GAPS and CSRS-PPP (May 10-14, 2015).	77
6.6	Five days averaged PPP results for PPPH, GAPS and CSRS-PPP (June 2-6, 2015).	77
6.7	Positioning error comparison of different system combinations.	82
6.8	Convergence time comparison of different system combinations.	83

6.9	Average values of positioning errors and convergence times acquired from PPP processes initialized with standard parameters and least squares adjustment	85
-----	--	----

LIST OF FIGURES

2.1	GPS constellation	6
2.2	Determination of signal travel time	13
3.1	IGS multi-GNSS stations	21
3.2	The code and carrier observations of PRN02 satellite on L1 signal during the first day of 2017 at ZWE2 station.	23
3.3	W differences for the observations obtained from the PRN2 satellite on the L1 signal during the first day of 2017 at ZWE2 station.	25
3.4	GNSS satellite orientation in nominal yaw-steering mode	30
3.5	Simulation of cycle slip based on the values of additional cycles on L1 and L2 frequencies $n_1 = 77, n_2 = 60$	38
3.6	Simulation of cycle slip based on the values of additional cycles on L1 and L2 frequencies $n_1 = 10, n_2 = 10$	38
4.1	The complete EKF process steps.	44
5.1	Data importing section of PPPH GUI.	61
5.2	Preprocessing section of PPPH GUI.	62
5.3	Modelling options section of PPPH GUI.	63
5.4	Filtering options section of PPPH GUI.	65
5.5	Analysis section of PPPH GUI.	66
5.6	Examples of the positioning error plots generated by PPPH.	67
5.7	Examples of additional plots generated by PPPH.	68
5.8	The flowchart of PPPH processing.	69
6.1	Distribution of IGS reference stations used in this study.	70
6.2	Ten days convergence times of each station obtained from PPPH estimates.	72
6.3	Average numbers of visible satellites of different system combinations during the days between 2-6 June 2015.	78
6.4	Visible satellite distribution for GNSS at station NNOR on 2 June 2015.	79
6.5	Average PDOP factors for different system combinations.	80
6.6	Five days averaged 3D positioning errors for different system combinations.	81
6.7	Five days averaged convergence times for different system combinations.	81

6.8	3D positioning errors for different system combinations during the day 2 June 2015 at station NNOR.	84
-----	--	----

1. INTRODUCTION

1.1. Background

For a long time, the differential and/or relative positioning techniques have dominated the Global Navigation Satellite Systems (GNSS) industry. These techniques provide highly accurate positioning solutions using reference points with known coordinates to eliminate most of GNSS observation errors. By definition, at least two or more receivers (one reference and one rover) are required to achieve high positioning accuracy in differential (or relative) techniques. There is no doubt that it raises the operational cost and system complexity. Additionally, positioning accuracy is closely dependent on the distance from reference station or regional network, which means that the relative or differential techniques can efficiently work in a limited area. In recent years, Precise Point Positioning (PPP) has emerged as an alternative precise positioning method. PPP enables centimetre-level positioning accuracy with only one receiver. The main strength of PPP is to employ the precise products to eliminate satellite-related clock and orbit errors. In addition, the ionosphere-free linear combination is utilized to mitigate the atmospheric effect caused by the ionosphere layer in traditional PPP process[1, 2].

Over the past ten years, PPP has taken a considerable attention within the GNSS community due to its benefits such as operational simplicity, cost effectiveness, the requirement of no base station, etc. Consequently, PPP has been a standard positioning method for a range of GNSS applications, such as atmospheric monitoring and modelling, aerial triangulation, geohazard monitoring, kinematic positioning [3, 4, 5, 6, 7, 8, 9]. Although PPP satisfies the positioning accuracy demands of most the GNSS applications, the initialization period required to converge centimetre-level positioning accuracy is quite long relative to differential positioning techniques. Over the last decade, much effort has been made to shorten the convergence period of PPP with the ambiguity resolution methods. The ambiguity resolution methods are pretty successful to reduce the convergence time, but these methods can be applied only if external corrections, which are mainly obtained from a network, are available. This approach is typically named ambiguity-fixed solution and requires a service provider to obtain the related corrections [10, 11, 12, 13, 14, 15]. Alternatively, the combination of different GNSS constellations presents the opportunity to enhance the positioning and convergence performance of PPP. The emergence of multi-GNSS provides additional

satellite resources and strengthens satellite geometry. The combination of multi-GNSS has a considerable potential to improve PPP performance since the quality of PPP technique closely depends on the geometry and number of visible satellites.

First studies on the combination of multi-GNSS observations mainly focused on the integration of Global Positioning System (GPS) and Russian Global Navigation Satellite System (GLONASS). These studies have confirmed that GPS/GLONASS PPP improves positioning accuracy and convergence time relative to traditional PPP approach which includes only GPS satellites [16, 17, 18]. In addition, the emergence of other navigation systems such as the Chinese navigation system BeiDou (BDS) and the European Galileo system (Galileo) makes the multi-GNSS PPP including four constellations possible. Recently, some researchers have investigated the impact of combined quad-constellation observations on PPP performance. Initial results have shown that multi-GNSS PPP, which includes quad-constellations, significantly improves the performance of traditional PPP. [19, 20]. Nevertheless, if modernization plans of GPS and GLONASS, ongoing development of Galileo and BDS, and new orbit and products are taken into consideration, it is clear that multi-GNSS PPP still requires further investigation and confirmation in terms of the improvement of performance.

1.2. Research Objectives

The combination of multi-GNSS offers an enormous potential for enhancing PPP performance by providing additional satellite resources to strengthen both number and geometry of visible satellites. Therefore, multi-GNSS PPP has taken considerable attention within GNSS community in recent years. The principal goal of this thesis is to examine the influence of combined multi-GNSS on PPP performance as regards the accuracy, precision and convergence time.

Traditional PPP technique is designed to employ only GPS observations. Therefore, traditional PPP models do not satisfy the requirement of combined multi-GNSS PPP. To assure interoperability of satellite systems, new functional and stochastic models, which reflect discrepancies between the systems like coordinate system definition, time reference scale, observation and product quality, etc., are needed to be introduced. At first, the multi-GNSS PPP approach including both functional and stochastic models should be presented and improved to meet the main objective.

At the same time, multi-GNSS PPP demands special PPP software package, which is capable of providing the solution to the combination of multi-GNSS. However, there

is not enough PPP software package options to meet this demand within the GNSS community. As well, existing software, mostly developed by universities or research institutes, have limited access to the functional and stochastic models and are not open to being progressed. For this reason, the other objective of this thesis is to develop a user-friendly PPP software package, which enables to provide multi-GNSS PPP solutions. Also, it is possible to interfere each step of PPP processing and to test the impact of combined multi-GNSS on PPP performance, independently.

Finally, experimental tests, of course, should be conducted to investigate the compatibility of the PPP software package developed in this study with other software packages and the impact of combined multi-GNSS and improved models on PPP performance.

1.3. Thesis Outline

This study contains seven chapters. First describes the background, research objectives and outline of the thesis.

Chapter 2 briefly explains GPS, GLONASS, Galileo, and BDS and makes a comprehensive comparison between these systems. Additionally, GNSS observations and their linear combinations are described in this chapter. Finally, GNSS positioning techniques with a single receiver are given.

Chapter 3 defines the possible error sources of traditional and multi-GNSS approaches. Also, mitigation strategies of these error sources are comprehensively discussed in this chapter.

Chapter 4 firstly gives the mathematical description of the extended Kalman filter. The functional and stochastic models of traditional and also multi-GNSS PPP approaches are presented. Additionally, this chapter introduces further improvements in the Kalman filter estimation.

Chapter 5 introduces the PPP software package developed in this study. Data importing, preprocessing, modelling options, filtering options and analysis components of the software are described in detail.

Chapter 6 starts with the description of data to employed in experimental tests. A validation test is conducted to compare the PPP software developed in this study with other software packages and their results are presented in this chapter. Additionally, the performance evaluation of multi-GNSS PPP is given. Finally, the effectiveness of

the innovative method for initializing Kalman filter is tested in this chapter.

Chapter 7 presents the conclusions drawn from this study and some recommendations for future work.

2. GNSS OVERVIEW

This chapter presents a brief introduction to GNSS, namely GPS, GLONASS, Galileo, and BeiDou. Then, a comprehensive comparison between these systems is drawn in terms of reference time scales and coordinate systems. Finally, GNSS observations and linear combinations of these observations, which are essential for the GNSS techniques, are presented.

2.1. GNSS System Descriptions

GNSS are the global satellite-based navigation, positioning and time transfer systems. There are four major GNSS currently: GPS developed by the US Department of Defense (DoD), GLONASS controlled by the Ministry of Defense of the Russian Federation, Galileo maintained by European Space Agency (ESA) and BDS operated by the China National Space Administration.

Nowadays, only GPS and GLONASS provide global coverage for positioning and navigation. However, Galileo and BDS have been under development and will be fully operational in near future.

2.1.1. GPS

GPS is the first satellite-based navigation and positioning system to reach full operational capability. GPS space segment is composed of a satellite constellation transmitting radio signals for navigation and positioning purposes. GPS constellation nominally has 24 satellites orbiting around the Earth and also the satellites are equally aligned on six orbital planes which have approximately 20200 kilometre altitude from the Earth. Furthermore, the orbital planes are split from each other with a 55° inclination in Earth's equatorial plane (Figure 2.1). Temporal resolution or orbital period of GPS satellites is approximately 11 hours 58 minutes, i.e. they revolve the Earth twice in a sidereal day. The design of GPS constellation ensures global coverage and minimum four satellites which is needed for navigation purposes are visible anywhere on the world. GPS currently has 31 operational satellites [21].

GPS satellites utilize code division multiple access (CDMA) method, which employs

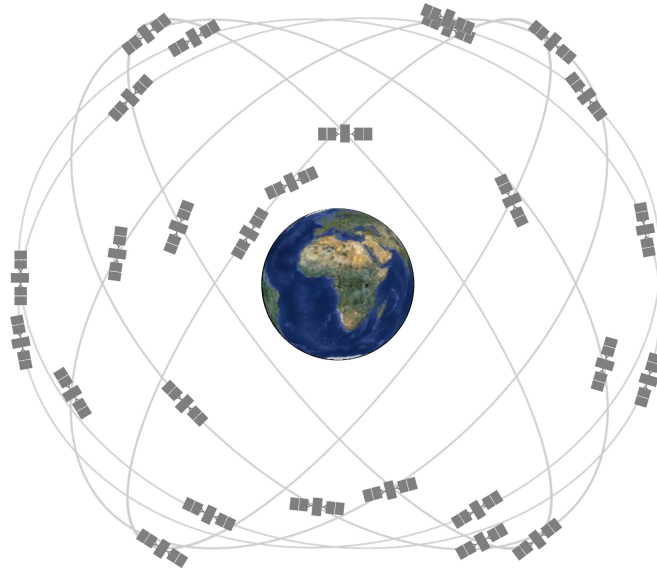


Figure 2.1: GPS constellation [21].

standard navigation signals modulated on same carrier frequencies for all satellites, to generate their navigation signals. CDMA technique allows receivers to distinguish GPS satellites from each other by means of different sets of codes transmitted by each satellite. On the other hand, GPS navigation signals are produced by multiplying a fundamental frequency ($f_0 = 10.23$ MHz) with different coefficients. The carrier frequencies employed in GPS are right-handed circularly polarized and are designed to transmit modulated codes as well as navigation messages. Basically, GPS frequencies include three modulated codes, which are the coarse acquisition code (C/A), precision code (P) and navigation message (D). While L1 frequency carries both C/A and P-codes, L2 frequency delivers only P-code to GPS users. Table 2.1 shows the essential specifications of the carrier frequencies employed in GPS.

Table 2.1: The essential specifications of the carrier frequencies employed in GPS.

Signal	Factor (f_0)	Frequency (MHz)	Wavelength (cm)
L1	154	1575.42	19.0
L2	120	1227.60	24.4
L5	115	1176.45	25.5

GPS modernization project began in 2005 with the launch of the new generation satellites (Block IIR-M). The project contains an additional carrier frequency (L5) and several new ranging codes (L2C, L5C, L1C and M). It is aimed at providing better signal quality, satellite visibility and positioning performance to users by means of the modernized GPS. Similarly, improved compensation for ionospheric delays, additional

wide-lane signal combinations for ambiguity resolution and the interoperability between different constellations are some improvements coming with the modernization. It is scheduled that 24 GPS satellites transmitting L5 will be in orbit by 2020 [22].

2.1.2. GLONASS

GLONASS reached full operational capability with the full orbital constellation in 2011. The constellation includes twenty-four satellites in three orbital planes. There is a 120° inclination between the orbital planes and Earth's equatorial plane. The orbital height of GLONASS satellites is about 19130 kilometres for which the orbital period approximately corresponds 11 hours 16 minutes. The GLONASS architecture is designed to ensure that the users anywhere in the world can receive transmitting signals from at least four visible satellites.

GLONASS satellites transmit right-handed circularly polarized signals for navigation and positioning purposes. As GLONASS utilizes two different frequencies modulated on L-band similar to GPS, the frequencies employed in GLONASS will be referred as G1 and G2 to prevent misconception in this study. Furthermore, the carrier frequencies of GLONASS involve two modulated codes, namely the coarse acquisition code (C/A) only on G1 and precision code (P) on G1 and G2. Also, GLONASS satellites transmit, of course, navigation messages including the satellite position and clock information.

The signals transmitted by GLONASS satellites are akin to the other GNSS signals, however, there is a little difference between GLONASS and other systems. Basically, GLONASS utilizes frequency division multiple access (FDMA) technique in which every satellite broadcasts navigation signals on the particular frequency. Although every satellite employs distinct frequency, the whole GLONASS satellites transmit standard ranging codes (C/A and P) in navigation signals. The formal values of the G1 and G2 frequencies are demonstrated by:

$$f_1^k = f_1^b + k \Delta f_1 \quad (2.1)$$

$$f_2^k = f_2^b + k \Delta f_2 \quad (2.2)$$

where k is the frequency channel number of corresponding satellite and the constants are $f_1^b = 1602$ MHz, $\Delta f_1 = 0.5625$ MHz, $f_2^b = 1246$ MHz and $\Delta f_2 = 0.4375$ MHz. The rate of frequencies, f_2^k/f_1^k , is constant for all GLONASS satellites and equals 7/9. GLONASS satellites launched after 2005 are using frequency channels $k = -7, \dots, +6$ [23]. Table 2.2 shows the frequency channel numbers of GLONASS satellites.

Table 2.2: GLONASS slot and frequency channel numbers.

Plane/Slot	1/01	1/02	1/03	1/04	1/05	1/06	1/07	1/08
Frequency Chan.	+1	-4	+5	+6	+1	-4	+5	+6

Plane/Slot	2/09	2/10	2/11	2/12	2/13	2/14	2/15	2/16
Frequency Chan.	-2	-7	0	-1	-2	-7	0	-1

Plane/Slot	3/17	3/18	3/19	3/20	3/21	3/22	3/23	3/24
Frequency Chan.	+4	-3	+3	+2	+4	-3	+3	+2

As a part of GLONASS modernization plan, the new CDMA signals will be transmitted by new generation satellites (GLONASS-K2)[23].

2.1.3. GALILEO

Galileo is the global satellite-based system which is developed by European Space Agency (ESA) for navigation and positioning purposes. The first four Galileo satellites were launched in pairs on 21 October 2011, and 12 October 2012, respectively. Space and ground-based components of the system underwent validation tests and Orbit Validation step was successfully completed at the end of 2013. As of March 2017, ten Galileo satellites is available for navigation purposes. The new satellite launches are planned to complete the constellation and to reach full operational capability by 2020 [24].

The full Galileo constellation will be composed of twenty-four satellites which have a 23222 kilometres altitude from Earth surface. The orbital period of Galileo satellites is approximately 14 hours. Galileo satellites are equally distributed in 3 orbital planes separated from each other with a 56° inclination in Earth's equatorial plane. Galileo is designed to ensure global coverage, that is at least four satellites will be visible at any point on the world when reaching full operational capability.

The Galileo navigation signals, which are right-handed circularly polarized, are transmitted in the four frequency bands. These frequencies are obtained from a fundamental frequency ($f_0 = 10.23$ MHz). Also, ten navigation signals which provide several services to satisfy various user requirements are delivered by these carrier frequencies. Galileo navigation services are the Open Service (OS), Public Regulated Service (PRS), and

Commercial Service (CS), respectively. OS can be globally used by GNSS users free of charge, while PRS is designed for only security authorities. Also, CS provides two additional signals for commercial purposes. The fundamental features of Galileo carrier frequencies are summarized in Table 2.3. As in GPS, all Galileo satellites make use of the same set of carrier frequencies. Thus, the signals are characterized by their spread spectrum using the CDMA technique [24].

Table 2.3: The basic features of Galileo signals.

Signal	Factor (f_0)	Frequency (MHz)	Wavelength (cm)	Services
E1	154	1575.42	19.0	OS, PRS, CS
E5a	115	1176.45	25.5	OS
E5b	118	1207.14	24.8	OS, CS
E6	125	1278.75	23.4	PRS, CS

2.1.4. BEIDOU

China started to test a satellite-based navigation system called BeiDou (BDS) in 2000. Thereby, China became the third country in the world able to develop such a system independently after the United States and Russia. In accordance with the construction plan, BeiDou has begun to provide services in Asia-Pacific region since December 2012. Nowadays, BDS has been under development and will be fully operational by around 2020 [25].

When fully deployed, BDS constellation will include five Geostationary Earth Orbit (GEO) satellites, twenty-seven Medium Earth Orbit (MEO) satellites and three Inclined Geosynchronous Satellite Orbit (IGSO) satellites. MEO satellites are running in orbit with 21528 kilometres altitude from the Earth surface. Twenty-four MEO satellites are going to be aligned in three orbital planes equally with a 55° inclination to Earth's equatorial plane and three additional satellites will be sparse ones. Akin to the other satellite-based navigation systems, BDS system design guarantees at least four visible satellites required for navigation purposes anywhere on the world when the system reaches full operational capability.

BeiDou satellites broadcast right-handed circularly polarized signals referred as B1 and B2 bands. These bands provide two services for navigation purposes: Open Service

(OS) and Authorised Service (AS). While all BDS users can access OS free of charge, authorized users only make use of AS service. As like GPS and Galileo, BDS utilizes navigation signals obtained from CDMA technique. The basic specifications of BeiDou signals are given in Table Table 2.4 [26].

Table 2.4: The basic specifications of BDS signals.

Signal	Frequency (MHz)	Wavelength (cm)	Code	Service
B1	1561.098	19.2	B1-I	Open
			B1-Q	Authorized
B2	1207.14	24.8	B2-I	Open
			B2-Q	Authorized
B3	1268.52	23.6	B3	Authorized

2.1.5. Comparison of GNSS

As mentioned previously, GPS, GLONASS, Galileo, and BDS are principally comparable systems, but there are still some discrepancies between them. Certain important features of navigation systems are summarized in Table 2.5 as including the main differences.

GPS, GLONASS, Galileo and BDS have their own atomic time scales. These time scales are different realizations of Coordinated Universal Time (UTC). GPS Time was fixed to suit UTC at 0^h 6 January 1980, so it constantly has 19 seconds offset from International Atomic Time (TAI).

On the other hand, GLONASS Time is synchronous with UTC as including three hours constant offset which reflects the time difference between Greenwich and Moscow. Apart from the constant offset, the time difference of GLONASS from UTC does not exceed 1 ms and is transmitted by navigation signals.

Galileo System Time (GST) was fixed to UTC at 0^h 22 August 1999 (Midnight between 21 and 22 August), so it was ahead of UTC by 13 leap seconds at its start epoch. Furthermore, three additional leap seconds have been introduced on December 31, 2005, and 2008, and June 30, 2012. Therefore, the constant difference between GST and UTC is 16 seconds. The Galileo navigation message includes all necessary parameters to convert GST to UTC [24]. Finally, BeiDou System Time (BDT) was started at 0^h

Table 2.5: The main features of GNSS.

	GPS	GLONASS	GALILEO	BEIDOU
Satellite number	24	24	30	27
Orbital plane	6	3	3	3
Orbital radius (km)	26508	25510	29601	27878
Inclination of orbital planes	55°	64.8°	56°	55°
Orbital period (approximately)	11 ^h 58 ^m	11 ^h 16 ^m	14 ^h 04 ^m	12 ^h 53 ^m
Signal separation technique	CDMA	FDMA	CDMA	CDMA
Carrier frequencies (MHz)	1575.42	1602 + $k * 0.5626$	1575.42	1561.098
	1227.60	1246 + $k * 0.4375$	1176.45	1207.14
	1176.45		1207.14	1268.52
			1278.75	
Coordinate system	WGS-84	PZ-90	GTRF	CGCS
Time scale	GPS Time	GLONASS Time	GST	BDT

UTC on 1 January 2006. Consequently, there is a regular difference between BDT and TAI, which equals 33 seconds. [26].

Each system utilizes an individual Earth-Centered Earth-Fixed (ECEF) reference frame based on a different ellipsoid. GPS uses the World Geodetic System 1984 (WGS-84) as reference ellipsoid and the origin of the coordinate system is Earth’s center of mass. The X-axis coincides with the IERS Reference Meridian (IRM). The Z-axis points to the direction of the IERS Reference Pole (IRP) and the Y-axis completes a right-handed, orthogonal coordinate system [27].

GLONASS adopts the PZ-90 as reference ellipsoid and the origin of the coordinate system is located at Earth’s center of mass. The X-axis is directed to the point of intersection of the Earth’s equatorial plane and the zero meridian established by Bureau International de l’Heure (BIH). The Z-axis points to IRP and the Y-axis completes a right-handed coordinate system [23].

Galileo utilizes the Galileo Terrestrial Reference System (GTRF) which complies with the definition of International Terrestrial Reference Frame (ITRF). GTRF shall be

agreeable with latest ITRF version within three centimetres precision level. This is ensured by Galileo Geodetic Service Provider (GGSP) [28].

BDS utilizes China Coordinate System 2000 (CGCS2000) as reference frame. Earth's center of mass is the origin of CGCS2000 and the X-axis points to IRM. Also, the Z-axis is directed to IRP and the Y-axis constitutes a right-handed coordinate system. Fundamental ellipsoidal parameters of these reference frames is given in Table 2.6.

Table 2.6: Ellipsoidal parameters of GNSS reference frames.

Ellipsoid	Semi-major axis (m)	Flattening	Angular velocity (rad/s)	Gravitational constant (m^3/s^2)
WGS-84	6378137.0	1/298.257223563	$792115.0 * 10^{-11}$	$3986004.418 * 10^8$
PZ-90	6378136.0	1/298.257839303	$792115.0 * 10^{-11}$	$3986004.400 * 10^8$
GTRF	6378137.0	1/298.257222101	$792115.0 * 10^{-11}$	$3986004.418 * 10^8$
CGCS	6378137.0	1/298.257222101	$792115.0 * 10^{-11}$	$3986004.418 * 10^8$

The time and coordinate system discrepancies between GNSS should be taken into account in combined multi-GNSS solutions. The parameters which are necessary to establish a proper relationship between the systems can be obtained from the navigation messages. Moreover, code and phase measurements of GLONASS includes more biases caused by the usage of FDMA method. Consequently, the orbit and clock offsets can be calculated separately for each system taking these parameters into consideration. Alternatively, GNSS ephemeris data and clock offsets can be directly estimated in the same reference frame. As a part of the IGS Multi-GNSS Experiment (MGEX), some agencies produce and broadcast the GNSS ephemeris products in the same reference frame [29]. In this case, it is not necessary to carry out any transformations, but the inter-system biases still must be considered.

2.2. GNSS Observations

The basic GNSS observations are code pseudorange deduced from transit time for the signal and carrier phase based on phase differences between received and receiver-generated signals. The satellite-based navigation methods make use of highly precise atomic clocks together with phase oscillators to obtain measurements. Both observations are basically described below.

2.2.1. Code Pseudorange

The code pseudoranges are obtained by measuring GNSS signal transit time between satellite and receiver. It refers to the distance between the phase center of satellite antenna at signal transmission time and the phase center of the receiver at signal reception time. Transit time is measured as the time shift which gives maximum correlation between the received and receiver-generated signals Figure 2.2.

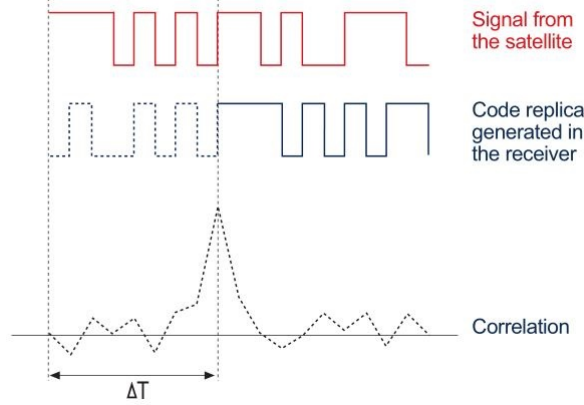


Figure 2.2: Determination of signal travel time [30].

Code observable is known as *pseudorange*, because it considerably deviates from the geometric range due to the lack of clock synchronization between satellite and receiver as well as atmospheric influences on the signal transmission. GNSS pseudorange observations are written as:

$$P_{i,r}^{s,j} = \rho_r^{s,j} + c dt_r^s - c dt^{s,j} + T_r^{s,j} + \frac{I}{f_i^2} + b_{P_{i,r}}^s - b_{P_i}^{s,j} + \varepsilon(P_{i,r}^{s,j}) \quad (2.3)$$

where subscript i and r indicate the frequency index of navigation signal and receiver, respectively; superscript s and j indicate the GNSS system (G: GPS, R: GLONASS, E: GALILEO or C: BDS) and satellite number. The other terms in Equation (2.3) are as follows:

$\rho_r^{s,j}$	geometric range between satellite and receiver
c	speed of the light in vacuum
dt_r^s	receiver clock error
$dt^{s,j}$	satellite clock error
$T_r^{s,j}$	tropospheric delay
I/f_i^2	first-order ionospheric delay
$b_{P_{i,r}}^s$	receiver code hardware delay
$b_{P_i}^{s,j}$	satellite code hardware delay
$\varepsilon(P_{i,r}^{s,j})$	multipath and code noise

2.2.2. Carrier Phase

The carrier phase observation refers to the measurement reflecting the phase difference between received satellite signal and receiver-generated signal. Nevertheless, this measurement includes only fractional part of the carrier waves. The number of full carrier waves, that is the unknown integer number of cycles for the first lock of a receiver to signal, is not a part of the carrier phase measurement and called as ambiguity. The fractional part can be determined with millimetre precision, however, the integer part of the cycles is still unknown. If ambiguity is resolved successfully, the carrier phase measurement can be precisely obtained. Apart from ambiguity, carrier phase measurement includes other effects similar to code pseudorange.

GNSS carrier phase observations are written as:

$$L_{i,r}^{s,j} = \rho_r^{s,j} + c dt_r^s - c dt^{s,j} + T_r^{s,j} - \frac{I}{f_i^2} + \lambda_i^s N_i^{s,j} + b_{L_{i,r}}^s - b_{L_i}^{s,j} + \varepsilon(L_{i,r}^{s,j}) \quad (2.4)$$

where λ_i^s is the wavelength of corresponding frequency, $N_i^{s,j}$ denotes the integer number of full cycles (ambiguity), $b_{L_{i,r}}^s$ and $b_{L_i}^{s,j}$ indicate the receiver phase hardware bias and the satellite phase hardware bias, respectively. It should be mentioned that the ionosphere has different influences on code and phase observations due to the nature of propagation. The reason for this will be detailed in the next chapters. The rest of the terms in Equation (2.4) were mentioned previously.

2.3. Linear Combinations of GNSS Observations

Linear combinations can be formed by combining different GNSS observations measured with the same receiver at the same station. Some GNSS problems can be easily solved by means of the linear combinations. The general way of forming a linear combination is given by

$$P_{LC}^{s,j} = \alpha P_{1,r}^{s,j} + \beta P_{2,r}^{s,j} \quad L_{LC}^{s,j} = \alpha L_{1,r}^{s,j} + \beta L_{2,r}^{s,j} \quad (2.5)$$

where α and β are the combination coefficients, P and L denotes code and carrier observable, respectively. The essential GNSS linear combinations are given in subsequent sub-chapters.

2.3.1. Ionosphere-free Combination

This combination is called as *ionospheric-free* since it removes the first order ionospheric effect which constitutes up to 99.9 percent of the ionospheric effects on GNSS observations [31]. The coefficients of ionosphere-free combination are given by:

$$\alpha_{IF} = \frac{f_1^2}{f_1^2 - f_2^2} \quad \beta_{IF} = -\frac{f_2^2}{f_1^2 - f_2^2}. \quad (2.6)$$

The equations of ionosphere-free combinations for code and phase observations are given by:

$$P_{3,r}^{s,j} = \rho_r^{s,j} + c dt_r^s - c dt^{s,j} + T_r^{s,j} + b_{P_{3,r}}^s - b_{P_3}^{s,j} + \varepsilon(P_{3,r}^{s,j}) \quad (2.7)$$

$$L_{3,r}^{s,j} = \rho_r^{s,j} + c dt_r^s - c dt^{s,j} + T_r^{s,j} + \lambda_3^s N_3^{s,j} + b_{L_{3,r}}^s - b_{L_3}^{s,j} + \varepsilon(L_{3,r}^{s,j}) \quad (2.8)$$

where subscript 3 indicates the ionosphere-free combination, $\varepsilon(P_{3,r}^{s,j})$ and $\varepsilon(L_{3,r}^{s,j})$ denotes the ionosphere-free code noise and phase noise, respectively. Other terms are given below.

$$b_{P_{3,r}}^s = \alpha_{IF} b_{P_{1,r}}^s + \beta_{IF} b_{P_{2,r}}^s \quad b_{P_3}^{s,j} = \alpha_{IF} b_{P_1}^{s,j} + \beta_{IF} b_{P_2}^{s,j} \quad (2.9)$$

$$b_{L_{3,r}}^s = \alpha_{IF} b_{L_{1,r}}^s + \beta_{IF} b_{L_{2,r}}^s \quad b_{L_3}^{s,j} = \alpha_{IF} b_{L_1}^{s,j} + \beta_{IF} b_{L_2}^{s,j} \quad (2.10)$$

$$\lambda_3^s N_3^{s,j} = \alpha_{IF} \lambda_1^s N_1^{s,j} + \beta_{IF} \lambda_2^s N_2^{s,j} \quad (2.11)$$

2.3.2. Geometry-free Combination

The geometry-free combination eliminates the whole geometry-dependent effects on GNSS observations and leaves only the frequency-dependent term. The geometry-free combinations can be formed as [31]:

$$P_{4,r}^{s,j} = P_{2,r}^{s,j} - P_{1,r}^{s,j} \quad L_{4,r} = L_{1,r}^{s,j} - L_{2,r}^{s,j} \quad (2.12)$$

$$P_{4,r}^{s,j} = I_4 + b_{P_{4,r}}^s - b_{P_4}^{s,j} + \varepsilon(P_{4,r}^{s,j}) \quad (2.13)$$

$$L_{4,r}^{s,j} = -I_4 + \lambda_4^s N_4^{s,j} + b_{L_{4,r}}^s - b_{L_4}^{s,j} + \varepsilon(L_{4,r}^{s,j}) \quad (2.14)$$

where subscript 4 indicates the geometry-free combination, $\varepsilon(P_{4,r}^{s,j})$ and $\varepsilon(L_{4,r}^{s,j})$ denotes the geometry-free code noise and phase noise, respectively. Other terms are given below.

$$b_{P_{4,r}}^s = b_{P_{2,r}}^s - b_{P_{1,r}}^s \quad b_{P_4}^{s,j} = b_{P_2}^{s,j} - b_{P_1}^{s,j} \quad (2.15)$$

$$b_{L_{4,r}}^s = b_{L_{1,r}}^s - b_{L_{2,r}}^s \quad b_{L_4}^{s,j} = b_{L_1}^{s,j} - b_{L_2}^{s,j} \quad (2.16)$$

$$\lambda_4^s N_4^{s,j} = \lambda_1^s N_1^{s,j} - \lambda_2^s N_2^{s,j} \quad I_4 = \frac{f_1^2 - f_2^2}{f_1^2 \cdot f_2^2} I \quad (2.17)$$

2.3.3. Wide-lane Combination

The wide-lane combination, as is evident from its name, is used for forming an observation which has the wider wavelength. The coefficients of wide-lane combination are given as [30]:

$$\alpha_{WL} = \frac{f_1}{f_1 - f_2} \quad \beta_{WL} = -\frac{f_2}{f_1 - f_2}. \quad (2.18)$$

The equations of wide-lane combinations for code and phase observations are written as follows:

$$P_{5,r}^{s,j} = \rho_r^{s,j} + c dt_r^s - c dt_r^{s,j} + T_r^{s,j} + I_5 + b_{P_{5,r}}^s - b_{P_5}^{s,j} + \varepsilon(P_{5,r}^{s,j}) \quad (2.19)$$

$$L_{5,r}^{s,j} = \rho_r^{s,j} + c dt_r^s - c dt_r^{s,j} + T_r^{s,j} - I_5 + \lambda_5^s N_5^{s,j} + b_{L_{5,r}}^s - b_{L_5}^{s,j} + \varepsilon(L_{5,r}^{s,j}) \quad (2.20)$$

where subscript 5 indicates the wide-lane combination, $\varepsilon(P_{5,r}^{s,j})$ and $\varepsilon(L_{5,r}^{s,j})$ denotes the wide-lane code noise and phase noise, respectively. Other terms are given below.

$$b_{P_{5,r}}^s = \alpha_{WL} b_{P_{1,r}}^s + \beta_{WL} b_{P_{2,r}}^s \quad b_{P_5}^{s,j} = \alpha_{WL} b_{P_1}^{s,j} + \beta_{WL} b_{P_2}^{s,j} \quad (2.21)$$

$$b_{L_{5,r}}^s = \alpha_{WL} b_{L_{1,r}}^s + \beta_{WL} b_{L_{2,r}}^s \quad b_{L_5}^{s,j} = \alpha_{WL} b_{L_1}^{s,j} + \beta_{WL} b_{L_2}^{s,j} \quad (2.22)$$

$$I_5 = -\frac{I}{f_1 \cdot f_2} \quad \lambda_5^s N_5^{s,j} = \alpha_{WL} \lambda_1^s N_1^{s,j} + \beta_{WL} \lambda_2^s N_2^{s,j} \quad (2.23)$$

2.3.4. Narrow-lane Combination

This combination is used to form a measurement with a considerably narrow wavelength. The coefficients of the narrow-lane combination are given as [30]:

$$\alpha_{NL} = \frac{f_1}{f_1 + f_2} \quad \beta_{NL} = \frac{f_2}{f_1 + f_2}. \quad (2.24)$$

The equations of narrow-lane combinations for code and phase observations are given by:

$$P_{6,r}^{s,j} = \rho_r^{s,j} + c dt_r^s - c dt_r^{s,j} + T_r^{s,j} + I_6 + b_{P_{6,r}}^s - b_{P_6}^{s,j} + \varepsilon(P_{6,r}^{s,j}) \quad (2.25)$$

$$L_{6,r}^{s,j} = \rho_r^{s,j} + c dt_r^s - c dt_r^{s,j} + T_r^{s,j} - I_6 + \lambda_6^s N_6^{s,j} + b_{L_{6,r}}^s - b_{L_6}^{s,j} + \varepsilon(L_{6,r}^{s,j}) \quad (2.26)$$

where subscript 6 indicates the narrow-lane combination, $\varepsilon(P_{6,r}^{s,j})$ and $\varepsilon(L_{6,r}^{s,j})$ denotes the narrow-lane code noise and phase noise, respectively. Other terms are given below.

$$b_{P_{6,r}}^s = \alpha_{WL} b_{P_{1,r}}^s + \beta_{WL} b_{P_{2,r}}^s \quad b_{P_6}^{s,j} = \alpha_{WL} b_{P_1}^{s,j} + \beta_{WL} b_{P_2}^{s,j} \quad (2.27)$$

$$b_{L_{6,r}}^s = \alpha_{WL} b_{L_{1,r}}^s + \beta_{WL} b_{L_{2,r}}^s \quad b_{L_6}^{s,j} = \alpha_{WL} b_{L_1}^{s,j} + \beta_{WL} b_{L_2}^{s,j} \quad (2.28)$$

$$I_6 = \frac{I}{f_1 \cdot f_2} \quad \lambda_6^s N_6^{s,j} = \alpha_{NL} \lambda_1^s N_1^{s,j} + \beta_{NL} \lambda_2^s N_2^{s,j} \quad (2.29)$$

2.3.5. Melbourne-Wübbena Combination

This combination was first proposed by Hatch [32], then it was additionally stated by Melbourne [33] and Wübbena [34]. In Equation (2.20) and Equation (2.25), it can be seen that the wide-lane combination of the carrier phases and the narrow-lane combination of the code pseudoranges have the same ionospheric effects. Using these combinations, an additional ionospheric-free, i.e. Melbourne-Wübbena combination, can be formed as:

$$MW = L_{5,r}^{s,j} - P_{6,r}^{s,j} = \lambda_5^s N_5^{s,j} + (b_{L_{5,r}}^s - b_{P_{6,r}}^s) - (b_{L_5}^{s,j} - b_{P_6}^{s,j}) + \varepsilon(MW) \quad (2.30)$$

2.4. GNSS Positioning with Single Receiver

Point positioning is the way to determine the receiver position using the navigation satellite signals. High precision GNSS positioning techniques usually require two or more receivers. However, the single receiver positioning techniques have attracted attention among the GNSS community since GPS was started to be used. There are two typical approaches for positioning with single receiver, which are named the Single (Absolute) Point Positioning and Precise Point Positioning.

2.4.1. Absolute Point Positioning

Absolute or Single Point Positioning (APP or SPP) is the simplest GNSS positioning technique, which relies on code pseudorange observations in addition to broadcast ephemeris for calculating receiver coordinates. The broadcast ephemeris is transmitted together with the satellite signals in real time and the orbit and clock corrections obtained from the broadcast ephemeris are not accurate enough for precise positioning, typically at metre level. Therefore, main limitation of SPP is low quality of orbits and clocks obtained from the navigation message.

The most of the error sources on the GNSS signals are not completely mitigated or corrected in SPP. For example, nearly one-half of ionospheric effect can be eliminated using the ionosphere model transmitted in the broadcast ephemeris only. The receiver clock offset is the only parameter to be estimated together with 3D coordinates of the receiver. Therefore, four visible satellites are sufficient to solve navigation problem in SPP. SPP is usually employed in applications which don't require high position accuracies, such as the car navigation and smart phones.

2.4.2. Precise Point Positioning

Precise Point Positioning (PPP) is the positioning technique which employs the dual-frequency ionosphere-free combinations of code and phase observations given in Equation (2.7) and Equation (2.8). Because PPP doesn't utilize any differences between satellites or receivers, the only single receiver is enough to achieve highly precise positioning solution in PPP. This technique was first put forward by Zumberge et al. [1] and then developed by Kouba and Heroux [2]. Nowadays, PPP has been widely employed in a range of applications like precise surveying, atmospheric monitoring and modelling, aerial triangulation, geohazard monitoring, kinematic positioning, etc.

[3, 4, 5, 6, 7, 8, 9].

PPP mainly relies on the usage of highly accurate satellite and clock products, which can only be obtained from a global network. International GNSS Service (IGS) continuously provides the required satellite orbit and clock products to GNSS users via the internet. The usage and specifications of IGS products, such as the accuracy, latency and sample interval, will be discussed in Section 3.1.

The first order ionosphere effects on GNSS observations, which forms nearly 99 percent of the total effect, can be eliminated using ionospheric-free combinations. However, it is required to mitigate the effect of other error sources. The dry part of troposphere effect can be corrected using one of the existing troposphere models, but the wet part is typically estimated together with receiver coordinates and clock offset. Additionally, the advanced error mitigation techniques must be applied to eliminate all error sources in PPP. This techniques will be comprehensively explained in the next chapter.

PPP utilizes carrier phase measurements which include the ambiguity term. The carrier phase ambiguity is estimated as a floating number in traditional PPP approach due to unmodeled hardware bias and the usage of ionosphere-free observations. The position accuracy depends on the code pseudorange observations until the ambiguities sufficiently converge to their final values. The time elapsed to achieve the desired accuracy level is typically named convergence time. The main limitation of PPP is the convergence time, which usually takes 1 hour to reach 5 centimetres or better horizontal accuracy [35].

PPP is one of the frequently used techniques among the GNSS community as mentioned above. Although it has a lot of advantages, the convergence time is still the primary restriction of PPP. In recent years, the ambiguity resolution methods have been developed to accelerate the convergence time in PPP process [10, 11, 12, 13, 14, 15]. Also, the combined multi-GNSS solution can be used to lessen the convergence time of PPP with the additional satellite resources [16, 19].

3. PPP ERROR SOURCES AND THEIR MITIGATION STRATEGIES

GNSS signals are influenced by a range of error sources and it is very crucial to deal with these errors properly to achieve high precision positioning. PPP error sources and mitigation strategies are given in this chapter.

3.1. Satellite Orbit and Clock

All GNSS satellites transmit the broadcast ephemeris together with their ranging signals in real-time. The broadcast ephemeris (so-called predicted ephemeris) includes the satellite orbit and clock information. However, the accuracy of broadcast ephemeris doesn't satisfy the requirement of PPP.

IGS is a civilian GNSS organization which presents observation data sets and precise orbit and clock products to GNSS users. IGS generates precise clock and orbit products using a global network which includes more than 400 reference stations. Additionally, IGS archives and distributes the GNSS data acquired from its network for scientific and engineering applications. Table 3.1 summarizes standard IGS products in different latencies and accuracies [36].

As it can be seen in Table 3.1, IGS products include combined GLONASS orbits, but combined GLONASS clocks are not among the IGS products. Furthermore, IGS does not produce any orbit and clock products for Galileo and BDS. Considering the build-up of new constellations and the modernization of existing systems, the interoperability of navigation systems has become an important matter for GNSS applications.

Multi-GNSS Experiment (MGEX) was started by IGS to monitor, collate and evaluate the whole existing navigation signals in 2011. Firstly, a small network, nearly 40 stations, was equipped with multi-GNSS receivers and MGEX orbit and clock products produced with these observations were started to be used widely in a short time. Then, IGS decided to change the status of MGEX as IGS Multi-GNSS Pilot Project in 2016, however, MGEX has continued to stay in use. As of October 2016, approximately one of third of all IGS stations was consisted of IGS multi-GNSS tracking (Figure 3.1) [29].

It was previously mentioned that the combined satellite ephemeris and clock products

Table 3.1: Standard IGS satellite orbit and clock products [36].

System	Type		Accuracy (RMS)	Latency	Sample Interval
GPS	Broadcast	Orbit	100 cm	Real time	Daily
		Clock	5 ns		
	Ultra-Rapid (predicted)	Orbit	5 cm	Real time	15 min
		Clock	3 ns		
	Ultra-Rapid (observed)	Orbit	3 cm	3-9 hours	15 min
		Clock	150 ps		
	Rapid	Orbit	2.5 cm	17-41 hours	15 min
		Clock	75 ps		5 min
	Final	Orbit	2.5 cm	12-18 days	15 min
		Clock	75 ps		30 sec
GLONASS	Final	Orbit	3 cm	12-18 days	15 min

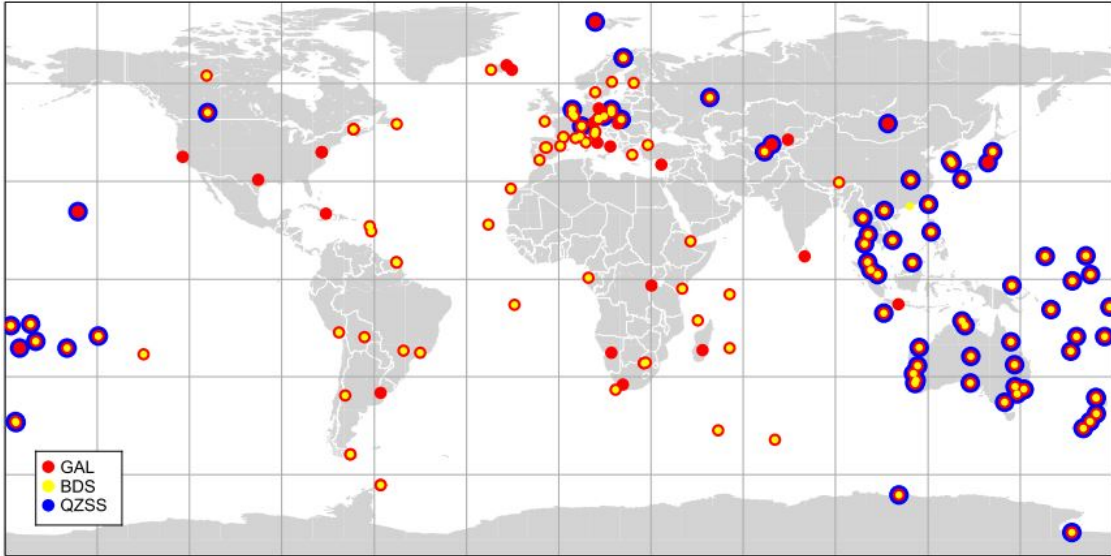


Figure 3.1: IGS multi-GNSS stations [29].

estimated in the same reference frame can be used for multi-GNSS processing. Multi-GNSS satellite ephemeris and clock offsets are estimated and broadcast to users in the same reference frame as a part of the MGEX project. Currently, five institutions generate and distribute multi-GNSS products, which are indicated in Table 3.2.

Satellite positions acquired from IGS or MGEX products have data intervals ranging between 5 and 15 minutes. However, GNSS observations typically are collected with

Table 3.2: A list of MGEX products.

Institution	Abbreviation	Constellation	Orbit Int. (min)	Clock Int. (sec)
CNES/CLS	GRM	GPS+GLO+GAL	15	30
CODE	COM	GPS+GLO+GAL+BDS+QZS	15	300
GFZ	GBM	GPS+GLO+GAL+BDS+QZS	5	30
TUM	TUM	GAL+QZS	5	-
Wuhan Univ.	WUM	GPS+GLO+GAL+BDS+QZS	15	300

higher frequency. Thus, it is necessary to interpolate satellite orbits to compute actual satellite position at signal transmission time. Lagrange interpolation, based on polynomial functions, is widely used for this purpose [31].

There are two different approaches for determining the signal transmission time. The first makes use of the pseudorange observations, while the second is an iterated geometric computation, which does not require any measurement. The first approach has been used in this thesis because it directly provides the signal transmission time ($T(\textit{transmission})$) in the related GNSS time reference as:

$$T(\textit{transmission}) = t_r(\textit{reception}) - P/c - dT \quad (3.1)$$

where $t_r(\textit{reception})$ indicates the signal reception time in the receiver's time scale, P indicates the pseudorange measurement, c is the speed of light in vacuum and dT is the satellite clock offset.

Once the transmission time is determined, satellite positions can be calculated in a given coordinate system. As previously mentioned, the precise ephemeris is based on a Earth-Centered and Earth-Fixed (ECEF) system as reference frame. It means that the reference frame rotates with the Earth. Therefore, the rotation of the frame during the transit time must be considered. Signal reception time is the common time reference for all measurements, so the reference frame must be set for the reception time. The transformation between the satellite position at transmission time and the satellite position at the reception time is given by

$$\mathbf{r}_{\textit{reception}}^{\textit{sat}} = \mathbf{R}_3(\omega_E * \Delta t) * \mathbf{r}_{\textit{transmission}}^{\textit{sat}} \quad (3.2)$$

and

$$\Delta t = \frac{\|\mathbf{r}_{transmission}^{sat} - \mathbf{r}_0^{rcv}\|}{c} \quad (3.3)$$

where ω_E indicates the Earth's rotation rate, $\mathbf{r}_{reception}^{sat}$, $\mathbf{r}_{transmission}^{sat}$ are satellite position at reception and at transmission time respectively, \mathbf{R}_3 is rotation matrix along the Z-axis and \mathbf{r}_0^{rcv} is approximate position of the receiver. Although the pseudorange observation establishes a direct link between the transmission and reception times, it should not be used in the transformation because it includes other delays apart from the geometric distance [30].

3.2. Receiver Clock

The receiver clock bias influences all received signals equally. Most of the GNSS receivers use quartz crystal oscillators. They are not as stable as the atomic clocks used in GNSS satellites. Some receivers try to synchronize its internal clocks with reference time scale to avoid the quite large clock error. This type of receivers inserts discrete clock jumps periodically to keep the receiver clock under a threshold value. The clock jumps typically occur as an integer number of milliseconds.

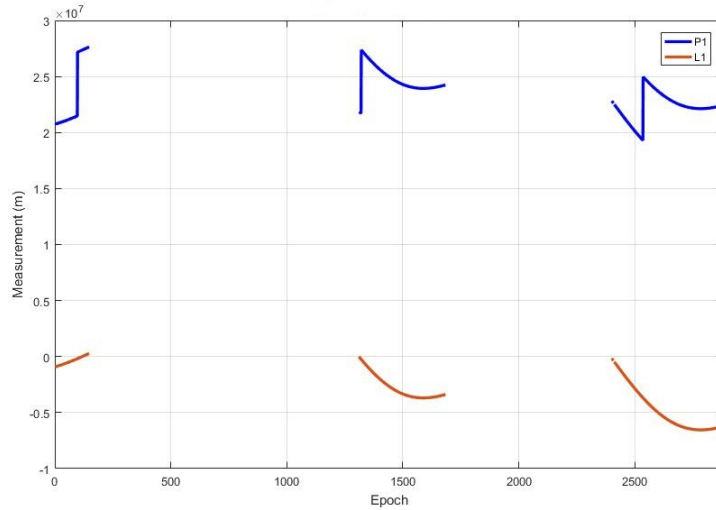


Figure 3.2: The code pseudorange and carrier phase observations obtained from PRN02 satellite on L1 signal during the first day of 2017 at ZWE2 station (Horizontal axis indicates epoch number for 30 seconds observation data).

Figure 3.2 shows the code pseudorange and carrier phase observations obtained from PRN02 satellite on L1 signal during the first day of 2017 at ZWE2 station. As it can be seen in the figure, clock jumps are observed only on code pseudoranges, which causes an inconsistency between code and phase measurements. The clock jumps are categorized into four groups as indicated in Table 3.3 considering their influences on

GNSS observables [37].

Table 3.3: Types of clock jumps [37].

Type	Time tag	Pseudorange	Carrier phase
1	Jumpy	Smooth	Smooth
2	Jumpy	Jumpy	Smooth
3	Smooth	Jumpy	Smooth
4	Smooth	Jumpy	Jumpy

It is not necessary to detect and correct all types of clock jumps. Only type 2 and 3 jumps require for correction due to inconsistency between the pseudorange and phase observations. For this purpose, a new ionosphere-free observable can be formed as:

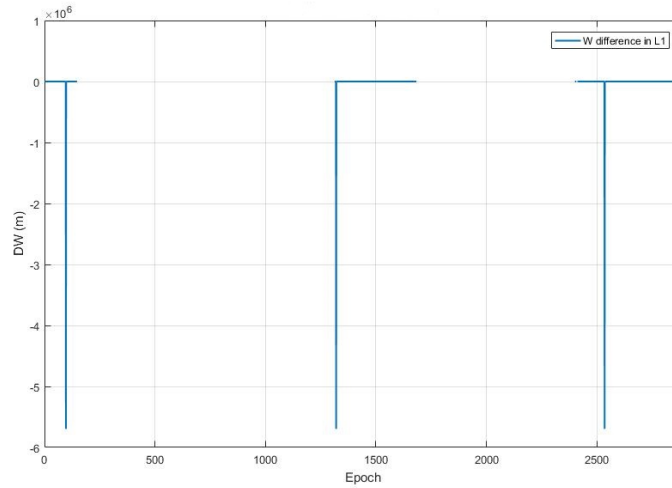
$$W = L_{3,r}^{s,j} - P_{3,r}^{s,j} = \lambda_3^s N_3^{s,j} + (b_{L_{3,r}}^s - b_{P_{3,r}}^s) - (b_{L_3}^{s,j} - b_{P_3}^{s,j}) + \epsilon(W) \quad (3.4)$$

where $L_{3,r}^{s,j}$ and $P_{3,r}^{s,j}$ indicate the ionosphere-free pseudorange and carrier phase observations, respectively. This observable removes the geometric part and atmospheric effects, whereas it still includes ionosphere-free ambiguity and hardware biases. If cycle slips are ignored or repaired, the remaining part doesn't change rapidly, i.e. it has long-term stability. So, the clock jump detection observable is formed as follows:

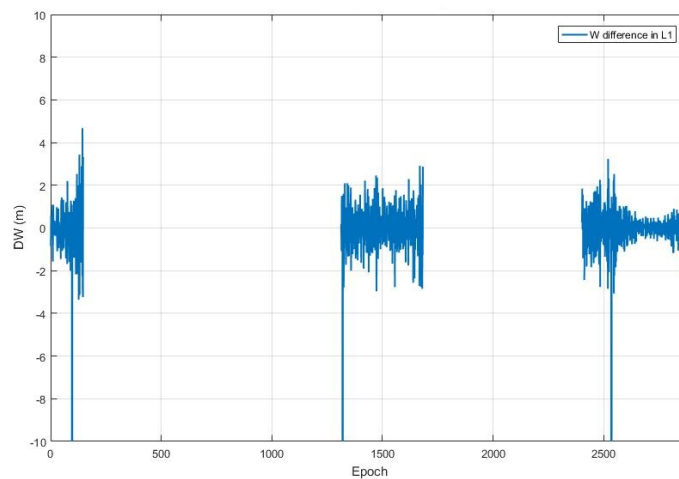
$$\Delta W = W(i) - W(i - 1) \quad (3.5)$$

where i represents a specific epoch and Δ is the epoch difference operator. Once a clock jump occurs, ΔW changes drastically, which simplifies the clock jump detection. A sample sketch of ΔW for the observations obtained from the PRN2 satellite on the L1 signal during the first day of 2017 at ZWE2 station is given in Figure 3.3a. The figure is also scaled to show the time series of ΔW in more details (see Figure 3.3b). If ΔW is an integer number of milliseconds within a certain range of accuracy (typically 50 ns), a clock jump is detected in the related epoch. The clock jump characteristically influences on all the measurements obtained from visible satellites in equal amount, so the another check, which detects whether or not the clock jump affects the whole measurements in the equal amount, is required for the validation [37].

The receiver clock error can be removed using differential positioning techniques. However, it is suggested to estimate the receiver clock as an unknown parameter in the traditional approach of PPP [37]. In this case, particularly for the Kalman filtering, it is important to determine the behaviour of the receiver clock precisely.



(a) 1000 kilometres vertical grid interval.



(b) 2 metres vertical grid interval (scaled).

Figure 3.3: W differences for the observations obtained from the PRN2 satellite on the L1 signal during the first day of 2017 at ZWE2 station (Horizontal axis indicates epoch number for 30 seconds observation data).

3.3. Troposphere

The neutral part of the atmosphere influences the GNSS signal propagation. Although the neutral part involves both the stratosphere and troposphere, the effect is frequently called tropospheric refraction or tropospheric delay. The tropospheric delay on GNSS signals is not dependent on the system frequency due to its non-dispersive nature. That is why the tropospheric effect, in contrast to the ionosphere, cannot be removed using dual-frequency combinations.

The tropospheric delay along the signal path is approximated as follows:

$$T = \int (n - 1) ds = 10^{-6} \int N^{trop} ds \quad (3.6)$$

where n indicates the refractive index of troposphere layer and N^{trop} is so-called its refractivity. The computation of tropospheric path delay is based on an approximation performing the integration along the geometric range. Typically, tropospheric delay is separated into two parts. The first is known as the hydrostatic or dry part, and it is related to the higher parts of the troposphere. The dry part constitutes approximately 90% of total tropospheric delay. The second is known as the non-hydrostatic or wet part, which is mostly due to the lower portions of the troposphere and contains most of the water vapour. The dry component of the tropospheric delay can be easily modelled, but it is difficult to model the wet component due to the irregularities in water vapour variation [38].

$$T = T_{dry} + T_{wet} = 10^{-6} \int N_{dry}^{trop} ds + 10^{-6} \int N_{wet}^{trop} ds \quad (3.7)$$

The tropospheric delay is typically dependent on the signal path, and so it is usually formulated as a function of the zenith distance. Consequently, the tropospheric delay are modelled at zenith direction and projected to the satellite elevation angle using a mapping function [31]:

$$T = Z_{dry} M_{dry}(E) + Z_{wet} M_{wet}(E)$$

where E is the satellite elevation angle, Z_{dry} is the zenith delay due to dry component, Z_{wet} is the zenith delay due to wet component, M_{dry} indicates the dry mapping function and M_{wet} indicates the wet mapping function.

In this study, the zenith delay of the hydrostatic part is approximated using the Saastamoinen model [39] which is one of the most popular dry zenith delay functions and is given by following equation:

$$Z_{dry} = \frac{0.0022768 p}{1 - 0.00266 \cos(2\varphi) - 0.28 \cdot 10^{-6} h} \quad (3.8)$$

where p indicates pressure in millibar, φ is latitude and h is the height in kilometre. The meteorological data can be acquired from either local measurements or a global seasonal temperature and pressure model, e.g. GPT (Global Pressure and Temperature) [40] or its new version GPT2 [41], which is the model preferred in this study. The delay of wet tropospheric part is estimated among the other unknowns in this study, because

of the difficulties to model this component accurately as it is highly variable.

Several mapping functions are available to scale the zenith delay to the satellite elevation angle. The Neill Mapping Function (NMF) [42], the Vienna Mapping Function (VMF) [43] and the Global Mapping Function (GMF) [44] are mostly used functions for this purpose. GMF, which is the mapping function used in this study, utilizes a spherical harmonics expansion of seasonal average VMF parameters to form its coefficients. Also, It only requires day of the year (DOY) as well as station coordinates. The mapping function used for both wet and dry components are expressed as:

$$m(E) = \frac{1 + \frac{a}{1 + \frac{b}{1 + c}}}{\sin E + \frac{b}{\sin E + c}} \quad (3.9)$$

where E is the elevation angle. The dry and wet mapping functions are obtained from different a , b and c parameter sets for the dry and wet components. The subscript d indicates the dry indices. The coefficients a_d is calculated as:

$$a = a_0 + A \cos\left(2\pi \frac{\text{DOY} - 28}{365}\right) \quad (3.10)$$

where a_0 and A are the mean and seasonal values, respectively, which are determined from the spatial spherical harmonics coefficients (A_{nm} and B_{nm}) up to degree and order 9 as follows:

$$\sum_{n=0}^9 \sum_{m=0}^n P_{nm}(\sin(\varphi)) [A_{nm} \cos(m\lambda) + B_{nm} \sin(m\lambda)] \quad (3.11)$$

where P_{nm} are the Legendre polynomials, φ and λ are the site latitude and longitude. According to Boehm et al. [45], the coefficients b and c is used for the hydrostatic component as follows:

$$b_d = 0.0029 \quad (3.12)$$

$$c_d = c_0 + \left[\left(\cos\left(2\pi \frac{\text{DOY} - 28}{365}\right) + \Psi\right) + 1\right] \frac{c_{11}}{2} + c_{10} (1 - \cos \varphi) \quad (3.13)$$

where c_0 , c_{10} and c_{11} values are given in Table 3.4 depending on the hemisphere of the related observation point.

In conclusion, the delay of dry tropospheric part is corrected using the Saastamoinen model with input meteorological data produced by the GPT2 model in this study. However, the delay caused by the wet component of the troposphere is estimated because of the difficulties in its modelling.

Table 3.4: The parameters required for computing coefficient c of the GMF dry mapping function

Hemisphere	c_0	c_{10}	c_{11}	Ψ
Northern	0.062	0.000	0.006	0
Southern	0.062	0.001	0.006	π

3.4. Ionosphere

The ionosphere, which extends from about 50 to 1000 kilometres above the earth surface, constitutes the upper part of the atmosphere. The free electrons in the ionosphere influence the propagation of GNSS signals where ionospheric effect typically depends on the electron density along the signal path. The solar and geomagnetic activities play important roles on the electron formation and its distribution. It is generally difficult to model the ionospheric effect on GNSS signals due to the irregularities of electron density [46].

The first-order refractive index of the ionosphere layer on carrier phase measurements can be approximated to an accuracy better than 99.9% as:

$$n_L = 1 - \frac{40.3 \cdot N_e}{f^2} \quad (3.14)$$

where N_e indicates the total electron density (el/m³) and f indicates signal frequency (Hz). Likewise, the first-order refraction index of the ionosphere for code measurements can be expressed as [46]:

$$n_P = 1 + \frac{40.3 N_e}{f^2}. \quad (3.15)$$

The ionospheric delays on phase and code observations can be obtained by integrating refraction indices along the entire propagation path:

$$\Delta_L^{ion} = \int (n_L - 1) dl = -\frac{40.3}{f^2} \int N_e dl \quad (3.16)$$

$$\Delta_P^{ion} = \int (n_P - 1) dl = \frac{40.3}{f^2} \int N_e dl \quad (3.17)$$

Considering that the Total Electron Content (TEC) is the total number of electrons along the signal path, Equation (3.16) and Equation (3.17) take the following form:

$$\Delta_L^{ion} = -\frac{40.3}{f^2} TEC \quad \Delta_P^{ion} = \frac{40.3}{f^2} TEC \quad (3.18)$$

which designates that the effects of the ionospheric refraction on phase and code measurements are in the same magnitude but have opposite signs. It means that the ionosphere advances the phase measurements but delays the code measurements. Moreover, the ionospheric effect depends on the system frequency because it is a dispersive medium. Therefore, the first-order ionospheric effect can be removed by combining GNSS observations (see Subsection 2.3.1). Traditional PPP approach employs the ionosphere-free combination to remove the first order ionospheric influence, which equals up to 99% of the total ionospheric delay. [47].

3.5. Relativistic Effects

Typically, satellite-based positioning techniques are based on the principle of measuring the time difference between receiver and satellite clocks. Therefore, the measurements based on time differences are subject to the relativistic effects. The relativistic correction which is due to the eccentricity of the satellite orbits is given by:

$$\Delta t_r = -2 \frac{\mathbf{r}^{sat} \cdot \mathbf{v}^{sat}}{c^2} \quad (3.19)$$

where \mathbf{r}^{sat} and \mathbf{v}^{sat} are the satellite position and velocity in an inertial system and c is the speed of light. The related IGS products does not include this correction, it is required to be considered during PPP processing [48].

The secondary relativistic effect which is due to the space-time curvature caused by the gravitational field also brings a delay on GNSS signals. This effect, i.e. the Shapiro signal propagation delay, must be taken into consideration only for high-accuracy positioning because of the effect is less than 2 cm. It is required to correct the Euclidean range between the satellite and receiver as much an amount given by the following expression [47]:

$$\delta_{rel} = \frac{2 \cdot \mu}{c^2} \ln \frac{\rho^{sat} + \rho^{rec} + \rho_{rec}^{sat}}{\rho^{sat} + \rho^{rec} - \rho_{rec}^{sat}} \quad (3.20)$$

where μ is the Earth's gravitational constant, ρ_{sat} indicates the geocentric distance of the satellite, ρ_{rec} indicates the geocentric distance of the receiver and ρ_{rec}^{sat} is the geocentric distance between the satellite and the receiver.

3.6. Antenna Phase Center

It is firstly necessary to describe the satellite orientation by defining a satellite-fixed reference frame before handling antenna phase center (APC). It is essential to understand the behaviour of GNSS satellites for determining its inertial attitude. Typically, the navigation antenna of GNSS satellites are designed to point to the Earth, whereas the solar panels are outlined to keep oriented towards the Sun. Therefore, the satellites attempt to catch the sunlight rotating about the Earth-pointing (*yaw*) axis. The name of this concept is the *yaw-steering* (YS) attitude mode [49].

The origin of the satellite-fixed reference system refers to satellite's center of mass. The system orientation can be defined by three-unit vectors which are given as follows:

$$\hat{\mathbf{e}}_x = \hat{\mathbf{e}}_y \times \hat{\mathbf{e}}_z \quad \hat{\mathbf{e}}_y = \frac{\hat{\mathbf{e}}_{\odot} \times \mathbf{r}}{|\hat{\mathbf{e}}_{\odot} \times \mathbf{r}|}, \quad \hat{\mathbf{e}}_z = -\frac{\mathbf{r}}{|\mathbf{r}|} \quad (3.21)$$

where $\hat{\mathbf{e}}_{\odot}$ is a unit vector pointing from the satellite to the Sun, \mathbf{r} is the satellite position in ECEF. The vector $\hat{\mathbf{e}}_z$ orients towards to the Earth, $\hat{\mathbf{e}}_y$ is the perpendicular to the Sun and nadir direction and $\hat{\mathbf{e}}_z$ completes the right-handed coordinate system (Figure 3.4). IGS has adopted the nominal yaw-steering attitude mode as the reference frame for nearly all GNSS satellites outside eclipse season [49].

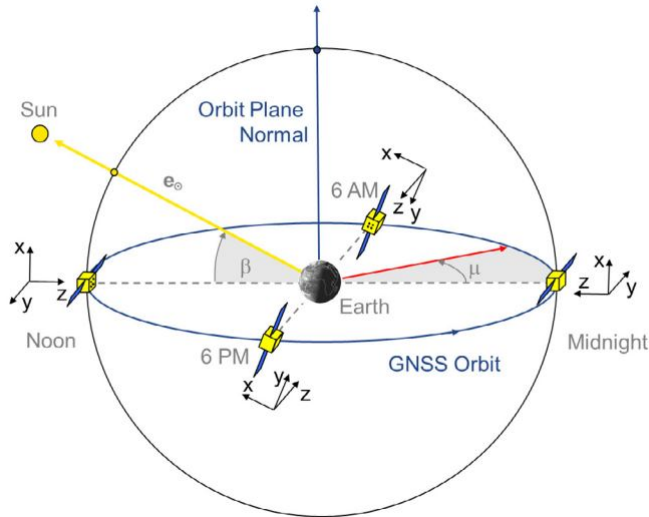


Figure 3.4: GNSS satellite orientation in nominal yaw-steering mode [49].

Unlike the broadcast ephemeris, the precise ephemeris refers to the satellite's center of mass due to employed model in satellite orbit modelling. Nevertheless, GNSS measurements take satellite APC as the reference point. Hence, it is required to consider the antenna phase center offsets (PCO) for precise point positioning which employs

the precise products [47]. The conversion from the satellite's center of mass to APC is performed as follows:

$$\mathbf{X}_{phase} = \mathbf{X}_{mass} + \begin{bmatrix} \hat{\mathbf{e}}_x & \hat{\mathbf{e}}_y & \hat{\mathbf{e}}_z \end{bmatrix}^{-1} \cdot \Delta \mathbf{x}_{offset} \quad (3.22)$$

where $\Delta \mathbf{x}_{offset}$ indicates the PCO in satellite-fixed coordinate system and \mathbf{X}_{phase} , \mathbf{X}_{mass} are the satellite coordinates referring to APC and satellite center of mass, respectively.

In addition, the electrical phase center of the antenna varies depending on the signal frequency and signal direction. In other words, each incoming signal has its own electrical APC [2]. Consequently, it is also required to take the signal dependent antenna phase center variations (PCV) into consideration within precise point positioning concept.

The correction of PCV is added to geometric range as:

$$\rho_{obs} = \rho_{geo} + PCV(elevation, azimuth) \quad (3.23)$$

where ρ_{obs} , ρ_{geo} are the observed and geometric ranges, respectively.

When it comes to receiver antennas, a geometrical point called antenna reference point (ARP) is introduced due to the variation of APC depending on the incoming signal direction. So, PCOs are typically defined as the three-dimensional coordinate correction with respect to the reference point. PCVs are also applied as a correction to the geometric range. Similar to the satellite antenna, the receiver antenna correction can be expressed as:

$$\begin{aligned} \mathbf{X}_{phase} &= \mathbf{X}_{ARP} + \Delta \mathbf{x}_{pco} \\ \rho_{obs} &= \rho_{geo} + PCV(elevation, azimuth) \end{aligned}$$

where \mathbf{X}_{phase} indicates the mean electrical APC position, \mathbf{X}_{ARP} is the ARP position, $\Delta \mathbf{x}_{pco}$ is PCO given usually in a receiver-based local system, ρ_{obs} and ρ_{geo} are the observed and geometric ranges, respectively.

IGS, using an absolute antenna model, produces and broadcasts the antenna PCOs and PCVs for the receiver and satellites [50]. In the first stage, the product included only GPS and GLONASS frequencies. Fortunately, the satellite antenna PCOs for GALILEO and BeiDou were added in 2015 [29]. The IGS antenna model and corrections (igs08.atx) should be utilized during the process of precise point positioning.

3.7. Phase Wind-up

As previously stated, GNSS utilizes right-handed circularly polarized signals for navigation purposes. Hence, carrier phase observation obtained from the phase difference between satellite and receiver signal is dependent on the relative position of receiver and satellite antennas. Mutual orientation of the antennas brings about a change, named *Phase Wind-up*, in the measured carrier phases, which can reach at most one cycle [51]. Phase Wind-up effect is typically ignored in differential positioning. However, it is essential to apply Wind-up effect as a correction in un-differenced positioning, such as precise point positioning.

Considering that antenna orientation of stationary receiver does not frequently alter, the main reason of phase wind-up effect is the satellite orbital motion. Typically, GNSS satellites perform a rotation around their z-axis because they attempt to keep their solar panels oriented towards the Sun. Thus, the relative orientation of the receiver and satellite antennas often change, which influences carrier phase measurement.

Wind-up effect on carrier phase measurements is modeled and corrected by the following equation [51]:

$$\Delta\phi = \text{sign}(\hat{\mathbf{p}} \cdot (\vec{\mathbf{d}}' \times \vec{\mathbf{d}})) \cos^{-1} \left(\frac{\vec{\mathbf{d}}' \cdot \vec{\mathbf{d}}}{|\vec{\mathbf{d}}'| \cdot |\vec{\mathbf{d}}|} \right) \quad (3.24)$$

where $\hat{\mathbf{p}}$ indicates the unit vector between satellite and receiver, $\vec{\mathbf{d}}'$ and $\vec{\mathbf{d}}$ are the effective dipole vectors of the receiver and satellite antennas determined by the related satellite body coordinate unit vectors ($\hat{\mathbf{e}}_x, \hat{\mathbf{e}}_y, \hat{\mathbf{e}}_z$) and the local receiver unit vectors ($\hat{\mathbf{n}}, \hat{\mathbf{e}}, \hat{\mathbf{u}}$), respectively. Effective dipole vectors are given by

$$\vec{\mathbf{d}}' = \hat{\mathbf{e}}_x - \hat{\mathbf{p}} (\hat{\mathbf{p}} \cdot \hat{\mathbf{e}}_x) - \hat{\mathbf{p}} \times \hat{\mathbf{e}}_y \quad (3.25)$$

$$\vec{\mathbf{d}} = \hat{\mathbf{n}} - \hat{\mathbf{p}} (\hat{\mathbf{p}} \cdot \hat{\mathbf{n}}) - \hat{\mathbf{p}} \times \hat{\mathbf{e}}. \quad (3.26)$$

The continuity of phase measurements between consecutive epochs should be guaranteed by appending full cycles to the Phase Wind-up correction in Equation (3.24) [47].

3.8. Solid Earth Tide

The variations in the gravitational forces imposed by the Sun, Moon and other planets give rise to deformations on the solid Earth. As a consequence, the ground stations

undergoes periodic movements, which is named the solid Earth tide. This displacement may arrive up to 30 centimetres and 5 centimetres in vertical and horizontal, respectively [47].

The site displacement induced by solid Earth tides are usually represented by spherical harmonics. Love and Shida number characterize the degree and order (n, m) of this spherical harmonics. At the same time, values of Love and Shida numbers are defined depending on geographical location of the station and tidal frequency [52]. Typically, the site displacement is split into two parts, which are the permanent and periodic parts. Whereas periodic part can be mainly averaged out in the static positioning of the whole day, the permanent part remains in such a while average position. The effect of the permanent component can arrive up to 12 centimetres near middle latitudes. Both the periodic and permanent tidal distortions must be taken into account completely to be consistent with ITRF system convention [47]. The site displacement vector including the effects of periodic and permanent parts can be computed by the following equation [53]:

$$\Delta \vec{r} = \sum_{j=2}^3 \frac{GM_j R_e^4}{GMR_j^3} \left\{ h_2 \hat{\mathbf{r}} \left(\frac{3(\hat{\mathbf{R}}_j \cdot \hat{\mathbf{r}})^2 - 1}{2} \right) + 3l_2 (\hat{\mathbf{R}}_j \cdot \hat{\mathbf{r}}) \left[\hat{\mathbf{R}}_j - (\hat{\mathbf{R}}_j \cdot \hat{\mathbf{r}}) \hat{\mathbf{r}} \right] \right\} \quad (3.27)$$

$$+ \left[-0.025 m \sin(\varphi) \cos(\varphi) \sin(\Theta_{Gr} + \lambda) \right] \cdot \hat{\mathbf{r}}$$

where,

GM_j gravitational parameter for the Moon ($j=2$) or the Sun ($j=3$),

GM gravitational parameter for the Earth,

$\hat{\mathbf{R}}_j, R_j$ unit vector from the geocenter to Moon ($j=2$) or Sun ($j=3$) and the magnitude of the that vector,

R_e Earth's equatorial radius,

$\hat{\mathbf{r}}, r$ unit vector from the geocenter to the station and the magnitude of the that vector,

h_2 nominal degree 2 Love number,

l_2 nominal degree 2 Shida number,

φ, λ latitude and longitude of the station,

Θ_{Gr} Greenwich Mean Sidereal Time.

Based on the site latitude, h_2 and l_2 can be computed as:

$$h_2 = 0.6078 - 0.0006 [(3 \sin^2(\varphi) - 1)/2]$$

$$l_2 = 0.0847 + 0.0002 [(3 \sin^2(\varphi) - 1)/2].$$

3.9. Ocean Loading

Temporal variations of the ocean mass distribution due to ocean tides produce time-varying deformation on the Earth crust. Additionally, the ocean loading is more localized and cause fewer displacements on the Earth crust in comparison with the solid Earth tides. Ocean loading effect is negligible for static positioning over twenty-four hours period as well as stations which are far from the oceans, whereas it must be taken account in precise kinematic positioning or precise static positioning near coastal regions [47]. The effects of ocean loading can be obtained by:

$$\Delta c = \sum_j f_j A_{cj} \cos(w_j t + \chi_j + u_j - \phi_j) \quad (3.28)$$

where j represents the 11 tidal waves ($M_2, S_2, N_2, K_2, K_1, O_1, P_1, Q_1, M_f, M_m, S_{sa}$), f_j and u_j depend on the longitude of the lunar node, w and χ are the angular velocity and the astronomical arguments for the tidal wave component j at time $t = 0^h$, A_{cj} and ϕ_j are station specific amplitude and phase coefficients for the tidal wave component j [53].

3.10. Polar Tide

The variations of the Earth's instantaneous axis of rotation give rise to periodical deformations on Earth's crust. The polar tide displacements can reach up to 25 mm in vertical and 7 milimetres in horizontal directions. Unfortunately, unlike the solid earth tides and the ocean loading effects, the pole tides do not average out over a 24 hours period. The polar tide correction must be applied when sub-centimetre position precision is required [47]. The corrections to latitude (+north), longitude (+east) and height(+up) in mm can be computed as follows:

$$\begin{aligned} \Delta\varphi &= -9 \cos(2\varphi) [(X_p - \bar{X}_p) \cos \lambda - (Y_p - \bar{Y}_p) \sin \lambda] \\ \Delta\lambda &= 9 \sin \varphi [(X_p - \bar{X}_p) \sin \lambda + (Y_p - \bar{Y}_p) \cos \lambda] \\ \Delta r &= -33 \sin 2\varphi [(X_p - \bar{X}_p) \cos \lambda - (Y_p - \bar{Y}_p) \sin \lambda] \end{aligned} \quad (3.29)$$

where φ and λ are station latitude and longitude, $(X_p - \bar{X}_p)$ and $(Y_p - \bar{Y}_p)$ are the pole coordinate variations from the mean poles (\bar{X}_p, \bar{Y}_p) in seconds of arc [53].

3.11. Differential Code Biases

The difference between signal travel times caused by the hardware group delay differences in satellite and receiver equipment is named Differential Code Biases (DCBs). The single frequency users must take DCBs into consideration in point positioning and timing applications. Also, the dual frequency users require considering the effect of DCBs when the signals employed in an ionosphere-free linear combination differ from the one utilized in the precise products generation [54].

DCBs are typically divided into the satellite-specific and receiver-specific parts. The receiver-specific bias is neglected in most positioning applications because its effect is lumped into the receiver clock error in the estimation process. However, the satellite-specific bias needs still to be corrected.

IGS and MGEX products are typically based on the ionosphere-free combinations composed of particular observations (e.g. $P1$ and $P2$ observations for GPS). As previously mentioned, if the receiver produces a different set of observations, the transformation between corresponding observations must be performed. For example, the receivers recording only $C1$ and $P2$ observations require the generation of $P1$ from $C1$ so that the users using this receiver can make use of the IGS products to constitute $P1$ like observation $P1'$ from $C1$:

$$P1' = C1 + \Delta_{P1-C1} \quad (3.30)$$

where Δ_{P1-C1} is DCB between $P1$ and $C1$ observations.

DCBs are calculated and broadcast to GNSS users by several agencies. CODE generates a averaged set of DCBs for GPS and GLONASS satellites in every month [55]. Also, the multi-GNSS DCB products are provided to users by two agencies (DLR and Chinese Academy of Sciences, CAS) as a part of IGS MGEX project [29].

3.12. Cycle Slips

Highly accurate GNSS positioning can be achieved through the carrier phase observations. Traditional PPP approach makes use of the ionosphere-free combinations of dual frequency code and phase observations [2]. Although carrier phase observations provide

more accurate positioning relatively, they include the integer ambiguity parameter as an unknown (see Equation (2.4)) at the same time. The integer ambiguity parameter must be corrected or estimated to achieve high positioning accuracy in carrier phase observations.

Also, carrier phase observations can be subjected to instantaneous jumps, which are called the cycle slips. Cycle slip is a abrupt jump in the carrier phase observations caused by GNSS receiver failure to signal tracking. A cycle slip typically occurs on measurements of one satellite at a particular epoch. The occurrence of cycle slips gives rise to a discontinuity in the measurements. If the cycle slips remain unrepaired, it can deteriorate the accuracy and convergence time in PPP. Therefore, cycle slips must be detected and repaired correctly in precise positioning applications. A range of methods based on the dual-frequency combinations can be successfully used for the cycle slip detection. Melbourne-Wübbena (MW) combination (see Equation (2.30)), which includes wide-lane ambiguity, is typically used for this purpose due to its low noise level and insensitiveness to ionospheric variations. Wide-lane ambiguity is computed as follows:

$$N_5^{s,j} = \frac{MW}{\lambda_5^s} \quad (3.31)$$

where $\lambda_5^s = c/(f_1 - f_2)$ is the wide-lane wavelength, $N_5^{s,j} = N_1^{s,j} - N_2^{s,j}$ is the wide-lane ambiguity, s and j are the particular system and satellite, respectively. The cycle slip term can be computed by tracking the wide-lane ambiguity:

$$[\Delta N_1^{s,j}(i) - \Delta N_2^{s,j}(i)] = N_5^{s,j}(i - 1) - N_5^{s,j}(i) \quad (3.32)$$

where i indicates the related epoch. If observation arc does not include any cycle slip, the variation of the cycle slip term must be at the noise level of wide-lane ambiguity, which equals to approximately 0.6 cycles. Cycle slip is detected at an epoch if the cycle slip term is greater than a threshold value, e.g. four times of the standard deviation. Otherwise, it is assumed that there is no cycle slip at the epoch [56].

Although the MW combination is quite useful in identifying cycle slips, it has some disadvantages as well. For example, this method cannot detect cycle slips when they have the same size and same sign on both carriers. Moreover, the magnitude of cycle slips on both measurements cannot be distinguished them each other. Because of these reasons, it is necessary to utilize the MW combination in conjunction with another method. The geometry-free (GF) combination of carrier phase measurements (Equation (2.14)) can be employed together with the MW combination for this purpose.

Geometry-free (GF) combination eliminates all geometry-dependent terms, but it still

includes ionospheric errors and phase ambiguities as well as inter-frequency hardware biases. Large ionospheric activity or long observation intervals give rise to significant variations on GF combination. Furthermore, the ionospheric refraction is mainly dependent on the satellite elevation angle. In order to reflect this relation, a threshold value dependent on the elevation angle should be used for preventing false detection of the cycle slips [57]. Cycle slip term based on GF combination can be formed by:

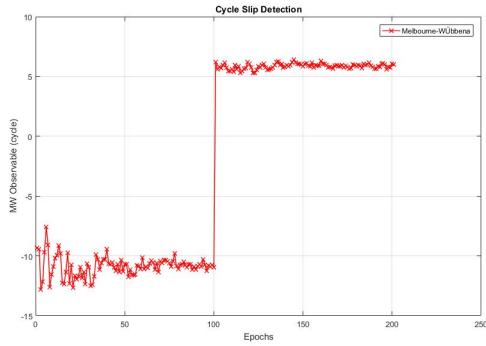
$$abs(L_{4,r}^{s,j}(i) - L_{4,r}^{s,j}(i - 1)) > s\sigma + \Delta l_{max} \quad (3.33)$$

where i indicates the related epoch, s depends on the confidence level (generally $s = 3$ or $s = 4$), σ indicates the standard deviation of GF combination and Δl_{max} is an empirical value used to bound possible ionosphere changes between consecutive epochs where 0.4 m/hr can be used for Δl_{max} [57]. The standard deviation value can be determined based on the satellite elevation angle as:

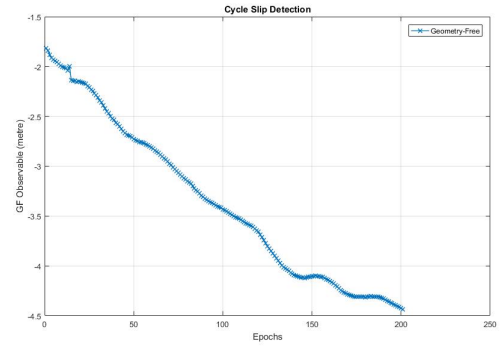
$$\sigma = \sqrt{2(\sigma_{L1}^2 + \sigma_{L2}^2)} \cdot M(E), \quad M(E) = 1 + 10e^{\frac{-E}{10}} \quad (3.34)$$

where σ_{L1}^2 and σ_{L2}^2 are the standard deviations of carrier phase measurements for frequencies 1 and 2, and the elevation angle is indicated by E .

Figure 3.5 and Figure 3.6 show two extraordinary situations in cycle slip detection. These simulations have been formed adding extra cycles to L1 and L2 carrier measurements which are free of cycle slips in the same arc. Figure 3.5 shows that GF combination is insensitive to cycle slips when both carrier phases have the particular cycle slip pairs ($77n_1$ & $60n_2$, $n = \pm 1, 2, 3, \dots$). Similarly, Figure 3.6 indicates that MW combination cannot detect cycle slips when they have the same size and same sign in both carrier phase observations (e.g. $n_1 = n_2 = 10$). Therefore, MW combination has been used together with GF combination to detect cycle slips, determine their size and repair carrier phase measurements in this thesis.

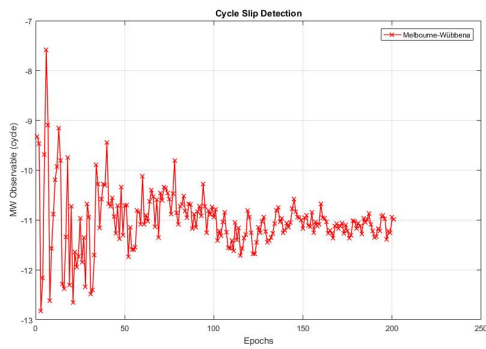


(a) MW combination

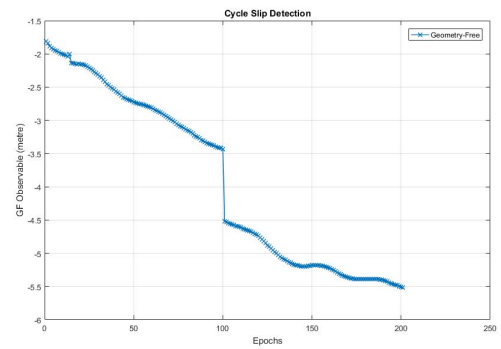


(b) GF combination

Figure 3.5: Simulation of cycle slip based on the values of additional cycles on L1 and L2 frequencies $n_1 = 77$, $n_2 = 60$.



(a) MW combination



(b) GF combination

Figure 3.6: Simulation of cycle slip based on the values of additional cycles on L1 and L2 frequencies $n_1 = 10$, $n_2 = 10$.

3.13. Summary

Finally, PPP error sources and their mitigation strategies are indicated in Table 3.5. In addition, the table shows the possible effect of each error sources on the line of sight (LOS) direction when any correction is not applied.

Table 3.5: PPP error sources, their mitigation strategies and possible effects on line of sight direction.

Error Sources	Effect on LOS di- rection	Mitigation tech- nique
Orbit error after broadcast ephemeris compensation	~ 1 m	Precise orbit
Clock error after broadcast ephemeris compensation	~ 2 ns (0.6) m	Precise clock
Ionosphere (first order)	removed	Ionosphere-free combination
Troposphere	~ 2.3 m	Dry part is corrected by Saastamoinen model, wet part is estimated
Relativistic effect on satellite clock	~ 1 m	Equation (3.19)
Relativistic effect on signal propagation	$\sim 1 - 2$ cm	Equation (3.20)
Satellite antenna PCO	~ 2 m	IGS ANTEX file
Satellite antenna PCV	$\sim 1 - 2$ cm	IGS ANTEX file
Receiver ARP	~ 10 cm	Observation file (RINEX)
Receiver antenna PCV	~ 1 cm	IGS ANTEX file
Phase Wind-up	~ 1 cycle	Equation (3.24)
Solid Earth tide	~ 30 cm	Equation (3.27)
Ocean Loading	~ 5 cm	Equation (3.28)
Polar tide	~ 2.5 cm	Equation (3.29)

*LOS: Line of sight, PCV: Phase center offset, PCO: Phase center variation, ARP: Antenna reference point

4. TRADITIONAL AND MULTI-GNSS PPP APPROACHES

PPP, which can achieve centimetre or decimetre-level positioning accuracy with only one receiver, has been a popular topic among the GNSS community over the past decade. Nevertheless, convergence time is still the main restriction of PPP due to the requirement to estimate float ambiguities with the limited number of visible satellites. As mentioned in Subsection 2.4.2, it can be possible to fix the ambiguity parameters as integer numbers when the ambiguity parameters regain integer nature using the external corrections. These methods are named the ambiguity-fixed solutions due to the recovery of the integer characteristic and can be utilized to shorten the convergence time [10, 12, 11, 13]. The other way to lessen the convergence time is to provide additional satellite resources. The emergence of new satellite-based navigation systems provides an opportunity to enhance the number of visible satellites and to lessen the convergence time consequently [16, 19]. On the other hand, the integration of the new systems entails new approaches on PPP modelling. This chapter focuses on integrating the multi-GNSS to improve the PPP performance and provides information about the traditional and multi-GNSS PPP models.

Regardless of the employed model, estimation of a set of parameters, such as the receiver position and clock offset with an appropriate estimation method (e.g. Kalman filter or least squares adjustment), is essential in PPP. Since Kalman filter provides additional information on how the states change with time, which contributes to more accurate solutions if assumption is correct, and also it makes possible to update the state vector using fewer measurements than the estimated parameters, the Kalman filter is employed as the estimation method in this thesis [58]. In accordance with the common implementation, this chapter includes the mathematical description of Kalman filter, namely Extended Kalman filter, as the first step to PPP modelling since the functional and stochastic components of the model depend on the estimation method widely.

In summary, this chapter includes the mathematical representation of Extended Kalman filter, the description of functional and stochastic models of traditional PPP approach, the presentation of improved multi-GNSS PPP models and the introduction of further improvements.

4.1. Extended Kalman Filter

Kalman filter is an optimal recursive algorithm which employs all available measurements and a priori information about the system and measurements to estimate a set of variables with the statistically minimized error [59, 60]. The Kalman filter carries forward all previous information in the filter instead of saving and reprocessing all previous data, which means that it is recursive. Also, it is optimal because of satisfying the general optimality conditions given as follows:

$$\lim_{n \rightarrow \infty} P(|\hat{x} - x| < \varepsilon) \quad (4.1)$$

$$E(\hat{x}) = x \quad (4.2)$$

$$E\{(\hat{x} - E(\hat{x}))^T(\hat{x} - E(\hat{x}))\} = \min \quad (4.3)$$

where n is the sample size, x is the state vector, \hat{x} is the estimate of the state vector, ε is a very small value, $P()$ is the statistical probability and $E()$ is the statistical expectation [61].

The Kalman filter provides solution to the estimation of the state which is controlled by a linear discrete-time process. If estimation process and/or measurement model is non-linear, Extended Kalman filter (EKF), which extends the scope of Kalman filter to nonlinear optimal filtering problem, is applied [62].

The non-linear dynamic model employed in EKF is expressed by

$$x_k = f(x_{k-1}, w_{k-1}), \quad (4.4)$$

and the non-linear measurement model is given as follows:

$$z_k = h(x_k, v_k) \quad (4.5)$$

where x_k and x_{k-1} are the state vectors at epoch k and $k - 1$ respectively, f is the state transition function describing the dynamic model, z_k is the measurement at epoch k , h is the measurement model relating the state x_k to the measurement z_k , and w_k and v_k are random variables that indicates the zero-mean process and measurement noise, respectively.

The individual values of the noise are actually uncertain at each step, where the state

vector can be approximated as:

$$\tilde{x}_k = f(\hat{x}_{k-1}, 0) \quad (4.6)$$

and the non-linear measurement model can be expressed as:

$$\tilde{z}_k = h(\hat{x}_k, 0) \quad (4.7)$$

where \tilde{x}_k and \tilde{z}_k indicate the approximate state and measurement vectors. It should be noted that the random variables don't follow a normal probability distribution as they undergo the non-linear transformation process [62]. Therefore, the non-linear dynamic and measurement model equations that linearise an estimate about Equation (4.6) and Equation (4.7) are given as follows:

$$x_k \approx \tilde{x}_k + A(x_{k-1} - \hat{x}_{k-1}) + W_{w_{k-1}} \quad (4.8)$$

$$z_k \approx \tilde{z}_k + H(x_k - \hat{x}_k) + V_{v_{k-1}} \quad (4.9)$$

where \hat{x}_k is an *a posteriori* estimate of the state at epoch k and

- A is the Jacobian matrix of partial derivatives of f with respect to x ,

$$A_{[i,j]} = \frac{\partial f_{[i]}}{\partial x_{[j]}}(\hat{x}_{k-1}, 0), \quad (4.10)$$

- W is the Jacobian matrix of partial derivatives of f with respect to w ,

$$W_{[i,j]} = \frac{\partial f_{[i]}}{\partial w_{[j]}}(\hat{x}_{k-1}, 0), \quad (4.11)$$

- H is the Jacobian matrix of partial derivatives of h with respect to x ,

$$H_{[i,j]} = \frac{\partial h_{[i]}}{\partial x_{[j]}}(\tilde{x}_k, 0), \quad (4.12)$$

- V is the Jacobian matrix of partial derivatives of h with respect to v ,

$$V_{[i,j]} = \frac{\partial h_{[i]}}{\partial v_{[j]}}(\tilde{x}_k, 0). \quad (4.13)$$

A , W , H and V are in fact different at each time step [62]. The prediction error \tilde{e}_{x_k} and measurement residual \tilde{e}_{z_k} can be written as:

$$\tilde{e}_{x_k} \approx A(x_{k-1} - \hat{x}_{k-1}) + \epsilon_k \quad (4.14)$$

$$\tilde{e}_{z_k} \approx H\tilde{e}_{x_k} + \eta_k \quad (4.15)$$

where ϵ_k and η_k indicate new independent random variables having zero mean and covariance matrices WQW^T and VRV^T , respectively. It can be noticed that Equation (4.14) and Equation (4.15) are linear, therefore the new random variables approximately follow the normal probability distribution as given in the following equations:

$$P(\tilde{e}_{x_k}) \sim N(0, E[\tilde{e}_{x_k}\tilde{e}_{x_k}^T]) \quad (4.16)$$

$$P(\tilde{\epsilon}_k) \sim N(0, WQ_kW^T) \quad (4.17)$$

$$P(\tilde{\eta}_k) \sim N(0, VR_kV^T). \quad (4.18)$$

The EKF processing includes the prediction and update steps. In the prediction step, the state vector which contains the estimated parameters and its covariance matrix are estimated for the next steps. Then, the predicted state is corrected with respect to the measurements at current step in order to acquire improved estimates of the state vector. The equations in the update step are sometimes called the measurement update equations. The equations for the prediction and update steps of EKF are given as follows:

- EKF time update equations

$$\hat{x}_k^- = f(\hat{x}_{k-1}, 0) \quad (4.19)$$

$$P_k^- = A_k P_{k-1} A_k^T + W_k Q_{k-1} W_k^T \quad (4.20)$$

- EKF measurement update equations

$$K_k = P_k^- H_k^T (H_k P_k^- H_k^T + VR_kV^T)^{-1} \quad (4.21)$$

$$\hat{x}_k = \hat{x}_k^- + K_k(z_k - h(\hat{x}_k^-, 0)) \quad (4.22)$$

$$P_k = (I - K_k H_k) P_k^- \quad (4.23)$$

where \hat{x}_k^- and \hat{x}_k are predicted and updated state vectors, respectively; P_k^- and P_k are predicted and updated state covariance matrices, respectively; and K_k is the Kalman gain matrix [62].

The computers typically use limited precision for floating point computations, which causes numerical round-off errors. Therefore, the updated state covariance matrix might fail to be symmetric and positive definite, which may lead to an ill-conditioned implementation. To overcome this problem, *Joseph form* of P_k (Equation (4.23)),

which ensures that P_k is symmetric positive definite, can be used as given by following equation [63] :

$$P_k = [I - K_k H_k] P_k^- [I - K_k H_k]^T + K_k R_k K_k^T. \quad (4.24)$$

The full operation process of EKF is demonstrated in Figure 4.1.

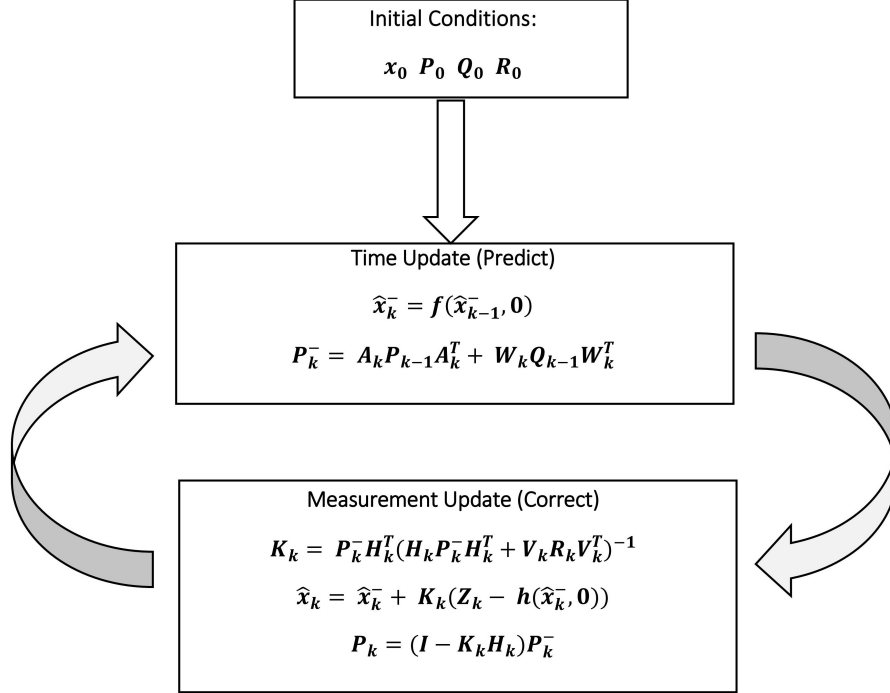


Figure 4.1: The complete EKF process steps.

4.2. Traditional PPP Approach

PPP is originally designed to obtain receiver position with the dual-frequency ionospheric-free combinations of GPS measurements only. This approach, which was put forward by Zumberge et al. [1] and developed by Kouba and Heroux [2]. The functional and stochastic models used in the traditional PPP approach are described below.

4.2.1. Functional Model

The functional model, which is also called observation model, defines the mathematical relationship between the measurements and unknown parameters. The traditional PPP approach employs the ionosphere-free combination, which is a very popular way for removing the first order ionospheric effect on the measurements (see Subsection 2.3.1).

The equations of the ionosphere-free combinations for GPS can be reorganized as:

$$P_{3,r}^{G,j} = \rho_r^{G,j} + c \tilde{dt}_r^G - c \tilde{dt}^{G,j} + T_r^{G,j} + \varepsilon(P_{3,r}) \quad (4.25)$$

$$L_{3,r}^{G,j} = \rho_r^{G,j} + c \hat{dt}_r^G - c \hat{dt}^{G,j} + T_r^{G,j} + \lambda_3^G N_3^{G,j} + \varepsilon(L_{3,r}) \quad (4.26)$$

where

$$c \tilde{dt}_r^G = c(dt_r^G + b_{P_{3,r}}^G) \quad (4.27)$$

$$c \tilde{dt}^{G,j} = c(dt^{G,j} + b_{P_3}^{G,j}) \quad (4.28)$$

$$c \hat{dt}_r^G = c(dt_r^G + b_{L_{3,r}}^G) \quad (4.29)$$

$$c \hat{dt}^{G,j} = c(dt^{G,j} + b_{L_3}^{G,j}) \quad (4.30)$$

and other terms are the same as given in previous chapters. The following terminology is found in the literature: $c \tilde{dt}_r^G$ is the receiver code clock error, $c \tilde{dt}^{G,j}$ is the satellite code clock error, $c \hat{dt}_r^G$ is the receiver phase clock error and $c \hat{dt}^{G,j}$ is the satellite phase clock error [15].

The main strength of PPP is to employ the precise products to eliminate satellite-related clock and orbit errors. Typically, IGS final products are utilized to minimize the effect of satellite code clock error in the ionosphere-free code observation, whereas the receiver code clock error is estimated as well as the receiver position. At the same time, satellite code clock correction obtained from IGS products is also applied to the ionosphere-free phase observations in the traditional PPP model because IGS doesn't provide any phase clock correction. Taking all these into consideration, Equation (4.25) and Equation (4.26) can be rewritten as follows:

$$P_{3,r}^{G,j} = \rho_r^{G,j} + c \tilde{dt}_r^G - c \tilde{dt}^{G,j} + T_r^{G,j} + \varepsilon(P_{3,r}) \quad (4.31)$$

$$L_{3,r}^{G,j} = \rho_r^{G,j} + c \tilde{dt}_r^G - c \tilde{dt}^{G,j} + T_r^{G,j} + \lambda_3^G B_3^{G,j} + \varepsilon(L_{3,r}) \quad (4.32)$$

$$\lambda_3^G B_3^{G,j} = \lambda_3^G N_3^{G,j} + (b_{L_{3,r}}^G - b_{P_{3,r}}^G) - (b_{L_3}^{G,j} - b_{P_3}^{G,j}) \quad (4.33)$$

where the estimated ambiguity parameter ($\lambda_3^G N_3^{G,j}$) is actually a linear function of the integer ambiguity and hardware biases of receiver and satellite. Thus, the estimated ambiguity parameter is no longer an integer number and named the floating ambiguity.

The precise products are applied to ionosphere-free combinations, which removes the first order of ionospheric effect, to mitigate the satellite orbit and clock errors. Additionally, the error handling strategies described in the previous chapter are used to model the rest of error sources. After correcting the whole error sources, the observa-

tion model is given by the following simplified equations:

$$P_{3,r}^{G,j} = \rho_r^{G,j} + c \tilde{dt}_r^G + Z_{wet} M_{wet}(E) + \varepsilon (P_{3,r}) \quad (4.34)$$

$$L_{3,r}^{G,j} = \rho_r^{G,j} + c \tilde{dt}_r^G + Z_{wet} M_{wet}(E) + \lambda_3^G B_3^{G,j} + \varepsilon (L_{3,r}) \quad (4.35)$$

$$\rho_r^{G,j} = \sqrt{(x^s - x^r)^2 + (y^s - y^r)^2 + (z^s - z^r)^2} \quad (4.36)$$

where x^s, y^s, z^s indicates the satellite position and x^r, y^r, z^r indicates the receiver position.

Apart from the direct interests, some unmodeled parameters remain as unknowns in Equation (4.34) and Equation (4.35). The unknown parameters consist of three coordinate components, one receiver clock offset, one zenith wet tropospheric delay component and the floating ambiguity parameters associated with each observed satellite. Therefore, the state vector which includes the unknown parameters is given by:

$$x = [x^r, y^r, z^r, c \tilde{dt}_r^G, Z_{wet}, \lambda_3^G B_3^{G,1}, \lambda_3^G B_3^{G,2}, \dots] \quad (4.37)$$

From the observation model, it can be seen that the measurement equations are non-linear. Therefore, the design matrix consists of the Jacobians of the estimated parameters, that is the elements of the state vector, in the observation model. The Jacobians of the observation model are expressed as follows:

$$\begin{aligned} \frac{\partial P_{3,r}^{G,j}}{\partial x^r} &= \frac{\partial L_{3,r}^{G,j}}{\partial x^r} = -\frac{x^s - x^r}{\rho}, \\ \frac{\partial P_{3,r}^{G,j}}{\partial y^r} &= \frac{\partial L_{3,r}^{G,j}}{\partial y^r} = -\frac{y^s - y^r}{\rho}, \\ \frac{\partial P_{3,r}^{G,j}}{\partial z^r} &= \frac{\partial L_{3,r}^{G,j}}{\partial z^r} = -\frac{z^s - z^r}{\rho}, \\ \frac{\partial P_{3,r}^{G,j}}{\partial c \tilde{dt}_r^G} &= \frac{\partial L_{3,r}^{G,j}}{\partial c \tilde{dt}_r^G} = 1, \\ \frac{\partial P_{3,r}^{G,j}}{\partial Z_{wet}} &= \frac{\partial L_{3,r}^{G,j}}{\partial Z_{wet}} = M_{wet}(E), \\ \frac{\partial P_{3,r}^{G,j}}{\partial \lambda_3^G B_3^{G,j}} &= 0, \\ \frac{\partial L_{3,r}^{G,j}}{\partial \lambda_3^G B_3^{G,j}} &= 1 \end{aligned}$$

The complete design matrix, which consists of the Jacobians, is given for each satellite

as follow:

$$H = \begin{bmatrix} -\frac{x^s - x_0^r}{\rho_0} & -\frac{y^s - y_0^r}{\rho_0} & -\frac{z^s - z_0^r}{\rho_0} & 1 & M_{wet}(E) & 0 & \dots \\ -\frac{x^s - x_0^r}{\rho_0} & -\frac{y^s - y_0^r}{\rho_0} & -\frac{z^s - z_0^r}{\rho_0} & 1 & M_{wet}(E) & 1 & \dots \end{bmatrix}$$

4.2.2. Stochastic Modelling

Kalman filter requires the statistical characteristics of estimated parameters as well as the statistical properties of measurements. The well-defined statistical behaviour of both measurement and parameter pave the way to achieve a appropriate solution. The general way to specify the statistical properties of the measurements is to construct the observation covariance matrix which is indicated by R in Equation (4.21). Moreover, the kinematic behaviour and variations of the parameters with time determine the stochastic properties of the estimated parameters.

Because the traditional PPP approach employs the ionosphere-free combinations, the error propagation law must be applied to obtain the variances of the linear combinations as follows:

$$\sigma_{P_{IF}}^2 = \left(\frac{f_1^2}{f_1^2 - f_2^2} \right) \sigma_{P_1}^2 + \left(\frac{f_2^2}{f_1^2 - f_2^2} \right) \sigma_{P_2}^2 = 6.481 \sigma_{P_1}^2 + 2.389 \sigma_{P_2}^2 \quad (4.38)$$

$$\sigma_{L_{IF}}^2 = \left(\frac{f_1^2}{f_1^2 - f_2^2} \right) \sigma_{L_1}^2 + \left(\frac{f_2^2}{f_1^2 - f_2^2} \right) \sigma_{L_2}^2 = 6.481 \sigma_{L_1}^2 + 2.389 \sigma_{L_2}^2 \quad (4.39)$$

where $\sigma_{P_1}^2$ and $\sigma_{P_2}^2$ are the variances of pseudorange observations on frequency 1 and 2, respectively and $\sigma_{L_1}^2$ and $\sigma_{L_2}^2$ indicate the variances of carrier phase observations on on frequency 1 and 2, respectively. The variances of ionosphere-free combinations ($\sigma_{P_{IF}}^2, \sigma_{L_{IF}}^2$) constitute the diagonal components of the observation covariance matrix (R). The off-diagonal elements of observation covariance matrix are zero since the phase and code observations are presumed to be uncorrelated.

Apart from the systematic errors and biases, the code and phase pseudoranges are influenced by random noises. The most of the random noises consists of the actual observation noise and multipath effect. The multipath is frequency dependent and its effect is much lower on carrier phases than code pseudoranges. Furthermore, the pseudorange observable has considerably greater wavelength than the carrier phase observable. As a consequence, the code observations has the relatively larger level of

noise in comparison with the phase observations [31]. Table 4.1 indicates typical noise levels of GPS observations.

Table 4.1: GPS observation noise levels [31].

Observation	Noise amount
Code pseudorange (Coarse acquisition)	10 cm to 300 cm
Code pseudorange (Precise)	10 cm to 30 cm
Carrier phase range	0.2 mm to 5 mm

An additional consideration to take into account is that the noise level of GPS observations is directly related to satellite elevation angle. The multipath effect and ionospheric and tropospheric delays are considerably higher level at lower elevations [64]. Therefore, an elevation dependent model should be used to relate the noise level with the elevation angle (E) as follows:

$$k = \begin{cases} \sin^2 E, & E < 30 \\ \sin E, & E > 30 \end{cases} \quad (4.40)$$

$$\sigma_P^2 = \frac{\sigma_{P,0}^2}{k} \quad \text{and} \quad \sigma_L^2 = \frac{\sigma_{L,0}^2}{k}$$

where $\sigma_{P,0}^2$ and $\sigma_{L,0}^2$ indicate the initial variances of code and phase observations, respectively.

As previously stated, it is required to define the stochastic properties of estimated parameters as well as the stochastic characteristics of measurements in the Kalman filter. The prior uncertainty of estimated parameters and epoch-to-epoch variation of the dynamic model should be specified appropriately.

In the traditional PPP model, the state vector consists of three coordinate components, one receiver clock offset, one zenith wet tropospheric delay and ambiguity parameters as stated before. The expected values of estimated parameters constitute the initial state vector \hat{x}_0 . Assuming there is no correlation between components of the state vector, the initial covariance matrix P_0 includes only diagonal elements.

On the other hand, it is quite difficult to define the behaviour of dynamic model correctly. While Coordinate components, zenith wet tropospheric delay and receiver clock offset might be modelled by using random walk process, carrier phase ambiguity parameters are assumed to be constant if there is no cycle slip. The differential equation

of the system dynamics for random walk process is given by the following equation as:

$$\dot{x}(t) = F(t) x(t) + w(t), \quad w(t) \approx q(t) \quad (4.41)$$

where $F(t)$ is the system dynamic matrix, $w(t)$ is the random white noise which is defined by the spectral density matrix $q(t)$. The propagation of the system dynamic covariance matrix can be simplified as follow [65]:

$$Q = \int_0^{\Delta t} A(t) q(t) A(t)^T \quad (4.42)$$

where Q is the process noise matrix, Δt is the time difference and $A(t)$ is the transition matrix.

In static positioning, the transition matrix for the station coordinates is an identity matrix and the noise matrix can be depicted as:

$$Q_{pos} = \begin{bmatrix} q_X \Delta t & 0 & 0 \\ 0 & q_Y \Delta t & 0 \\ 0 & 0 & q_Z \Delta t \end{bmatrix} \quad (4.43)$$

where q_X , q_Y , q_Z are the spectral densities of position components.

Similarly, the transition matrix for the receiver clock offset and zenith wet tropospheric delay is still an identity matrix and the process noise of these parameters are given as follows:

$$Q_{clock} = \begin{bmatrix} q_{clock} \Delta t \end{bmatrix} \quad (4.44)$$

$$Q_{trop} = \begin{bmatrix} q_{trop} \Delta t \end{bmatrix} \quad (4.45)$$

where q_{clock} and q_{trop} are spectral density of the receiver clock and zenith wet tropospheric delay, respectively. The stochastic properties of the estimated parameters indicated in Table 4.2 can be used for the Kalman filter [16, 66].

4.2.3. Quality Control

One of the essential steps of the filtering process is to validate the filter performance which is directly related to the measurements because the Kalman filter updates the state vector at each epoch using the measurements. Because of the recursive character,

Table 4.2: Stochastic properties of the estimated parameter for traditional PPP approach

Component	Model	Spectral Density
Position	Random Walk	0 (in static mode)
Receiver Clock Offset	Random Walk	$1 \times 10^5 \text{ m}^2/\text{sec}$
Tropospheric zenith wet delay	Random Walk	$1 \times 10^{-9} \text{ m}^2/\text{sec}$
Phase ambiguities	Constant	0

any error in the measurements deteriorates the filtering performance for the subsequent epochs. Consequently, it is required to detect and tolerate the erroneous measurements.

The erroneous measurements can result from the multipath, cycle slip, receiver clock jump and other error sources. How to deal with the cycle slip and clock jump is comprehensively explained in the previous chapter. However, it is essential to control the consistency of measurements with the stochastic model. The innovation sequence vector which describes the difference between the predicted and actual measurements is typically employed to detect the inconsistency as follows:

$$v_k = z_k - h(\hat{x}_k, 0) \quad (4.46)$$

where z_k is the actual measurements and h is the measurement model.

The innovation sequence must follow the normal distribution for an optimal filter. Therefore, the innovation sequence typically reflects the effect of erroneous measurements. Firstly, a global statistical test is conducted to determine whether the innovations are Gaussian. If any anomaly is identified in the global test, a local statistical test should be conducted to distinguish which measurement is most likely erroneous. The measurement having the maximum local test value is presumed to be an outlier. The procedure of the global and local tests is summarized as follows [67].

Global Test:

$$T = v_k^T S_k v_k \mid T < \chi_\alpha^2(m_k, 0) \quad (4.47)$$

Local Test:

$$w = \frac{(v_k)_i}{\sqrt{(S_k)_{ii}}} \quad (4.48)$$

where,

S_k	$= R_k + H_k P_k^- H_k^T$
α	: level of significant
m_k	: degrees of freedom
$\chi_\alpha^2(m_k, 0)$: upper α probability point of the Chi-squared distribution
H_k	: design matrix
R_k	: observation covariance matrix
P_k^-	: predicted parameter covariance matrix

4.3. Multi-GNSS PPP Approach

Although traditional PPP approach globally provides centimetre-level positioning accuracy, the convergence time is still the main limitation of PPP. The ambiguity parameter in traditional PPP, as previously described, is a float number and named float ambiguity, therefore the initializing time, i.e. convergence time, is pretty long. In general, it approximately takes 20 minutes for positioning solution to achieve 20 centimetres or better horizontal accuracy in static mode [35]. The positioning accuracy and convergence time mainly depend on the user environment, the observation session length and the geometry and number of the visible satellites.

Due to independent, unlimited and highly precise positioning ability, PPP has received much attention in recent years. However, it is not preferable for a wide range of real-time GNSS applications because of the restriction caused by the convergence time. Over the last decade, much effort has been made to shorten the convergence period with ambiguity resolution methods. These methods are pretty successful to reduce the convergence time, but they can be applied only if external corrections, which are mainly obtained from a network solution, are available. This method is typically named ambiguity-fixed solution and requires a service provider to obtain the related corrections [10, 11, 12, 13]. On the other hand, additional satellite resources make it possible to optimize the satellite geometry and therefore to accelerate the convergence speed. After achieving the full operational capability, GLONASS has provided additional satellite resources to GNSS users. Some researchers which examine the performance of combined GPS/GLONASS PPP confirmed that the additional satellites enhance the PPP performance as regards convergence time and accuracy [16, 17, 18]. Additionally, with the emergence of the additional navigation systems like the Chi-

nese BeiDou and European Galileo, the multi-GNSS PPP including four constellations has been studied in recent years [19, 20]. The first results suggest that the combined multi-GNSS has a potential to enhance the PPP performance significantly. However, it is still required to validate the multi-GNSS PPP performance with further research in various aspects.

Although the combined multi-GNSS provides an opportunity to enhance the PPP performance, it entails new modelling approaches and more complex processing strategies. There are some differences between the navigation systems, in terms of the spatial reference definition, working signal properties, applied corrections to hardware biases and accuracy of precise products. Therefore, it is needed to deduce new functional and stochastic models which ensure the integration of Multi-GNSS.

4.3.1. Functional Model

Because each navigation system uses its own spatial reference frame for positioning (see Chapter 2.1), the coordinate system transformation must be performed to combine the navigation systems. The other option to ensure the compatibility of reference systems is to employ the precise products generated in the same reference system. Fortunately, IGS provides the precise products for GNSS within the scope of MGEX project. For the multi-GNSS process, the MGEX products given in Table 3.2 can be utilized to eliminate the satellite orbit error and clock error which includes the satellite code hardware bias.

Similar to the traditional PPP approach, the ionosphere-free combinations are employed to remove the first-order ionospheric effect in the multi-GNSS PPP model, whose observation equations are written as follows:

$$\begin{aligned} P_{3,r}^{G,j} &= \rho_r^{G,j} + c \tilde{d}t_r^G + Z_{wet} M_{wet}(E) + \varepsilon(P_{3,r}^G) \\ L_{3,r}^{G,j} &= \rho_r^{G,j} + c \tilde{d}t_r^G + Z_{wet} M_{wet}(E) + \lambda_3^G B_3^{G,j} + \varepsilon(L_{3,r}^G) \end{aligned} \quad (4.49)$$

$$\begin{aligned} P_{3,r}^{R,j} &= \rho_r^{R,j} + c \tilde{d}t_r^R + Z_{wet} M_{wet}(E) + \varepsilon(P_{3,r}^R) \\ L_{3,r}^{R,j} &= \rho_r^{R,j} + c \tilde{d}t_r^R + Z_{wet} M_{wet}(E) + \lambda_3^R B_3^{R,j} + \varepsilon(L_{3,r}^R) \end{aligned} \quad (4.50)$$

$$\begin{aligned} P_{3,r}^{E,j} &= \rho_r^{E,j} + c \tilde{d}t_r^E + Z_{wet} M_{wet}(E) + \varepsilon(P_{3,r}^E) \\ L_{3,r}^{E,j} &= \rho_r^{E,j} + c \tilde{d}t_r^E + Z_{wet} M_{wet}(E) + \lambda_3^E B_3^{E,j} + \varepsilon(L_{3,r}^E) \end{aligned} \quad (4.51)$$

$$\begin{aligned} P_{3,r}^{C,j} &= \rho_r^{C,j} + c \tilde{d}t_r^C + Z_{wet} M_{wet}(E) + \varepsilon(P_{3,r}^C) \\ L_{3,r}^{C,j} &= \rho_r^{C,j} + c \tilde{d}t_r^C + Z_{wet} M_{wet}(E) + \lambda_3^C B_3^{C,j} + \varepsilon(L_{3,r}^C) \end{aligned} \quad (4.52)$$

where G , R , E and C indicate GPS, GLONASS, GALILEO and BDS respectively.

Unlike other navigation systems, there exist various hardware biases in the GLONASS receiving channels due to FDMA method, which utilizes the distinct frequency channel for each satellite. Hence, the hardware biases are denoted as a sum of an average term and a frequency-dependent term as follows:

$$\begin{aligned} b_{P_{i,r}}^R &= b_{P_{i,r}}^{R,avg} + \delta b_{P_{i,r}}^R \\ b_{L_{i,r}}^R &= b_{L_{i,r}}^{R,avg} + \delta b_{L_{i,r}}^R \end{aligned} \quad (4.53)$$

where $b_{P_{i,r}}^{R,avg}$ and $b_{L_{i,r}}^{R,avg}$ are the average receiver hardware biases for code and phase, respectively; $\delta b_{P_{i,r}}^R$ and $\delta b_{L_{i,r}}^R$ are the inter-frequency biases (IFB) [68].

At this stage, it is not required to consider the satellite-related hardware biases because the phase biases have been eliminated in the receiver clock offset and the code biases contaminated into the ambiguity parameter. As for the receiver, the average code hardware bias is absorbed by the receiver clock offset. If Equation (4.53) are embedded into Equation (4.50), GLONASS observations can be rewritten as:

$$\begin{aligned} P_{3,r}^{R,j} &= \rho_r^{R,j} + c \tilde{d}t_r^R + Z_{wet} M_{wet}(E) + \delta b_{P_{3,r}}^R + \varepsilon(P_{3,r}^R) \\ L_{3,r}^{R,j} &= \rho_r^{R,j} + c \tilde{d}t_r^R + Z_{wet} M_{wet}(E) + \lambda_3^R B_3^{R,j} + \varepsilon(L_{3,r}^R) \\ \tilde{d}t_r^R &= dt_r^R + b_{P_{3,r}}^{R,avg} \\ \lambda_3^R B_3^{R,j} &= \lambda_3^G N_3^{G,j} + (b_{L_{3,r}}^{R,avg} + \delta b_{L_{3,r}}^R - b_{P_{3,r}}^{R,avg}) - (b_{L_3}^{G,j} - b_{P_3}^{G,j}) \end{aligned} \quad (4.54)$$

As it can be seen in the above equations, the GLONASS code pseudorange observation contains the inter-frequency code bias ($\delta b_{P_{3,r}}^R$) parameter additionally. The IFBs may be estimated in state vector, but this is usually not preferable because too many unknowns weaken the model structure. Therefore, IFB parameters can be ignored in the multi-GNSS model if only the pseudoranges take the quite smaller weight in comparison with phase observations [16, 69].

On the other hand, if the equations from 4.49 to 4.52 are directly employed, there will be many receiver clock offset parameters to be estimated. Instead, a more suitable way is to introduce the system time bias parameters which reflect the time differences between the other navigation systems and GPS [16, 19]. If the system bias parameters are introduced according to the GPS receiver clock offset, the observation equations of GLONASS, Galileo and BDS are given as:

$$\begin{aligned} P_{3,r}^{R,j} &= \rho_r^{R,j} + c(\tilde{d}t_r^G + ISB_r^R) + Z_{wet} M_{wet}(E) + \varepsilon(P_{3,r}^R) \\ L_{3,r}^{R,j} &= \rho_r^{R,j} + c(\tilde{d}t_r^G + ISB_r^R) + Z_{wet} M_{wet}(E) + \lambda_3^R B_3^{R,j} + \varepsilon(L_{3,r}^R) \end{aligned} \quad (4.55)$$

$$\begin{aligned}
P_{3,r}^{E,j} &= \rho_r^{E,j} + c(\tilde{d}t_r^G + ISB_r^E) + Z_{wet} M_{wet}(E) + \varepsilon(P_{3,r}^E) \\
L_{3,r}^{E,j} &= \rho_r^{E,j} + c(\tilde{d}t_r^G + ISB_r^E) + Z_{wet} M_{wet}(E) + \lambda_3^E B_3^{E,j} + \varepsilon(L_{3,r}^E)
\end{aligned} \tag{4.56}$$

$$\begin{aligned}
P_{3,r}^{C,j} &= \rho_r^{C,j} + c(\tilde{d}t_r^G + ISB_r^C) + Z_{wet} M_{wet}(E) + \varepsilon(P_{3,r}^C) \\
L_{3,r}^{C,j} &= \rho_r^{C,j} + c(\tilde{d}t_r^G + ISB_r^C) + Z_{wet} M_{wet}(E) + \lambda_3^C B_3^{C,j} + \varepsilon(L_{3,r}^C)
\end{aligned} \tag{4.57}$$

where ISB_r^R , ISB_r^E and ISB_r^C are GPS/GLONASS, GPS/GALILEO and GPS/BDS system time bias parameters, respectively.

In the multi-GNSS model, the unknown parameters include the three position coordinate components, one receiver clock bias, three inter system time biases, one zenith wet tropospheric delay component and one real-valued ambiguity parameters for each of the observed satellites. The state vector is given by:

$$x = [x^r, y^r, z^r, c\tilde{d}t_r^G, ISB_r^R, ISB_r^E, ISB_r^C, Z_{wet}, \lambda_3^G B_3^{G,1}, \lambda_3^G B_3^{G,2}, \dots] \tag{4.58}$$

Like the traditional model, the design matrix of the multi-GNSS model is composed of the Jacobians of the observation model according to the estimated parameters. Jacobians of the inter-system time bias parameters are given by:

$$\begin{aligned}
\frac{\partial P_{3,r}^{s,j}}{\partial cISB_r^R} = \frac{\partial L_{3,r}^{s,j}}{\partial cISB_r^R} &= \begin{cases} 0 & \text{GPS, GALILEO and BDS satellites} \\ 1 & \text{GLONASS satellites} \end{cases} \\
\frac{\partial P_{3,r}^{s,j}}{\partial cISB_r^E} = \frac{\partial L_{3,r}^{s,j}}{\partial cISB_r^E} &= \begin{cases} 0 & \text{GPS, GLONASS and BDS satellites} \\ 1 & \text{GALILEO satellites} \end{cases} \\
\frac{\partial P_{3,r}^{s,j}}{\partial cISB_r^C} = \frac{\partial L_{3,r}^{s,j}}{\partial cISB_r^C} &= \begin{cases} 0 & \text{GPS, GALILEO and GALILEO satellites} \\ 1 & \text{BDS satellites} \end{cases}
\end{aligned}$$

The Jacobians of other estimated parameters are the same as given in the traditional PPP model.

4.3.2. Stochastic Modelling

It is essential to describe the stochastic models appropriately for achieving an optimal solution in the Kalman filter. Determining statistical behaviour of both measurements and estimated parameters in multi-GNSS data processing is complicated because the combined GNSS model involves different kinds of measurements and parameters. Therefore, the covariance matrix of measurements and the variations of the parameters

with time should be handled carefully in the multi-GNSS model.

Akin to the traditional model, the measurement covariance matrix is composed of only diagonal elements assuming there is no correlation between the measurements. The diagonal elements of the covariance matrix are the variances of the ionosphere-free combinations calculated from Equation (4.38) and Equation (4.39), whereas off-diagonal elements are zero. As given in Equation (4.40), it is recommended to employ the weight model which depends on satellite elevation angle due to high amount of multi-path and noise effect at low elevation angles. The covariance matrix for ionosphere-free combinations of all GPS satellites is given as follows:

$$\Sigma\varepsilon_G = \begin{bmatrix} \sigma_{P,G1}^2 & 0 & 0 & 0 & 0 & 0 & 0 & 0 \\ 0 & \sigma_{L,G1}^2 & 0 & 0 & 0 & 0 & 0 & 0 \\ 0 & 0 & \ddots & 0 & 0 & 0 & 0 & 0 \\ 0 & 0 & 0 & \sigma_{P,Gk} & 0 & 0 & 0 & 0 \\ 0 & 0 & 0 & 0 & \sigma_{L,Gk} & 0 & 0 & 0 \\ 0 & 0 & 0 & 0 & 0 & \ddots & 0 & 0 \\ 0 & 0 & 0 & 0 & 0 & 0 & \sigma_{P,Gn} & 0 \\ 0 & 0 & 0 & 0 & 0 & 0 & 0 & \sigma_{L,Gn} \end{bmatrix} \quad (4.59)$$

Similarly, the covariance matrices of GLONASS, Galileo and BDS can be demonstrated by $\Sigma\varepsilon_R$, $\Sigma\varepsilon_E$ and $\Sigma\varepsilon_C$, respectively.

Typically, a ratio between code and phase observations, which is usually equal 100, are used to weight the different observations in the same system. However, the covariance matrix should reflect the weight of measurements obtained from different navigation systems. Unlike the other navigation systems, GLONASS utilizes the FDMA signal method. Hence, GLONASS code observations contain the receiver and satellite-dependent inter-channel biases (ICBs). The ICBs can't be embedded into receiver clock offset because they differ for each satellite. It is recommended to assign small weights to the GLONASS code measurements because the accuracy of GLONASS code measurements is lower than GPS ones [16].

Additionally, the quality of the orbit and clock products are not at the same level for all navigation systems. The MGEX precise products of GPS and GLONASS are

generally at the same level as the standard IGS products. In addition, Galileo and BDS products have poorer quality relative to GPS and GLONASS products [29]. Thus, it is required to reflect the quality difference between the precise products on the measurement covariance matrix. The initial variance ratio among the four systems can be employed as follows:

$$\begin{aligned}\sigma_{P,G}^2 : \sigma_{P,R}^2 : \sigma_{P,E}^2 : \sigma_{P,C}^2 &= 1 : 4 : 4 : 4 \\ \sigma_{L,G}^2 : \sigma_{L,R}^2 : \sigma_{L,E}^2 : \sigma_{L,C}^2 &= 1 : 1 : 4 : 4\end{aligned}\tag{4.60}$$

In the multi-GNSS PPP model, there are additional three parameters to be estimated, which are inter-system time biases. Random Walk process is employed to model these parameters with the spectral density value $10^{-7} \text{ m}^2/\text{sec}$ [16, 66].

4.3.3. Quality Control

The quality check procedure described in Subsection 4.2.3 can be implemented into the multi-GNSS PPP model for validating the Kalman filter performance.

4.4. Further Improvements

The exact description of both functional and stochastic models is essential to reach an optimal solution in the implementation of the Kalman filter on PPP process. Traditionally, the ionosphere-free combinations are employed as the functional model for PPP. Although the functional model is well-known for PPP, it is pretty tough to determine the stochastic properties appropriately. The Kalman filter requires initial values of the estimated parameters and their initial covariances apart from the observation data. A good initial knowledge of both process and measurements assists Kalman filter in achieving an optimal solution, while insufficient or inexact a priori knowledge weakens the precision of the PPP estimates. On the other hand, outliers and incorrectly weighted measurements influence the filter performance adversely.

An adaptive robust Kalman filtering method, which introduces an equivalent covariance matrix and an adaptive factor, can be applied for PPP processing [70, 71, 72]. In addition to adaptive robust Kalman filtering method, an alternative method to determine the initial values of the unknown parameters and their covariance matrix are presented in this section.

4.4.1. Adaptive Robust Kalman Filter

Compared with the classical Kalman filter, an equivalent weight matrix and an adaptive factor are additionally introduced in the adaptive robust Kalman filter (ARKF) process. The equivalent weight matrix is responsible for tolerating incorrectly weighted observations. Additionally, the adaptive factor balances the contribution of state-space. Essentially, ARKF is a combination of the robust estimation and adaptive filter, and its recursive equations are expressed by the following simple form:

$$\hat{x}_k^- = f(\hat{x}_{k-1}, 0) \quad (4.61)$$

$$P_k^- = A_k P_{k-1} A_k^T + W_k Q_{k-1} W_k^T \quad (4.62)$$

$$K_k = \frac{1}{\alpha_k} P_k^- H_k^T \left(\frac{1}{\alpha_k} H_k P_k^- H_k^T + \bar{R}_k \right)^{-1} \quad (4.63)$$

$$\hat{x}_k = \hat{x}_k^- + K_k (z_k - h(\hat{x}_k^-, 0)) \quad (4.64)$$

$$P_k = [I - K_k H_k] P_k^- [I - K_k H_k]^T + K_k \bar{R}_k K_k^T \quad (4.65)$$

where \bar{R}_k denotes the equivalent covariance matrix of measurements, α_k is an adaptive factor ($0 < \alpha \leq 1$) and the other terms are the same as given previously [72].

The main difference between the adaptive robust and classical Kalman filters is the computation of the Kalman gain matrix (Equation (4.63)). In the classical Kalman filter, the observations are either accepted or rejected according to a statistical test. It means that the observation weight is either set as one or zero. Instead, a continuous weighting function ranging from zero to one is utilized in the robust estimation.

The equivalent covariance matrix of measurements can be computed using the improved IGG (Institute of Geodesy and Geophysics) III function as given the following equations: [71, 72]

$$\bar{R}_i = R_i / \gamma_i \quad (4.66)$$

$$\gamma_i = \begin{cases} 1 & |\tilde{v}_i| \leq k_0 \\ \frac{k_0}{|\tilde{v}_i|} \left(\frac{k_1 - |\tilde{v}_i|}{k_1 - k_0} \right)^2 & k_0 < |\tilde{v}_i| \leq k_1 \\ 0 & |\tilde{v}_i| > k_1 \end{cases} \quad (4.67)$$

where γ_i is the variance inflation factor, \tilde{v}_i is the standardized posterior residual, k_0 and k_1 are two thresholds which are usually chosen as $k_0 = 1.5 \sim 3.0$ and $k_1 = 3.0 \sim 8.0$. In contrast to the original version, the improved filtering scheme conducts equivalent variance function for only the measurement with largest standardized residual instead

of all measurements in each iteration.

In addition to the equivalent covariance matrix, an proper adaptive factor shall be constructed to balance the influences of measurements and dynamic model. A three-segment function depending on innovation-based statistics is presented by:

$$\bar{V}_k = \frac{\sum_{i=1}^{n_k} \tilde{v}_k}{\sum_{i=1}^{n_k} \sigma_{V_k}^2} \quad (4.68)$$

$$\alpha_k = \begin{cases} 1 & |\bar{V}_k| \leq c_0 \\ \frac{c_0}{|\bar{V}_k|} \left(\frac{c_1 - |\bar{V}_k|}{c_1 - c_0} \right)^2 & c_0 < |\bar{V}_k| \leq c_1 \\ 0 & |\bar{V}_k| > c_1 \end{cases} \quad (4.69)$$

where \tilde{v}_k is the innovation, $\sigma_{V_k}^2$ is the standard deviation of innovation, c_0 and c_1 are two thresholds which are usually chosen as $k_0 = 1.5 \sim 3.0$ and $k_1 = 3.0 \sim 8.0$ [72].

The adaptive robust Kalman filter has recently received attention in many GNSS applications [70, 71, 73]. As for PPP, much effort has been made to enhance the effectiveness of filtering solution through the adaptive robust Kalman filter. Moreover, many studies have shown that the implementation of the adaptive robust Kalman filter in PPP processing influences filtering performance positively as compared to the classical Kalman filter [72, 74]. In this study, the adaptive robust Kalman filter scheme explained above is applied.

4.4.2. Initialisation of Kalman Filter

As previously mentioned, Kalman filter requires the specification of initial values in a proper way [62]. In the implementation of Kalman filter on PPP, insufficient or wrong prior knowledge not only degrades the precision of the PPP estimates but also it may lead to a failure of PPP solution. Unfortunately, a proper initial knowledge reflecting the system dynamic is difficult to be obtained in most GNSS applications because measurement quality and process dynamics vary depending on the application.

Herein an innovative method, which reflects the initial system dynamics appropriately, is suggested to obtain a priori knowledge of the process. This method involves the computation of initial parameters and their covariances using least squares adjustment in the first epoch. Because least square independently determines the unknown parameters, estimated parameters are very close to actual values and represent the initial

system dynamics in a proper way. Moreover, it is not required an extra information about the system to perform least squares adjustment.

Least squares solution is simply given as follows [31]:

$$\hat{x} = (A^T W A)^{-1} A^T W Z = N^{-1} A^T W Z \quad (4.70)$$

where \hat{x} is the vector of unknowns, A is the design matrix, Z is the observation matrix, W is the weight matrix of observations and N denotes the normal equation matrix. The cofactor matrix of the estimated parameter vector is given by:

$$Q_{\hat{x}} = N^{-1} \quad (4.71)$$

The residuals (\tilde{v}), the a posteriori variance of unit weight ($\tilde{\sigma}_0^2$) and the covariance matrix of the estimated parameters ($\Sigma_{\hat{x}}$) can be calculated as follows:

$$\tilde{v} = Z - A\hat{x} \quad (4.72)$$

$$\tilde{\sigma}_0^2 = \frac{\tilde{v}^T W \tilde{v}}{n - u} \quad (4.73)$$

$$\Sigma_{\hat{x}} = \tilde{\sigma}_0^2 Q_{\hat{x}} \quad (4.74)$$

where n is the number of measurements and u indicates the number of unknown parameters, respectively.

The functional and stochastic models given for both traditional and multi-GNSS PPP approaches can be used for least squares adjustment as well. However, the functional models of PPP are non-linear, and thus a linearisation process using a Taylor expansion around the approximate position is required. After the linearisation step, the least squares method can estimate the unknown parameter iteratively. Finally, estimated parameter and its covariance matrix are utilized by the Kalman filter as the initial values.

5. SOFTWARE DEVELOPMENT

As a part of the thesis, a PPP software package, named PPPH, was developed to both design the PPP models and filtering techniques independently, and to evaluate the multi-GNSS PPP performance. Consequently, PPPH was designed to perform PPP process accepting data from GPS, GLONASS, Galileo and BeiDou. The theoretical background of the software is based on the models and methods described in the previous chapters.

PPPH was developed in MATLAB[®] environment due to its highly suitable architecture for technical computing. MATLAB is a high-level language for programming, computing, and visualization of data through its matrix-based structure and built-in graphics. PPPH only requires the installation of MATLAB in the related computer. However, MATLAB version should be 2016a or newer because the graphical user interface (GUI) of software was developed using the MATLAB App Designer which is a special environment to design and develop the visual components of a user interface. In addition to MATLAB core files, PPPH does not need any MATLAB toolbox.

PPPH fundamentally consists of five main components:

- Data importing,
- Preprocessing,
- Modelling,
- Filtering,
- Analysis

Each of the components and their options are represented by a related section in the GUI of PPPH. The sections will be briefly explained in this chapter.

5.1. Data Importing

There are several file formats designed to exchange data within the GNSS community. Navigation data required for performing PPP processing such as observations, satellite orbits, and clocks, etc. are provided in its specific file format as well. Before performing

PPP process, it is required to extract and make data ready to be utilized. For this reason, the first component of PPPH is to handle files and data appropriately. In PPPH, relevant data can be easily imported into the software using the data importing section indicated in Figure 5.1. This section allows users to specify five fundamental files for PPP, which are observation file, precise orbit file, antenna correction file, clock correction file and differential code bias file.

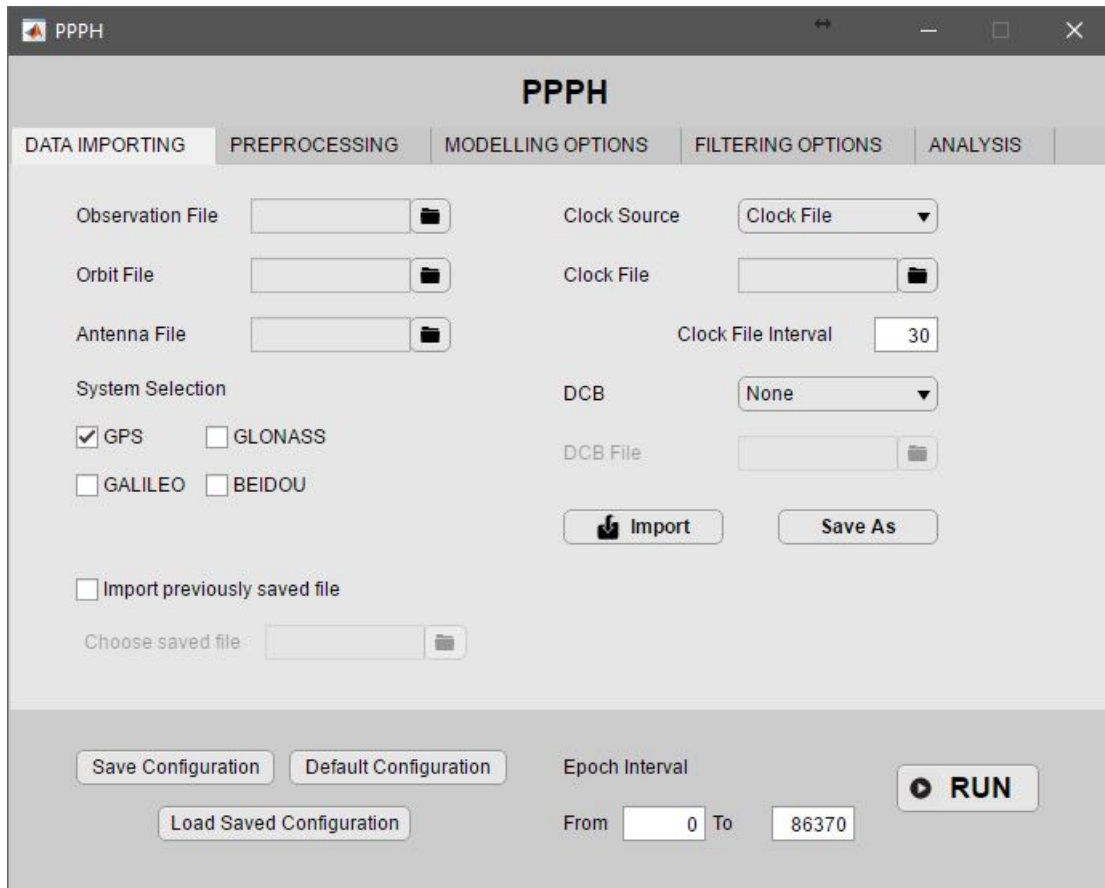


Figure 5.1: Data importing section of PPPH GUI.

The observation files use RINEX format as the standard exchange format, and PPPH is compatible with RINEX 2 and 3 versions. Additionally, PPPH can process files comprising GLONASS, Galileo, and BeiDou observations together with GPS observations. At this stage, it can be decided which system observations will be utilized for PPP process. When it comes to precise navigation data, SP3 is the standard format accepted by the GNSS community. In addition to SP3 files produced by IGS, PPPH is also compatible with MGEX products described in Section 3.1. PPPH can also process ANTEX files which contain the antenna PCOs and PCVs of satellites and receivers.

In addition to precise satellite positions, SP3 file contains satellite clock corrections. Nevertheless, it is not recommended to use satellite clock corrections obtained from the SP3 file for precise GNSS applications due to long sampling interval. As an alternative,

the CLK file including high-rate clock data can be used for satellite clock corrections. PPPH can process the CLK file if "Clock File" is selected as the clock source option. In the case of CLK file is used, its sampling interval has to be specified. Finally, the DCB file which contains differential code biases between P1 and C1 observations of satellites can be imported into PPPH if "P1-C1" is selected as DCB option. These last two files are optional for PPP processing, while first three files are obligatory.

5.2. Preprocessing

Raw data obtained from data importing section require a pre-processing step to mitigate gross errors and inconsistencies in the data. PPPH accepts user preferences related to this step through the preprocessing section shown in Figure 5.2. After preprocessing step, the data get completely ready for the filtering process.

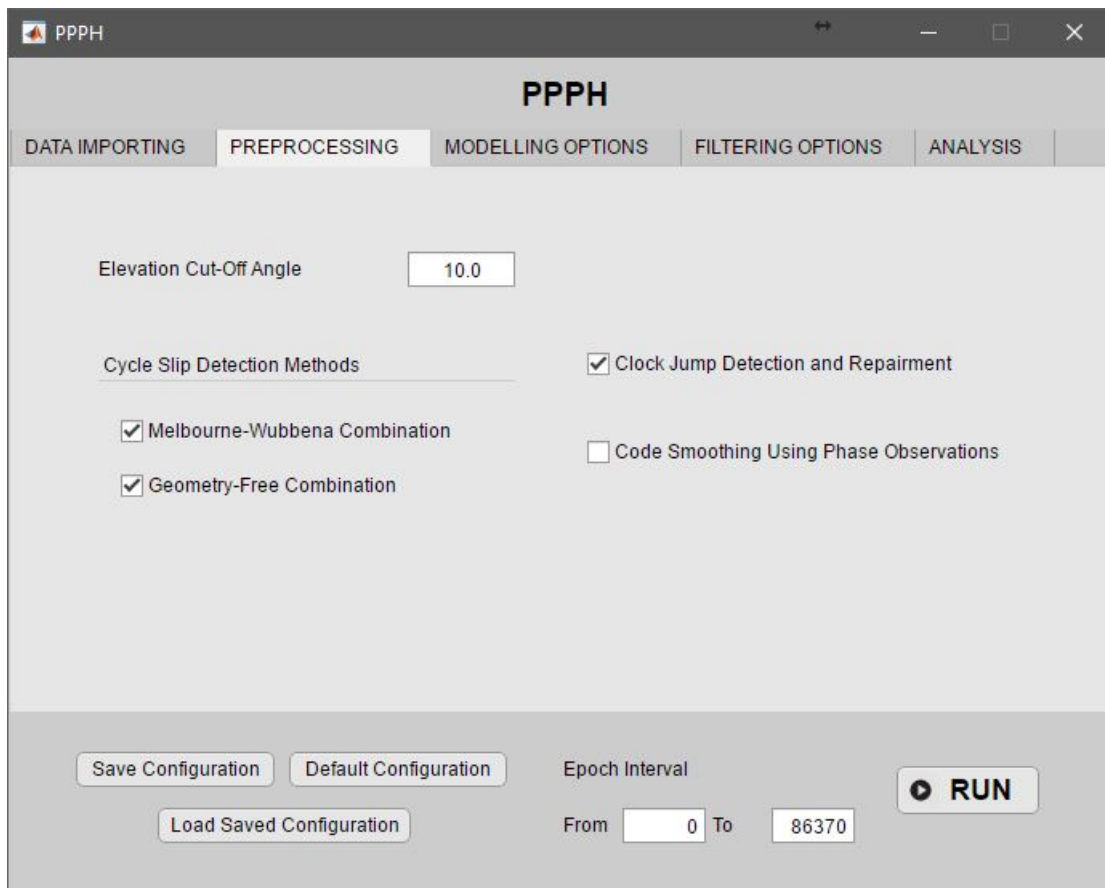


Figure 5.2: Preprocessing section of PPPH GUI.

Outliers in the data are detected and eliminated at the initial stage of the preprocessing step. Then, cycle slips in the phase measurements are detected and repaired using the algorithms described in Section 3.12. Herein, there are options to decide which cycle

slip methods will be applied. Moreover, there is an option to determine whether clock inconsistencies will be checked as described in Section 3.2. As well, PPPH provides a option whether or not the code observations will be smoothed with phase observations. The last choice in the preprocessing section is to specify the elevation cut-off angle.

5.3. Modelling Options

Modelling component of PPPH is responsible for calculating the corrections to mitigate the influence of error sources on GNSS measurements. These corrections are categorized into four groups in the modelling options section of PPPH depending on their effect (see Figure 5.3). Table 5.1 shows the correction types and handling strategies provided by PPPH. Because Chapter 3 explains the strategies to handle relevant error sources comprehensively, herein only corresponding sections are referred in the table.

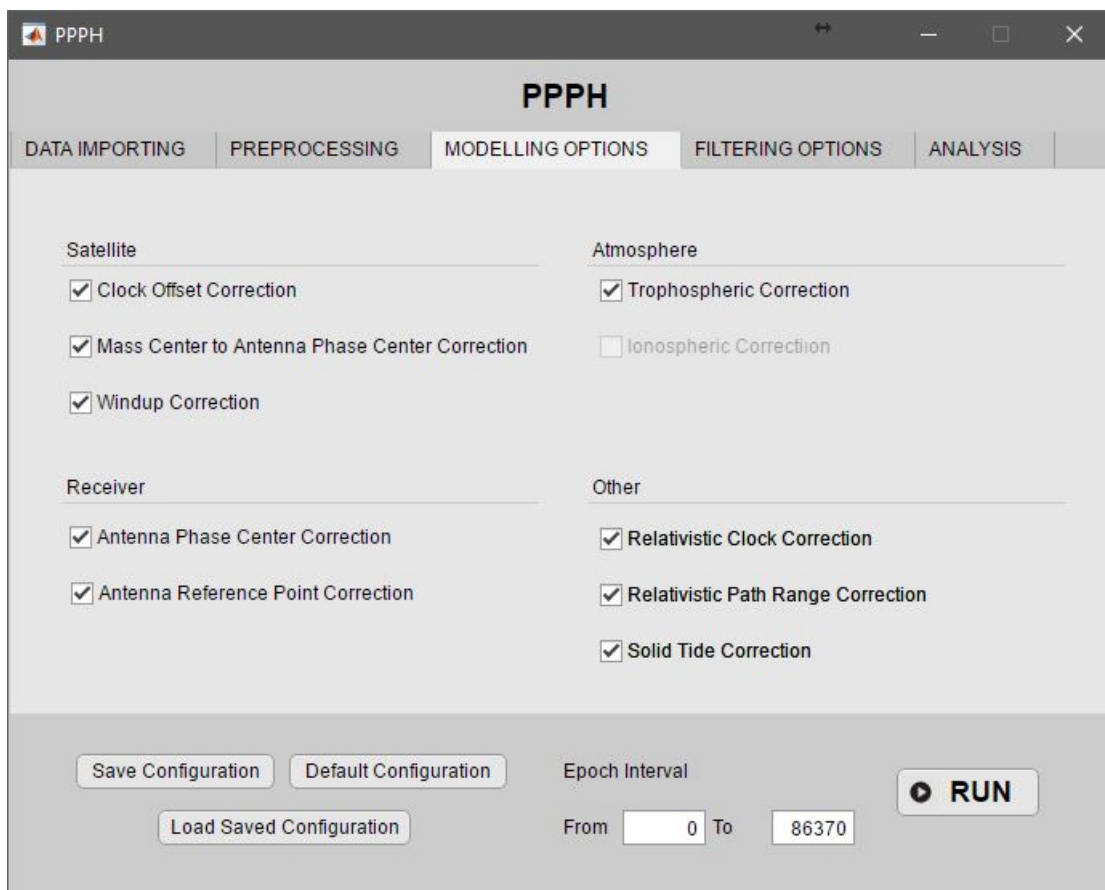


Figure 5.3: Modelling options section of PPPH GUI.

The corrections to be employed can be selected in modelling options section of PPH as can be seen in Figure 5.3. Thus, PPPH provides an opportunity to evaluate the impacts of corrections on the filtering solution separately.

Table 5.1: Corrections and handling strategies provided by the modelling sections of PPPH.

Category	Correction type	Handling strategy
Satellite	Clock offset	Section 3.1
	Antenna phase center	Section 3.6
	Wind-up	Section 3.7
Receiver	Antenna phase center	Section 3.6
	Antenna reference point	Section 3.6
Atmosphere	Ionosphere	Ionosphere-free comb.
	Troposphere	Section 3.3
Other	Relativistic clock	Section 3.5
	Relativistic path range	Section 3.5
	Solid tide	Section 3.8, 3.9, 3.10

5.4. Filtering Options

The adaptive robust Kalman filter is utilized in PPPH to estimate the state-space vector. The functional and stochastic models related about PPP are comprehensively described in the previous chapter. Accordingly, PPPH enables to specify the options and parameters of the Kalman filter through the filtering options section of GUI (see Figure 5.4).

In this section, there are two options to determine initial values of the Kalman filter; the selection of parameters manually and the determination of parameters using the least squares adjustment. Similarly, process uncertainty parameters can be manually determined. Moreover, a priori position can be defined in two ways if "*using least squares*" option is deactivated. One of these is to use approximate position obtained from the observation file, while the other is to specify position manually. Finally, standard deviations and weighting methods of the measurements can be defined in the filtering options section of GUI.

After all these selections, filtering process is started with the RUN button situated in the main screen for the interval specified by the user. An output file containing the results is created by PPPH at the end of the filtering process.

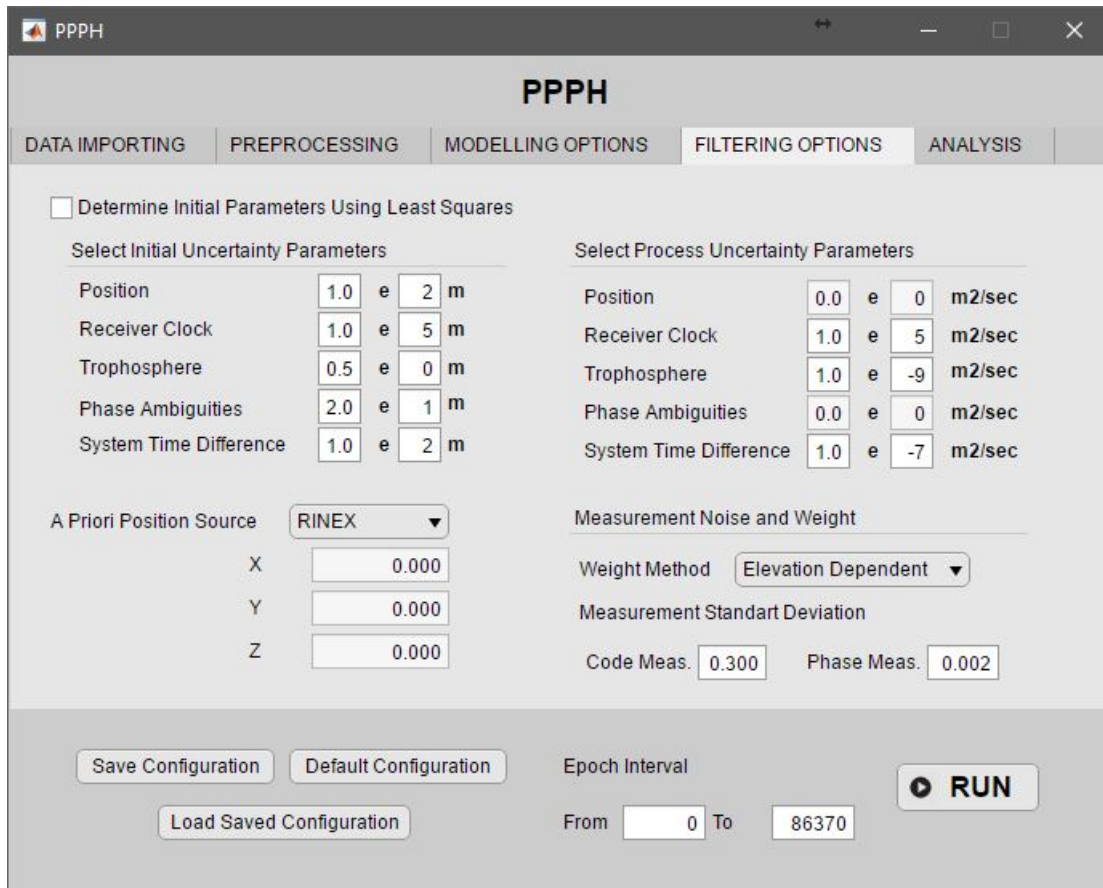


Figure 5.4: Filtering options section of PPPH GUI.

5.5. Analysis

The last component of PPPH is the analysis section as indicated in Figure 5.5. This section provides many tools to evaluate the qualities of filtering solution and data, comprehensively. First of all, it is essential to identify a reference point as a ground truth to calculate the statistics, such as accuracy, root mean square error and positioning error. Then, the accuracy and RMS values calculated in the local system appear in the section panel together with the convergence time.

To analyze the epoch-by-epoch variations of positioning error, PPPH provides three different plot options, which are ;

- NEU positioning error, which demonstrates the errors in north, east and up directions separately (Figure 5.6a),
- Horizontal positioning error (Figure 5.6b),
- 3D positioning error indicating the total spatial error (Figure 5.6c).

PPPH also enables to produce plots of receiver clock estimation, visible satellite number

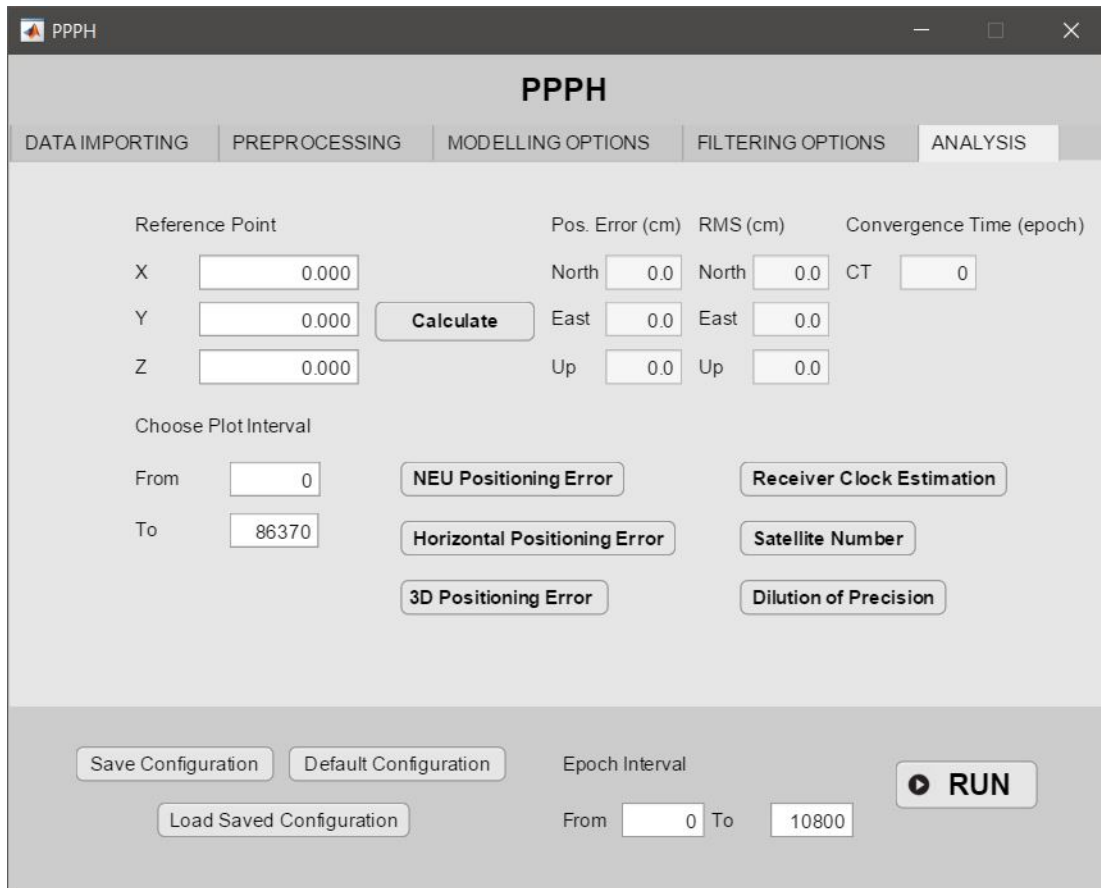
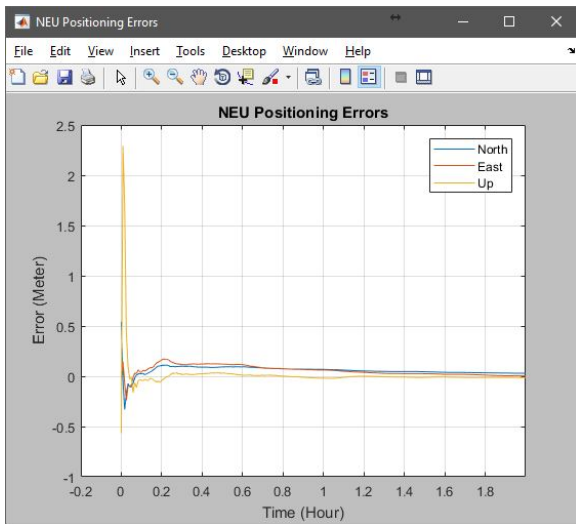


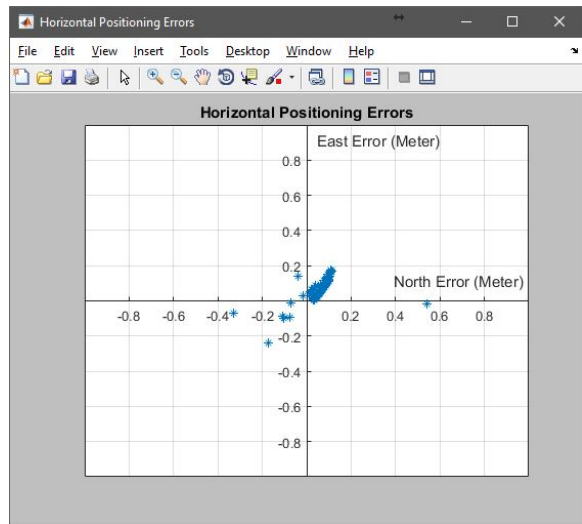
Figure 5.5: Analysis section of PPPH GUI.

and dilution of precision, example plots of which are given in Figure 5.7, respectively. By means of these tools, PPPH provides a possibility to evaluate not only the filtering performance but also the data quality.

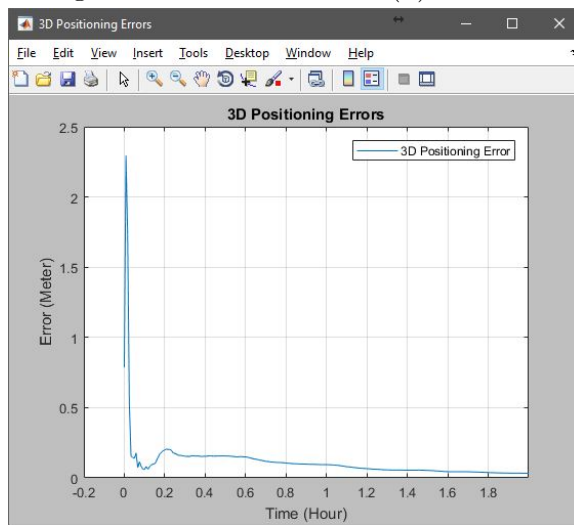
A flowchart for the basic procedure of PPPH processing, which represents the whole process step, is illustrated in Figure 5.8.



(a) NEU positioning error.

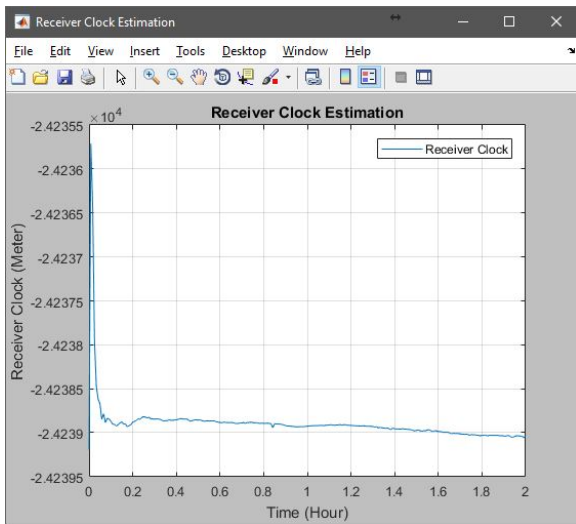


(b) Horizontal positioning error.

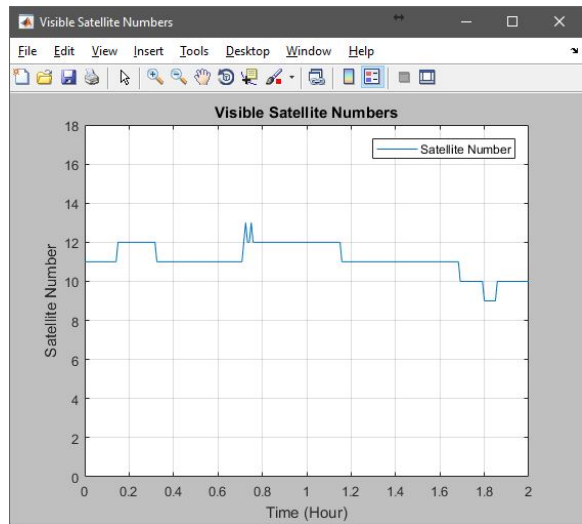


(c) 3D positioning error.

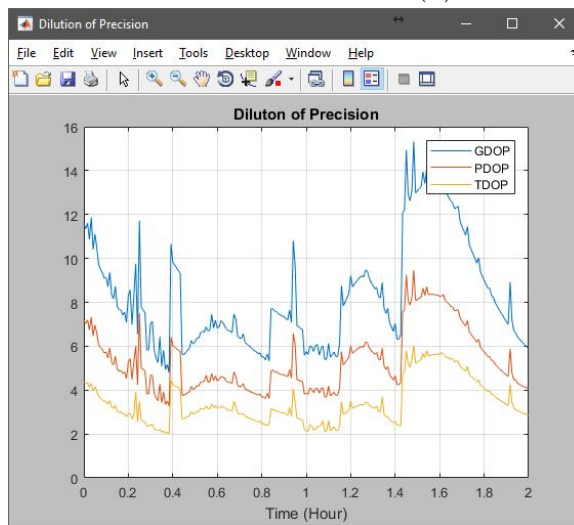
Figure 5.6: Examples of the positioning error plots generated by PPPH.



(a) Receiver clock estimation.



(b) Visible satellite number.



(c) Dilution of precision.

Figure 5.7: Examples of additional plots generated by PPPH.

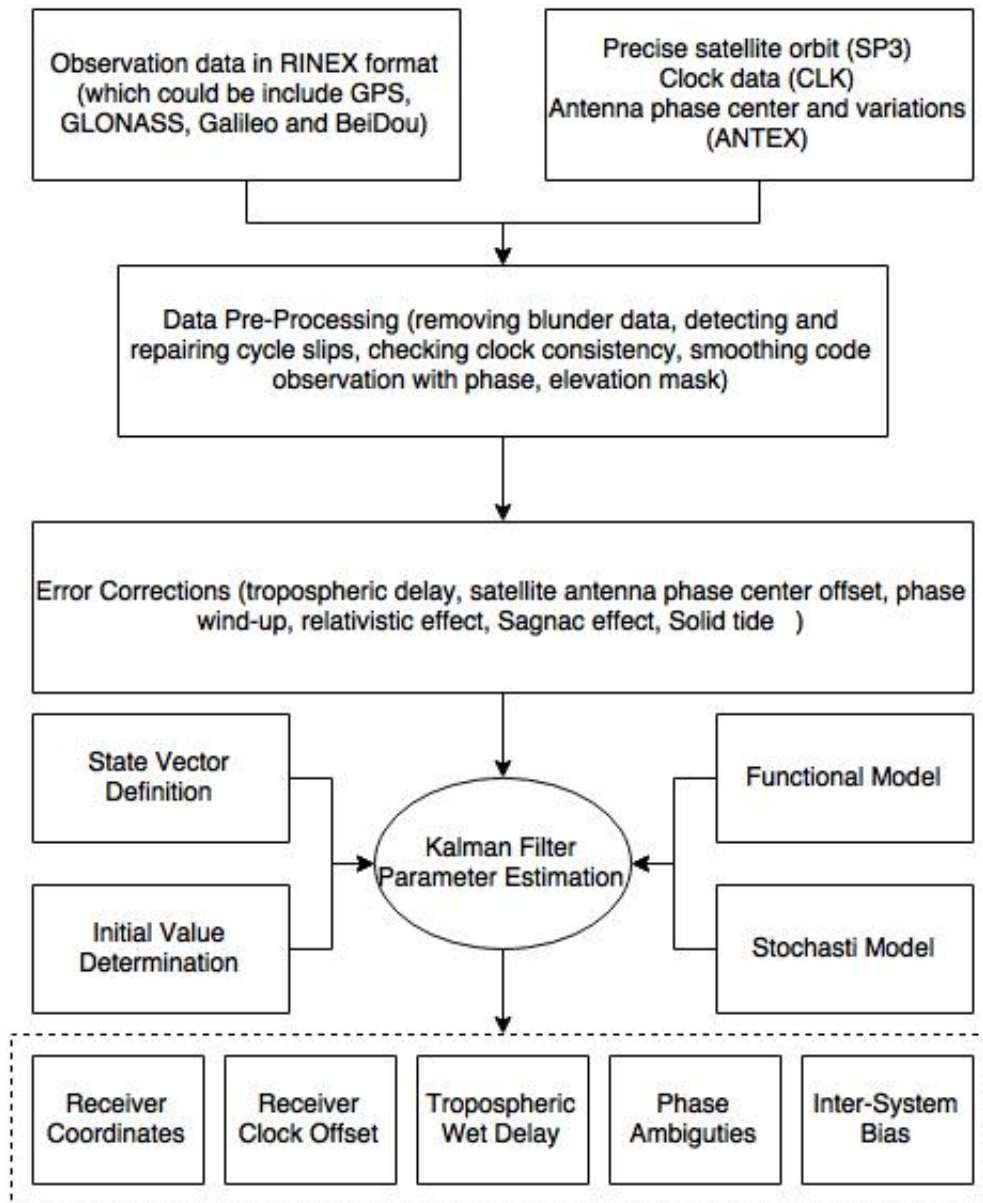


Figure 5.8: The flowchart of PPPH processing.

6. TESTS AND RESULTS

This chapter presents the results and analyses of experimental tests conducted to evaluate both the performances of the PPPH and multi-GNSS PPP model. Firstly, the data collection procedure used in this study is described, and then the results are presented and analysed in detail.

6.1. Data Description

Six IGS stations have been selected to be utilized in this study. They are HOFN, NNOR, OUS2, REUN, UNB3, and WTZZ whose locations are indicated in Figure 6.1. The main characteristic of these stations is that they are an MGEX stations equipped with the multi-GNSS receivers to track GLONASS, Galileo and BeiDou satellites in addition to GPS.

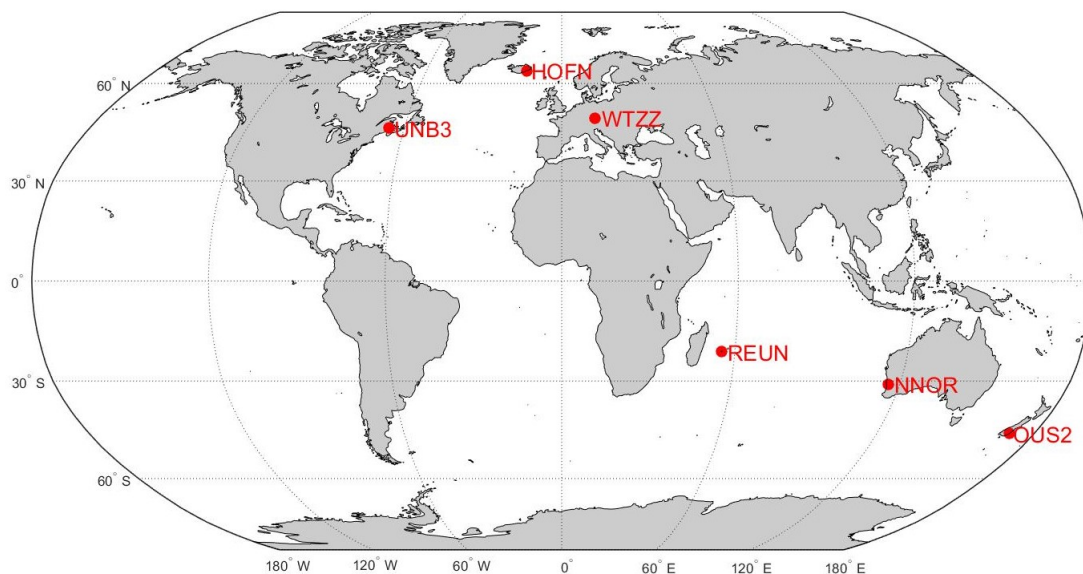


Figure 6.1: Distribution of IGS reference stations used in this study.

IGS broadcasts 30 seconds observation data of its reference stations regularly. Observation datasets collected from selected six stations during the days between 10-14 May and 2-6 June 2015 were obtained via IGS services. Instead of 10 consecutive days, it was preferred to use two 5-days periods to analyze the influence of ionospheric variations on the PPP models and algorithms. When deciding the time spans, K_p indices have been taken into account. K_p index refers to an integer number between 0 and 9, which represents the level of ionospheric activity [75]. Typically, the level of ionospheric

activity is very quiet if K_p is lower than 1, it is moderately active if K_p is between 1 and 4.5, and it is highly active if K_p is greater than 4.5 [56]. Using 3 hours K_p indices provided by GFZ (<http://www.gfz-potsdam.de/en/kp-index/>), two 5-days periods have been determined among the quietest and most distributed days of 2015. Note that the availability of MGEX data and products is an important restriction for this selection.

Table 6.1 shows the daily average of 3 hours K_p indices for selected 10 days. As it can be easily seen in the table, the first 5-days period is moderately active in terms of ionospheric activity, while the second 5-days period is very quiet. K_p indices also indicates that there is a high level of ionospheric activity on May 13, 2015.

Table 6.1: Daily average K_p indices of the days between 10-14 May and 2-6 June 2015.

Days (2015)	May 10	May 11	May 12	May 13	May 14
K_p index	2.2	2.9	3.0	4.9	2.0
Days (2015)	June 2	June 3	June 4	June 5	June 6
K_p index	0.8	0	0	1.2	1.6

Finally, IGS final products were utilized to eliminate the orbit and clock errors in GPS-only PPP, while MGEX products produced by GFZ were utilized for multi-GNSS PPP processing,. The specifications of these products were previously described in Section 3.1.

6.2. Validating the Positioning Performance of PPPH

The positioning performance of PPPH is required to be validated by comparing a reference or the other PPP estimates. For this purposes, two comparisons were performed within the study. The first test is performed by comparing the PPP estimates of the software with the reference coordinates as regards the convergence time, accuracy and precision. The second is to compare the results of PPPH with the ones which are acquired from the other PPP software or services, statistically.

To assess the positioning performance, 24 hours datasets explained before were processed in PPPH in static mode including the only GPS satellites. As mentioned above, the quality assessment of the estimates was made in three aspects, which are accuracy, precision and convergence time. To determine the accuracy of PPP estimates, IGS weekly solutions, which include very precise station coordinates, were used as the *ground truth*. The positioning error, that is the difference between the PPP solution

and the ground truth, was computed in the topocentric system. Additionally, convergence time was determined with the definition of the time taken until to achieve a sub-decimetre 3D positioning accuracy and for a period longer than 5 minutes. Concerning the precision, root mean square (RMS) error was computed as including the whole epochs after the convergence time.

Table 6.2 shows the positioning errors acquired from the PPPH estimates at the end of 24 hours processing. From the table, we can see that the horizontal and vertical positioning errors have reached a maximum value of 1.7 cm and 3.5 cm, respectively. Additionally, 80% of the horizontal positioning errors and 55% of the vertical positioning errors are less than 1 cm. It means that PPPH could provide centimetre-level positioning accuracy. Furthermore, there is no significant difference between the positioning and RMS errors due to the rigorous error modelling in PPP, which shows that the positioning estimates are very consistent after the convergence time. Also, Figure 6.2 illustrates the ten days convergence times for each station. It can be seen that the convergence takes maximum 70 and minimum 8 minutes, respectively. It should be mentioned that the number and geometry of visible satellites can vary the convergence time significantly. Considering at least 1 hour is required to achieve 5 cm or better horizontal positioning accuracy in standard PPP processing, the convergence time obtained from PPPH processing is very comparable with the general acceptance [76]. Finally, it is observed that there is no considerable impact of ionospheric variations on the PPP results when the positioning errors are taken into consideration.

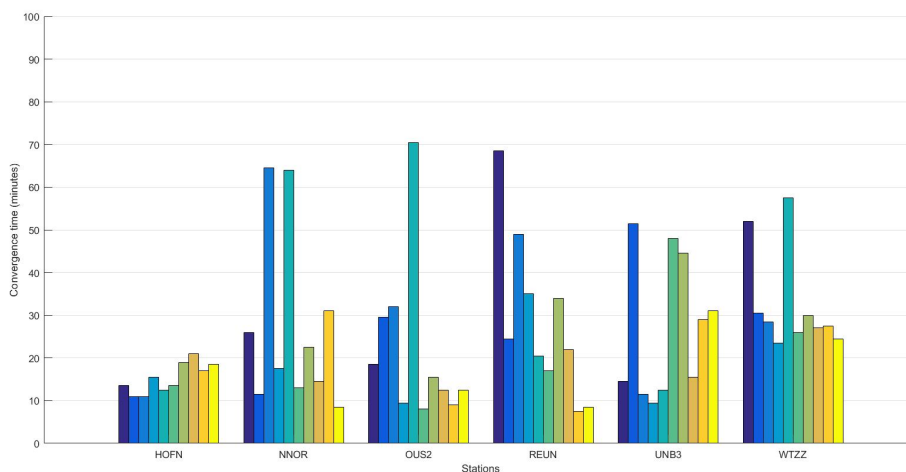


Figure 6.2: Ten days convergence times of each station obtained from PPPH estimates.

The second validation can be made by comparing the results of PPPH with the other software's result. For this purpose, online PPP processing services can be employed to validate the quality of PPPH estimates. Such services are the PPP software packages generated and developed by leading universities and research institutes, and they are

Table 6.2: Ten days positioning errors of six stations obtained from PPPH estimates at the end of 24 hours processing

Station	Day	Positioning errors (cm)			RMS errors(cm)			Day	Positioning errors (cm)			RMS errors(cm)		
		N	E	U	N	E	U		N	E	U	N	E	U
HOFN	1	0.4	0.7	-0.6	0.8	1.2	0.7	6	-0.3	0.7	-0.7	0.8	0.9	1.1
	2	0.2	0.5	-0.8	0.5	1.1	1.5	7	-0.2	0.9	-0.6	0.3	1.1	0.7
	3	0.1	1.4	-0.2	0.4	1.2	1.2	8	-0.1	0.9	-0.8	0.5	0.9	0.7
	4	0.4	0.2	-0.3	0.5	1.8	2.0	9	-0.1	1.0	-0.6	0.3	1.2	0.7
	5	0.3	0.7	-0.1	0.5	1.1	1.4	10	0.1	0.6	0.6	0.3	0.6	0.8
NNOR	1	-0.4	0.9	-0.2	0.4	1.7	1.5	6	-0.1	0.4	-0.9	0.3	1.2	1.6
	2	-0.4	-0.1	-1.0	0.6	2.5	2.9	7	-0.2	0.3	-1.1	0.6	1.3	2.3
	3	-0.4	-0.2	-0.4	0.7	1.7	1.2	8	-0.3	1.0	-1.4	0.4	1.8	2.2
	4	-0.4	-1.2	-1.6	0.6	2.6	2.4	9	-0.6	0.9	-2.0	0.8	3.3	3.2
	5	-0.6	-0.3	-1.7	0.8	1.0	2.2	10	0.1	1.1	-0.8	0.5	2.7	2.1
OUS2	1	0.8	1.1	0.1	1.2	1.2	1.2	6	0.1	0.7	0.6	0.4	0.9	1.8
	2	1.6	0.1	1.2	1.9	0.8	1.7	7	0.6	0.2	-0.5	0.4	0.7	0.7
	3	0.9	0.8	-0.1	1.2	1.2	1.3	8	0.1	0.9	-1.1	0.3	1.3	1.1
	4	1.2	1.2	-0.3	1.5	2.1	1.7	9	-0.3	0.6	-1.5	0.5	0.7	1.3
	5	0.5	0.6	-0.6	0.6	1.0	1.8	10	-0.4	0.7	-1.4	0.6	1.2	1.3
REUN	1	-0.3	0.1	0.7	0.2	0.7	0.9	6	-0.1	-1.4	-3.5	0.2	2.3	4.5
	2	0.1	-1.0	-1.4	0.7	1.5	2.0	7	-0.4	-1.3	-1.3	0.3	1.8	1.4
	3	0.1	0.8	-0.5	0.4	0.9	1.1	8	-0.3	-0.4	0.5	0.4	0.8	1.1
	4	0.6	0.8	-0.3	0.7	0.9	0.9	9	-0.1	-1.1	-0.3	0.4	1.5	1.3
	5	-0.7	0.2	-0.3	1.3	0.8	2.8	10	-0.3	-1.0	-0.6	0.3	1.1	0.9
UNB3	1	0.8	-1.4	-2.1	1.2	2.2	1.9	6	-0.4	-0.1	-1.7	0.9	0.8	2.5
	2	1.0	-1.4	-2.2	1.5	2.2	2.9	7	-0.6	0.3	-1.6	1.1	0.5	2.7
	3	0.6	-1.3	-1.3	1.1	2.2	1.7	8	-0.7	-0.3	-2.6	1.6	0.7	2.3
	4	1.7	0.5	-1.1	2.5	2.5	2.7	9	-1.0	0.4	-1.9	1.4	0.6	2.5
	5	0.3	-1.3	-2.0	0.6	2.1	1.6	10	-0.8	0.5	-1.5	1.1	0.6	2.0
WTZZ	1	0.3	1.2	-1.3	1.2	1.3	1.0	6	0.3	1.0	-0.2	0.3	1.4	1.1
	2	-0.3	0.4	0.9	0.5	0.9	1.6	7	-0.3	0.3	-0.1	0.7	0.5	0.9
	3	-0.2	0.5	1.4	0.1	0.7	2.8	8	-0.3	0.5	-1.2	0.5	0.7	1.1
	4	1.0	-0.3	0.6	1.2	2.2	1.6	9	-0.4	0.2	-0.4	0.5	0.6	0.7
	5	0.2	0.1	1.7	0.3	1.1	3.4	10	0.1	0.3	-0.9	0.4	0.7	0.8

freely open to users 24-h per day. Currently, there are six online PPP processing services free of charge, namely Online Positioning User Service (OPUS), Automatic Precise Positioning Service (APPS), Scripps Coordinate Update Tool (SCOUT), Canadian Spatial Reference System Precise Point Positioning Service (CSRS-PPP), GPS Analysis and Positioning Software (GAPS) and Geoscience Australia Online GPS Processing Service (AUSPOS). Table 6.3 gives the developers and URLs of these services.

Table 6.3: Agencies and URLs of online PPP processing services.

Service	Agency	URL
OPUS	National Geodetic Survey (NGS) of the United States	https://www.ngs.noaa.gov/OPUS/
APPS	Jet Propulsion Laboratory (JPL)	http://apps.gdgps.net/
SCOUT	Scripps Orbit and Permanent Array Center (SOPAC)	http://sopac.ucsd.edu/processing.shtml#
CSRS-PPP	National Resources Canada (NRCan)	https://webapp.geod.nrcan.gc.ca/geod/tools-ouils/ppp.php?locale=en
GAPS	University of New Brunswick (UNB)	http://gaps.gge.unb.ca/
AUSPOS	Geoscience Australia	http://www.ga.gov.au/bin/gps.pl

Online PPP services offer an alternative to GNSS users which need to highly precise positioning. The quality of results obtained from online PPP services is mainly dependent on the data span [77, 78, 79]. In order to obtain PPP solutions, it is only required to upload the observation data via the internet. A short time later, the results including precise coordinates and other estimates are sent by e-mail. In general, online PPP processing services produce coordinates in ITRF, however, some services have options to obtain coordinates in their national geodetic reference frame.

Online PPP services have taken considerable attention within the GNSS community over the past decade. These services have been widely used in GNSS applications, such as vertical and horizontal displacement monitoring, marine applications, etc [80, 81, 82]. Additionally, several studies have shown that online PPP services enables centimetre-level positioning accuracy for a 24 hours datasets in the static mode [78, 79, 83]. Among the options presented above, two of the most used online PPP services, CSRS-PPP and GAPS, were chosen for the comparison with PPPH. Although the online PPP services follow standart PPP processing strategy in general, there are certain differences between them. Table 6.4 presents the main processing strategies of these

online services in addition to PPPH.

Table 6.4: Main processing strategies of PPPH, GAPS, CSRS-PPP

	PPPH	GAPS	CSRS-PPP
Constellation	GPS, GLONASS, Galileo, BeiDou	GPS, Galileo, BeiDou	GPS, GLONASS
Satellite orbit and clock	IGS, MGEX	IGS or NRCan, MGEX	IGS or NRCan
Satellite and receiver phase center offset	IGS ANTEX		
Observable	Undifferenced, ionosphere-free linear combination of dual frequency code and phase observations		
Weighting scheme	Elevation angle-dependent		
Processing mode	Static	Static/Kinematic	Static/Kinematic
Troposphere			
Dry model	Saastamoinen (GPT2)	VMF1 (ECMWF) default	Davis (GPT)
Wet model	Estimated	Estimated	Hopfield (GPT) initial and estimated
Mapping function	GMF	VMF	GMF
Adjustment method	Adaptive robust Kalman filter	Sequential least squares with weighted constraints	Batch least squares
Estimation	Station coordinates, receiver clock offset, inter-system bias, tropospheric wet delay, ambiguities		

GPT: Global Pressure and Temperature data, GPT2: Global Pressure and Temperature 2 data, ECMWF: European Center for Medium-Range Weather Forecast data, GMF: Global Mapping Function, VMF: Vienna Mapping Function

In order to compare PPPH with online PPP services, same datasets were processed in CSRS-PPP and GAPS, individually. It should be noted that CSRS-PPP does not have an option to determine which navigation systems will be included in PPP processing. So, CSRS-PPP necessarily perform PPP processing including GLONASS satellites in addition to GPS satellites. However, GAPS is not compatible with GLONASS and PPP solutions are performed with only GPS satellites. The results were statistically evaluated in a similar way to previous analysis. Table 6.5 and Table 6.6 present the 5-days averaged positioning errors, RMS errors and convergence times obtained from

PPPH, GAPS, and CSRS-PPP for the days between 10-14 May and 2-6 June 2015, respectively.

When the results are analysed, it is observed that the average positioning errors obtained from three services (or software) do not exceed 2.6 cm. Additionally, the 10-days average 3D positioning errors of PPPH, GAPS, and CSRS-PPP are 1.6, 2.0 and 1.3 cm, respectively, which means that centimetre-level positioning accuracy has been achieved by. As a consequence, it is clear that PPPH is quite comparable with online PPP services in terms of accuracy. Similarly, the RMS errors of all three services (or software) are at the centimetre-level. Nevertheless, CSRS-PPP has relatively fewer RMS errors in the whole directions. Probably an important factor for this result is that CSRS-PPP employs GLONASS satellites in PPP processing together with GPS.

If the convergence results are analysed, we can see that the maximum convergence time takes 39, 37, and 21 minutes in PPPH, GASP, and CSRS-PPP processing, respectively. Also, the average convergence times for all stations are 28.8, 26.4, and 16.4 minutes for PPPH, CSRS-PPP, and GAPS solutions, respectively. It should be noted that CSRS-PPP solution converges to sub-decimetre positioning accuracy shorter than both PPPH and GAPS probably because of including GLONASS satellites as described before. Again, it can be said that three solutions are comparable with each other and with the standard PPP acceptance as mentioned above.

The last matter about the comparison is to evaluate the impact of ionospheric variations on PPP processing models and algorithms. If the results of the first 5 days, which is experienced moderately high ionospheric activity, and the second 5 days, which is a very quiet period in terms of ionospheric variations, are examined, it is seen that there are not any significant difference. Therefore, it can be concluded that the PPP results are rarely affected from the ionospheric variations.

In conclusion, the positioning performance of PPPH was validated by online PPP services with regards to accuracy, precision, and convergence time. It can be said that centimetre-level accuracy can be achieved by PPPH, and it is compatible with the online PPP processing services.

Table 6.5: Five days averaged PPP results for PPPH, GAPS and CSRS-PPP (May 10-14, 2015).

	PPPH				GAPS				CSRS-PPP				PPPH			GAPS			CSRS-PPP			PPPH	GAPS	CSRS-PPP
Stations	Positioning errors (cm)												RMS errors (cm)									Convergence time (minutes)		
	N	E	U	3D	N	E	U	3D	N	E	U	3D	N	E	U	N	E	U	N	E	U			
HOFN	0.3	0.7	0.4	0.9	0.6	1.0	1.6	2.0	0.2	0.5	0.6	0.8	0.5	1.3	1.4	1.1	2.4	3.2	0.4	0.5	0.6	13	13	10
NNOR	0.4	0.5	1.0	1.2	0.8	0.3	1.0	1.3	0.2	0.4	1.0	1.1	0.6	1.9	2.0	0.9	0.6	1.1	0.3	0.5	1.0	27	22	15
OUS2	1.0	0.8	0.5	1.3	0.9	0.4	2.4	2.6	0.6	0.2	0.8	1.1	1.3	1.3	1.5	0.9	1.0	2.6	0.7	0.8	1.1	24	19	13
REUN	0.4	0.6	0.6	0.9	0.9	0.5	0.7	1.2	0.5	0.3	0.7	0.9	0.6	0.9	1.5	1.0	0.8	1.5	0.6	0.7	1.1	39	37	15
UNB3	0.9	1.2	1.7	2.2	1.2	0.4	1.2	1.7	0.3	0.5	0.8	1.0	1.3	2.2	2.2	1.5	0.9	1.2	0.7	0.9	1.4	20	18	10
WTZZ	0.4	0.5	1.2	1.4	0.8	0.4	1.9	2.1	0.3	0.3	1.8	1.9	0.7	1.2	2.1	0.7	0.6	2.2	0.3	0.7	1.8	38	36	21

77

Table 6.6: Five days averaged PPP results for PPPH, GAPS and CSRS-PPP (June 2-6, 2015).

	PPPH				GAPS				CSRS-PPP				PPPH			GAPS			CSRS-PPP			PPPH	GAPS	CSRS-PPP
Stations	Positioning errors (cm)												RMS errors (cm)									Convergence time (minutes)		
	N	E	U	3D	N	E	U	3D	N	E	U	3D	N	E	U	N	E	U	N	E	U			
HOFN	0.2	0.8	0.7	1.0	0.4	0.4	1.9	2.0	0.3	0.3	0.4	0.6	0.4	0.9	0.8	0.5	0.6	1.8	0.4	0.5	0.7	18	31	10
NNOR	0.3	0.7	1.2	1.4	0.9	0.2	0.8	1.3	0.2	0.3	0.9	1.0	0.5	2.0	2.2	0.9	1.1	1.2	0.3	0.7	1.0	18	14	15
OUS2	0.3	0.6	1.0	1.2	0.9	0.5	1.8	2.1	0.7	0.4	0.9	1.2	0.4	1.0	1.2	0.9	1.2	2.6	0.8	0.8	1.6	12	19	10
REUN	0.2	1.0	1.2	1.6	0.8	0.7	0.9	1.3	0.5	0.4	0.8	1.1	0.3	1.5	1.8	1.1	4.1	4.7	0.6	0.8	1.2	18	16	15
UNB3	0.7	0.3	1.8	2.0	0.5	0.3	1.0	1.1	0.3	0.1	1.1	1.2	1.2	0.6	2.4	0.6	1.0	1.4	0.6	0.5	1.3	34	20	13
WTZZ	0.3	0.5	0.6	0.8	0.6	0.2	1.3	1.5	0.3	0.4	1.3	1.4	0.5	0.8	0.9	0.6	0.7	1.7	0.5	0.6	1.6	27	19	17

6.3. Integrating Multi-GNSS to Improve the PPP Performance

The geometry and number of visible satellites, observation session length and quality of precise products are important factors to determine the quality of PPP estimates. Since the combined multi-GNSS provides additional satellite resources, it can improve the PPP performance significantly. The contribution of multi-GNSS to PPP performance is evaluated in this section.

Three different PPP scenarios, which are GPS-only, GPS/GLONASS and multi-GNSS, have been introduced for the assessment of multi-GNSS contributions on the PPP performance. Because the PPP performance closely depends on the geometry of visible satellites as previously stated, first of all, the availability of visible satellites was analysed. For this purpose, 24 hours observation data collected from six MGEX stations during 2-6 June 2015 were processed under three scenarios. The precise orbit and clock products provided by GFZ were utilized for the whole systems for the sake of consistency. Figure 6.3 presents the average number of visible satellites (per epoch) of different combined system for each station.

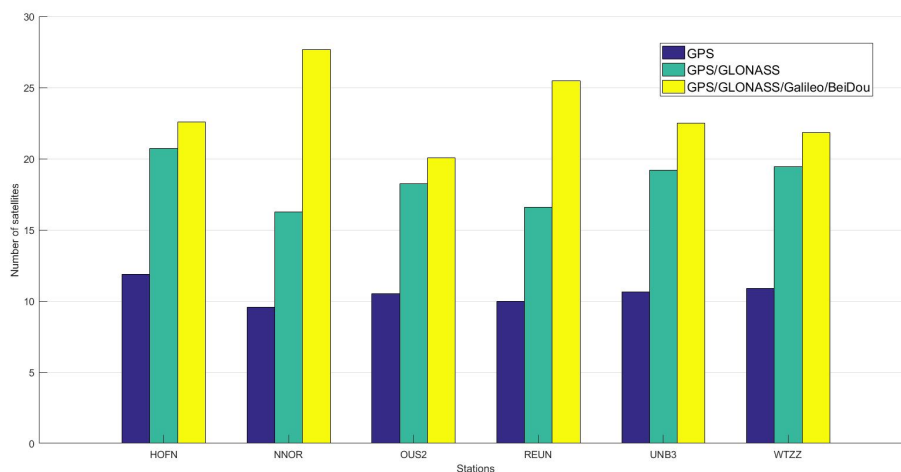
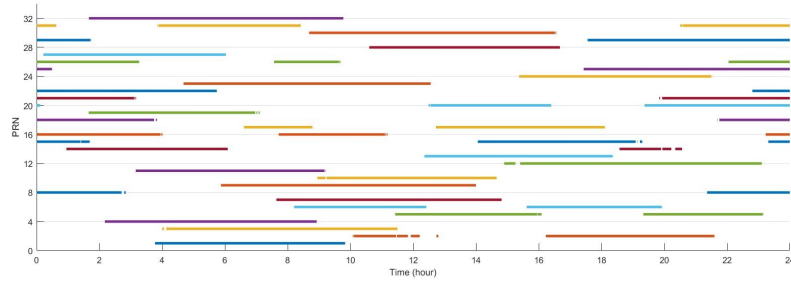
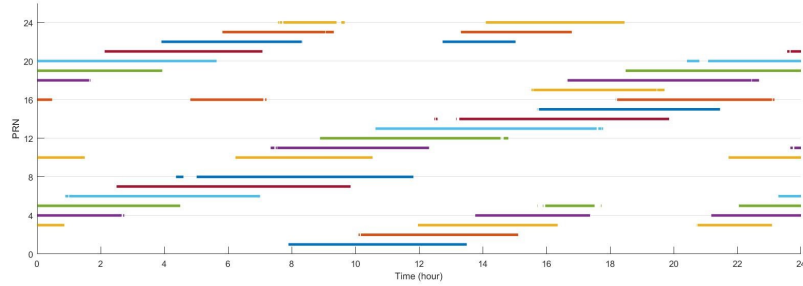


Figure 6.3: Average numbers of visible satellites of different system combinations during the days between 2-6 June 2015.

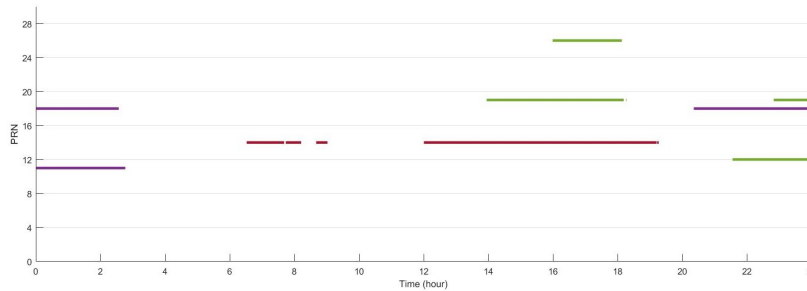
As it can be seen from Figure 6.3, the satellite availability depends on the geographical location of the station. If GLONASS satellites are employed together with GPS, the number of visible satellites are increased at the rate of 74% in average. This rate ranges between 66% and 80% depending on the station's location. Similarly, the addition of Galileo and BDS satellites raises the number of visible satellites at a rate of approximately 28% relative to the combined GPS/GLONASS. However, the increase considerably varies from one station to other. For example, the rate of increase is 9% at



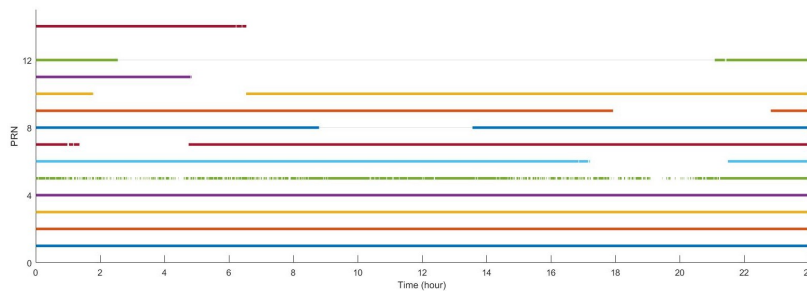
(a) Visible satellite distribution for GPS.



(b) Visible satellite distribution for GLONASS.



(c) Visible satellite distribution for Galileo.



(d) Visible satellite distribution for BeiDou.

Figure 6.4: Visible satellite distribution for GNSS at station NNOR on 2 June 2015.

station HOFN, while the rate is 70% at station NNOR. The reason is that the number of BDS observations increase significantly in Asia-Pacific due to the BDS Geostationary Earth Orbit (GEO) satellites in the region. Figure 6.4 shows the visible satellite distribution for GPS, GLONASS, Galileo and BeiDou at station NNOR on the date of 2 June 2015, respectively. From Figure 6.4, we can see that the increase of satellite number caused by Galileo is not remarkable and the most of the increase is actually

caused by GLONASS and BDS. While the number of visible GLONASS satellites is approximately the same for all the stations, the number of visible BDS satellites is very dependent on geographical location.

The satellite geometry is another important factor influencing the quality of position estimates. The PDOP factor is typically used for measuring the instantaneous geometry [31]. Figure 6.5 shows the average PDOP factor of different system combinations for each station. Note that the average PDOP factor was calculated by taking the average of the PDOP factors of the whole epochs before the convergence. The combined GPS/GLONASS reduces PDOP factor by 23%, and the reduction ratio ranges from 13% to 30%. Therefore, the GPS/GLONASS combination has great potential to improve PPP performance at all stations. However, it is not possible to say the same thing for the addition of Galileo and BeiDou satellites. The average rate of reduction is approximately 14%, but if only the stations located in the Asia-Pacific region are considered, the ratio rises to 27%. Additionally, there is not any improvement in PDOP factors for stations HOFN and WTZZ. Still, the PDOP factors of stations located in the Asia-Pacific region shows considerable improvement when multi-GNSS combination is employed.

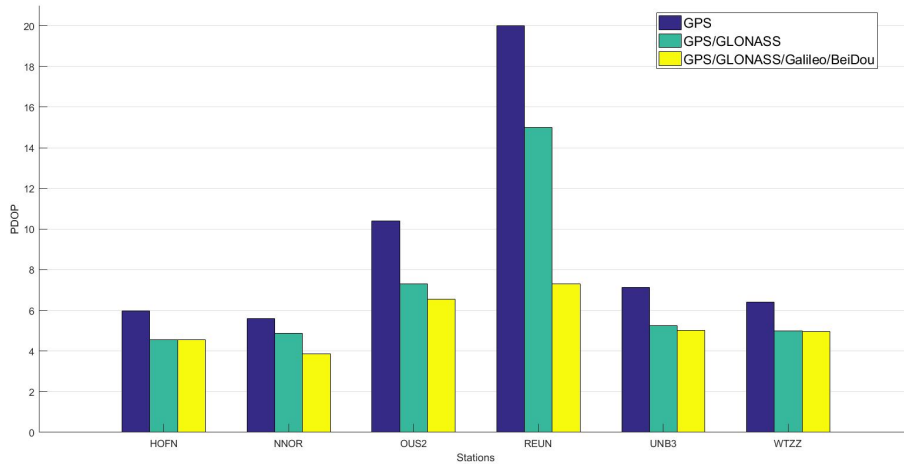


Figure 6.5: Average PDOP factors for different system combinations.

The results were also analysed with regards to accuracy and convergence time. Figure 6.6 indicates the average 3D positioning errors calculated for the different system combinations in each station, respectively. As the figure implies, the integration of two or more constellations efficiently improves the 3D positioning error according to GPS-only PPP solution. If the results of GPS/GLONASS PPP and multi-GNSS PPP are compared, it is seen that there is a slight improvement in positioning accuracies for all stations except for station NNOR. The exception can be caused by the poor quality of the BDS products. Also, it should be noted that the differences do not exceed a few

millimetres. Similarly, 6.7 illustrates the average convergence times for the different system combinations. The figure demonstrates that the GPS/GLONASS and multi-GNSS PPP significantly reduce the convergence time. In conclusion, the combined multi-GNSS has a considerable potential to improve the performance of PPP.

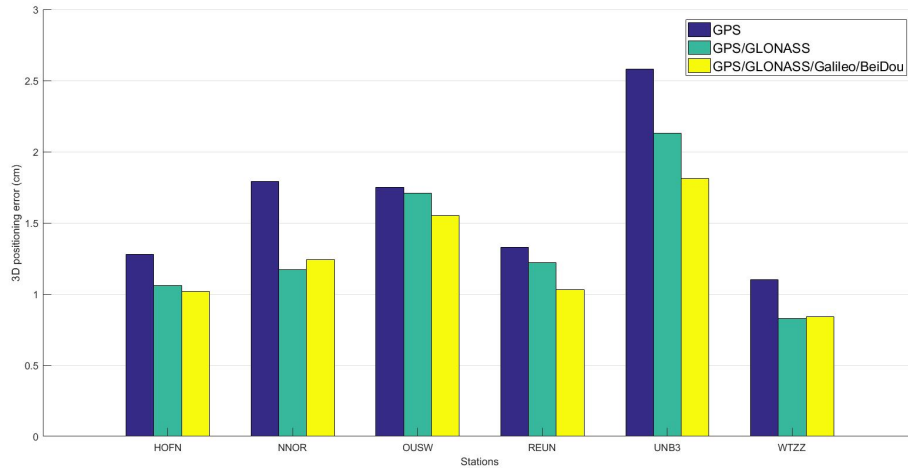


Figure 6.6: Five days averaged 3D positioning errors for different system combinations.

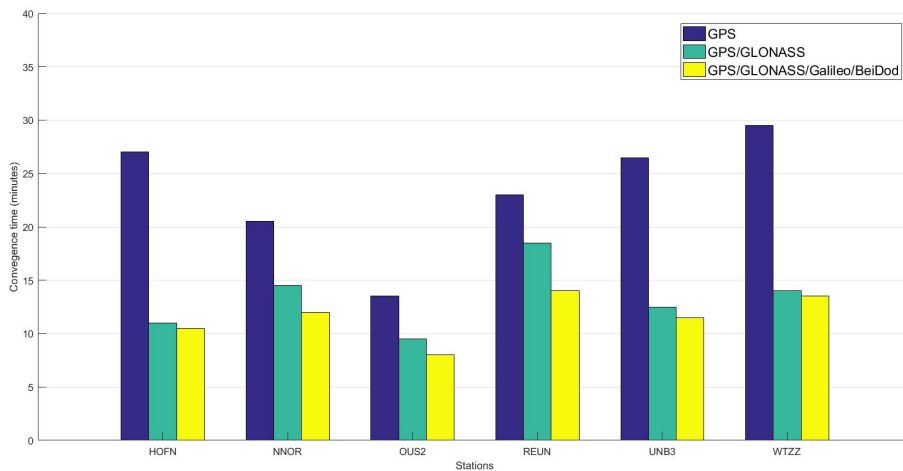


Figure 6.7: Five days averaged convergence times for different system combinations.

To assess the multi-GNSS PPP performance in more details, the same dataset has been processed in static mode under the three scenarios described above, but, this time the Kalman filter estimator is restarted every 3 hours, which means that each station has 8 periods in one day, and 240 periods in five days. In other words 720 processes were performed individually. Table 6.7 demonstrates the average positioning errors of PPP solutions for different system combinations and their improvements with respect to GPS-only PPP solution. From Table 6.7, it can be concluded that the positioning accuracy of combined system PPP is better than GPS-only PPP. The improvement

ratio of combined GPS/GLONASS PPP in the positioning accuracy varies between 7.5% and 27.4%. Considering the improvements in the whole stations, the combined GPS/GLONASS PPP enhances the 3D positioning error at a rate of %16.2 in average. Similarly, the combined four systems has an improvements between 8.5% and 45.3% with respect to GPS-only PPP solution, while the average ratio of improvement is 21.6%. On the other hand, the stations in Asia-Pacific, namely NNOR, OUS2, and REUN experienced significant improvements for the integration of multi-GNSS PPP. This is not surprising due to the considerable increase of both visible satellite number and geometry as described before.

Table 6.7: Positioning error comparison of different system combinations.

Station	System combination	Positioning error (cm)				Improvement w.r.t GPS (%)			
		N	E	U	3D	N	E	U	3D
HOFN	GPS	0.9	1.6	3.1	3.6	-	-	-	-
	GPS/GLONASS	0.9	1.4	2.7	3.2	0	12.5	12.9	12.0
	GPS/GLONASS/Galileo/BDS	0.9	1.4	2.6	3.1	0	12.5	16.1	13.5
NNOR	GPS	0.9	2.4	2.9	3.9	-	-	-	-
	GPS/GLONASS	0.8	1.4	2.3	2.8	11.1	41.7	20.7	27.4
	GPS/GLONASS/Galileo/BDS	0.7	1.2	1.6	2.1	22.2	50.0	44.8	45.3
OUS2	GPS	1.4	2.7	2.8	4.1	-	-	-	-
	GPS/GLONASS	1.3	2.1	2.2	3.3	7.1	22.2	21.4	20.0
	GPS/GLONASS/Galileo/BDS	1.3	2.1	1.9	3.1	7.1	22.2	32.1	24.6
REUN	GPS	0.9	2.0	2.6	3.4	-	-	-	-
	GPS/GLONASS	0.8	1.9	2.0	2.9	11.1	5.0	23.1	15.6
	GPS/GLONASS/Galileo/BDS	0.7	1.8	1.9	2.7	22.2	10.0	26.9	20.4
UNB3	GPS	1.4	1.9	3.2	4.0	-	-	-	-
	GPS/GLONASS	1.4	1.8	2.5	3.4	0	5.3	21.9	14.9
	GPS/GLONASS/Galileo/BDS	1.3	1.7	2.5	3.3	7.1	10.5	21.9	17.2
WTZZ	GPS	1.2	1.6	3.7	4.2	-	-	-	-
	GPS/GLONASS	1.1	1.3	3.5	3.9	8.3	18.8	5.4	7.5
	GPS/GLONASS/Galileo/BDS	1.0	1.5	3.4	3.8	16.7	6.3	8.1	8.5

Table 6.8 shows the average convergence times for PPP solutions of different system combinations in addition to its reduction according to GPS-only PPP solution. From the table, we can see that the multi-GNSS PPP has the best performance in terms of the convergence. The combined GPS/GLONASS PPP lessens the convergence time at a rate of 28.1% in average. Similarly, the multi-GNSS PPP has an average of 33.2% reduction in the convergence time with respect to GPS-only PPP. As it would

be expected, the most significant reduction for multi-GNSS PPP is observed at the stations located in Asia-Pacific region. On the other hand, multi-GNSS PPP has a slight influence on the convergence time at stations HOFN, UNB3, and WTZZ because of the limited increase in the number of the visible satellite.

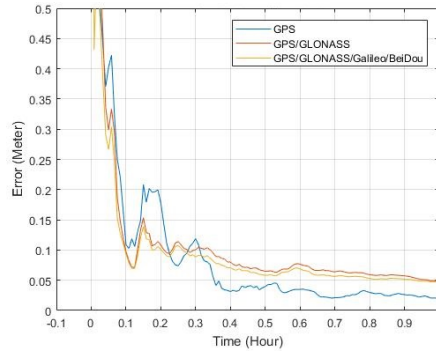
Table 6.8: Convergence time comparison of different system combinations.

		GPS	GPS/ GLONASS	GPS/ GLONASS/ Galileo/ BDS
HOFN	Convergence time (min)	26.4	20.8	20.3
	Reduction w.r.t GPS (%)	-	21.2	23.1
NNOR	Convergence time (min)	28.0	17.5	16.0
	Reduction w.r.t GPS (%)	-	37.5	44.6
OUS2	Convergence time (min)	23.9	17.7	16.8
	Reduction w.r.t GPS (%)	-	25.9	29.7
REUN	Convergence time (min)	31.5	23.5	20.0
	Reduction w.r.t GPS (%)	-	25.4	36.5
UNB3	Convergence time (min)	29.4	20.7	19.8
	Reduction w.r.t GPS (%)	-	29.6	32.7
WTZZ	Convergence time (min)	31.4	22.4	21.1
	Reduction w.r.t GPS (%)	-	28.7	32.8

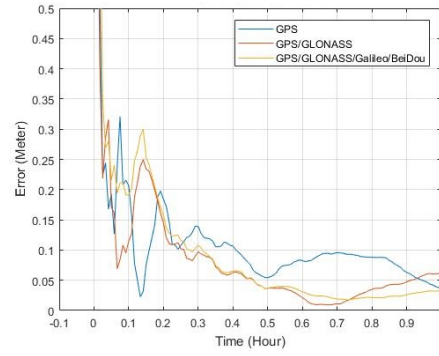
Finally, Figure 6.8 presents the 3D positioning errors for 8 different periods during the day 2 June 2015 at station NNOR. In order to be apparently visible, only one hour of each 3 hours period is illustrated in the figure. From Figure 6.8, it can be seen that the combined PPP considerably shortened the convergence time excepts for the third period (see Figure 6.8c). The multi-GNSS PPP has a lightly better convergence performance at station NNOR during the date of 2 June 2015 relative to the combined GPS/GLONASS PPP.

6.4. Initialization of Kalman Filter using Least Squares Adjustment

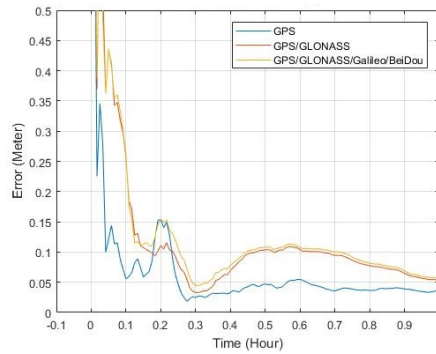
In Subsection 4.4.2, it was stated that insufficient or wrong initial knowledge about both estimated parameters and process dynamics degrade the quality of PPP estimates. Unfortunately, it is difficult to obtain a priori parameters reflecting system dynamics appropriately because measurement quality and process dynamics vary depending on



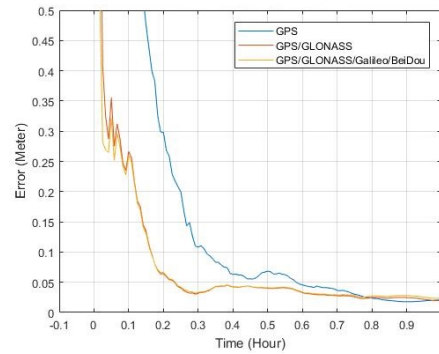
(a) Between 00:00 and 01:00.



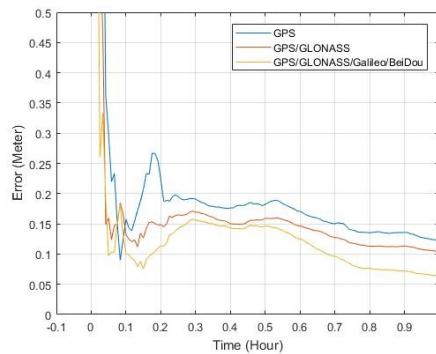
(b) Between 03:00 and 04:00.



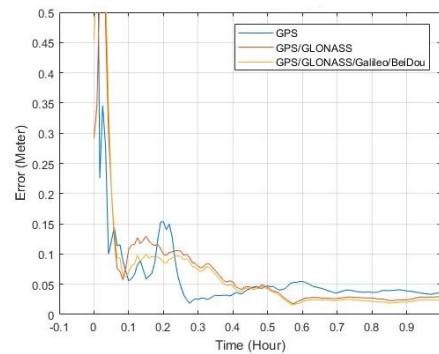
(c) Between 06:00 and 07:00.



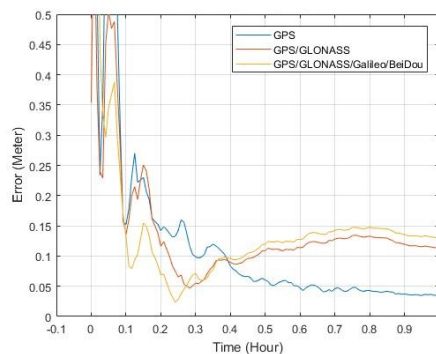
(d) Between 09:00 and 10:00.



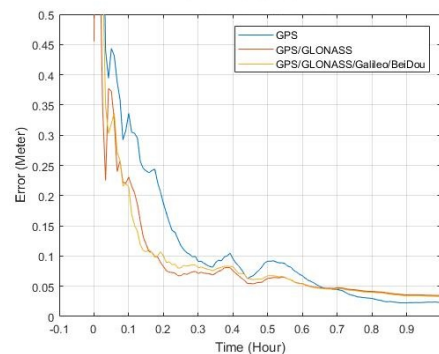
(e) Between 12:00 and 13:00.



(f) Between 15:00 and 16:00.



(g) Between 18:00 and 19:00.



(h) Between 21:00 and 22:00.

Figure 6.8: 3D positioning errors for different system combinations during the day 2 June 2015 at station NNOR.

many factors, such as application type, receiver type, geographical location of the station, user environment, etc. To overcome this problem, an innovative method is introduced to acquire prior knowledge of system dynamics in this study. This method involves the computation of initial parameters and their covariance using least squares adjustment.

To assess the effectiveness of the method, an experimental test was conducted. 24 hours observation data collected from 6 IGS stations on 2 June 2016 were processed by restarting every 3 hours. It should be mentioned that the PPP solutions were performed by including GPS, GLONASS, Galileo, and BDS satellites, and the precise products provided by GFZ were used. For the analysis, each process was initialized with a priori parameters obtained by least squares and also with the standard parameters, individually. As a result, 96 processes were performed to examine the contribution of this approach. The spectral densities of estimated parameters given in Subsection 4.2.2 were used as a default for both processes. Additionally, initial uncertainties of station coordinates, receiver clock error, tropospheric delay, inter-system biases and ambiguities were assumed to be 100 m, 10^5 m, 0.5 m, 100 m and 200 m, respectively. Table 6.9 shows the average values for positioning errors and convergence times acquired from PPP processes initialized with both standard parameters and least squares adjustment. From the table, we can see that new method slightly enhance the positioning performance of PPP, approximately 4.5%. However, it has a considerable improvement on convergence time. Compared to the standard parameters, initialization of the Kalman filter with parameters obtained from least squares reduces convergence time at a rate of 15.8% in average. As a consequence, it can be concluded that the new approach is successful to determine suitable initial parameters for the implementation of the Kalman filter in PPP processing.

Table 6.9: Average values of positioning errors and convergence times acquired from PPP processes initialized with standard parameters and least squares adjustment

Initialization method	Number of data sets	Positioning error (cm)				Convergence time (min)
		N	E	U	3D	
Standard parameters	48	1.1	2.3	3.6	4.4	38
Least squares	48	1.1	2.1	3.5	4.2	32
Improvement (%)		0	8.7	2.8	4.5	15.8

7. CONCLUSIONS

The principal goal of this thesis is the examination of the multi-GNSS PPP performance including the observations from multi-constellations, which are GLONASS, Galileo, BDS as well as GPS. The thesis includes the theoretical background for multi-GNSS PPP approach containing functional and stochastic models as well as the traditional PPP approach. Furthermore, some improvements aiming to increase the efficiency of the Kalman filter estimation on PPP were introduced. As a part of this research, a PPP software package, named PPPH, was developed to evaluate the multi-GNSS PPP performance independently. The performance of PPPH was evaluated by comparing with other PPP software or services. Finally, several tests were performed to examine the multi-GNSS PPP performance as regards the convergence and positioning accuracy. After all of them, a number of conclusions drawn from the research and suggestions are provided in this section.

7.1. Conclusions

A new PPP software package, called PPPH, was developed in the MATLAB[®] environment. PPPH is designed to process observations from GPS, GLONAS, Galileo, and BDS, and to provide multi-GNSS PPP solutions. PPPH includes five main components, which are data importing, preprocessing, modelling, filtering, and analysis. PPPH allows users to interfere each processing step of PPP through its user-friendly graphical user interface (GUI). To assess the performance of PPPH, 24-h observation data collected from 6 IGS stations during ten days between 10-14 May and 2-6 June 2015 were processed in static mode. The results indicated that the horizontal and vertical positioning errors taking IGS weekly solutions as the *ground truth* reached 1.7 and 3.5 cm at most, respectively. Additionally, 80% of the horizontal positioning errors and 55% of the vertical positioning errors were less than 1 cm, which demonstrated that PPPH provides centimetre-level positioning accuracy.

Additional investigation conducted to determine whether ionospheric variations affect the PPP models and algorithms. While the 5-days period between 10-14 May was moderately active in terms of ionospheric variation, the second 5-days period between 2-6 June 2015 was rather quiet. When the results of both two periods are compared, it was observed that there was no considerable difference between them in the sense of the positioning accuracy and convergence time. Therefore, it was concluded that the

models and algorithms of PPPH are not affected by the ionospheric variations.

In addition, a comparison between PPPH and online PPP services was made to validate the performance of PPPH. The same data set was processed with two of widely used online PPP services, namely CSRS-PPP developed by National Resources Canada (NRCan) and GAPS developed by University of New Brunswick (UNB). As a result, it was observed that the average positioning errors obtained from PPPH, GAPS, and CSRS-PPP do not exceed 2.6 cm. Moreover, 10 days average 3D positioning errors of PPPH, GAPS, and CSRS-PPP were found to be 1.6, 2.0 and 1.3 cm, respectively. Consequently, two online PPP services achieved the centimetre-level positioning accuracy as well as PPPH. From the point of positioning accuracy, PPPH is quite akin to online services. On the other hand, maximum convergence times were 39, 37 and 21 minutes for PPPH, GAPS, and CSRS-PPP processes, respectively. Further, the average convergence times of the whole stations were calculated as 28.8, 26.4, and 16.4 minutes for PPPH, CSRS-PPP, and GAPS solutions, respectively. It should be mentioned that the CSRS-PPP processes GLONASS satellites by default, which is thought to be the main reason for its better performance in terms of convergence time. Nevertheless, it can be concluded that the three solutions are comparable with each other.

Before evaluating the contribution of multi-GNSS to PPP performance, the satellite availability was analysed because PPP performance mainly depends on number and geometry of visible satellites. 24 hours observation data collected from 6 IGS stations during 2-6 June 2015 were processed in three different PPP processing modes; GPS-only, GPS/GLONASS PPP, and multi-GNSS. The inclusion of GLONASS improved the number of visible satellites by 70% relative to the GPS only solutions. Likewise, the addition of Galileo and BDS increased the number of visible satellites at the rate of 28% relative to the combination of GPS and GLONASS. Furthermore, it was noticed that Galileo and BDS significantly improved the number of visible satellites in the Asia-Pacific region. The reason for this is that BDS has additional Geostationary Earth Orbit (GEO) satellites in this region. Therefore, multi-GNSS PPP offers a considerable prospect to augment the PPP performance near Asia-Pacific region.

To evaluate the contribution of multi-GNSS to the PPP performance, 24 hours observation data collected from 6 MGEX stations during the days between 2-6 June 2015 was processed by restarting the process at every 3 hours. The processes again were performed under three different PPP scenarios; GPS-only, GPS/GLONASS, and multi-GNSS. The GPS/GLONASS PPP improved the positioning accuracy at the rate of 16.2% in comparison with the GPS-only PPP solutions in average. Similarly, relative to GPS-only PPP, the multi-GNSS PPP provided a 21.6% improvement in the

positioning accuracy. Moreover, the GPS/GLONASS PPP decreased the convergence time at a rate of 28.1% relative to the GPS-only PPP. In similar, the multi-GNSS PPP decreased the convergence time at the rate of 33.2%. This rate reached to 44.6% at the station NNOR located in the Asia-Pacific region. Consequently, multi-GNSS PPP improved the performance of PPP significantly relative to the GPS-only PPP, especially in the Asia-Pacific region.

Insufficient or wrong initial knowledge about estimated parameters and process dynamics not only degrade the accuracy of PPP estimates but also may lead to a failure of the convergence in the implementation of the Kalman filter on PPP. To overcome this problem, an innovative method introduced to obtain prior knowledge of system dynamics. This method involves the computation of both initial parameters and their covariances using least squares estimation. In order to evaluate the contribution of this approach, a data set including 48 samples was processed with both the standard initial parameters and a priori parameters acquired from least squares adjustment. Results show that although there is not any significant improvement with regard to the positioning accuracy, and new approach reduces convergence time by 15.8% in average with respect to the standard parametrization.

7.2. Recommendations

The recommendations for future works about this research are given as:

- Five agencies broadcast multi-GNSS precise products as a part of IGS MGEX project. A comparison can be performed to investigate the quality of these products and their influence on multi-GNSS PPP.
- Recently, several agencies have started to broadcast the precise orbit and clock products in real time. PPPH can be improved to support real-time applications.
- Integrating multi-GNSS improves not only the positioning accuracy but also the other estimates, such as tropospheric wet delay. Therefore, this research may be extended to estimate the atmospheric water vapor.
- In this research, the multi-GNSS PPP model includes the ambiguity-float solution. The contribution of multi-GNSS on ambiguity-fixed solutions can be investigated.
- It would be beneficial to present PPPH as a multi-GNSS PPP service via the internet for the GNSS community.

REFERENCES

- [1] Zumberge, J., Heflin, M., Jefferson, D., Watkins, M., Webb, F. Precise point positioning for the efficient and robust analysis of GPS data from large networks, *Journal of Geophysical Research*, 102(B3),5005:5017, **1997**.
- [2] Heroux, P., Kouba, J., GPS precise point positioning using IGS orbit products, *GPS Solutions*, 5:2, 12-28, **2001**.
- [3] Tu, R., Zhang, H., Ge, M., Huang, G., A real-time ionospheric model based on GNSS Precise Point Positioning, *Advances in Space Research*, 52, 1125-1134,**2013**.
- [4] Lu, C., Li, X., Nilsson, T., Heinkelmann, R., Ge, M., Glaser, S., Schuh, H., Real-time retrieval of precipitable water vapor from GPS and BeiDou observations, *Journal of Geodesy*, 89, 843-856,**2015**.
- [5] Yuan, X., Fu, J., Sun, H., Toth, C., The application of GPS precise point positioning technology in aerial triangulation, *ISPRS Journal of Photogrammetry and Remote Sensing*, 64, 541-550,**2009**.
- [6] Shi, J., Yuan, X., Cai, Y., Wang, G., GPS real-time precise point positioning for aerial triangulation, *GPS Solutions*, 21, 405-414,**2017**.
- [7] Wright, T. J., Houlie, N., Hildyard, M., Iwabuchi, T., Real-time, reliable magnitudes for large earthquakes from 1 Hz GPS precise point positioning: The 2011 Tohoku-Oki (Japan) earthquake, *Geophysical Research Letters*, 39, L12302, **2012**.
- [8] Li, X., Ge, M., Zhang, X., Zhang, Y., Guo, B., Wang, R., Klotz, J., Wickert, J., Real-time high-rate co-seismic displacement from ambiguity-fixed precise point positioning: Application to earthquake early warning, *Geophysical Research Letters*, 40, 295-300, **2013**.
- [9] Berber, M. M., Üstün, A., Yetkin, M., Static and kinematic PPP using online services: a case study in Florida, *Journal of Spatial Science*, **2017**.
- [10] Collins, P., Bisnath, S., Lahaye, F., Heroux, P., Undifferenced GPS ambiguity resolution using the decoupled clock model and ambiguity datum fixing, *Navigation*, 57(2), CA, 123-135, **2010**.
- [11] Ge, M., Gendt, G., Rothacker, M., Shi, C., Liu, J., Resolution of GPS carrier-phase ambiguities in precise point positioning (PPP) with daily observations, *Journal of Geodesy*, 82(7), 389:399, **2007**.

- [12] Laurichesse, D., Mercier, F., Bertias, J., Broca, P., Cerri, L., Integer ambiguity resolution on undifferenced GPS phase measurements and its applications to PPP and satellite precise orbit determination navigation, *Navigation*, 56(2), 135-149, **2009**.
- [13] Geng, J., Meng, X., Dodson, A. H., Ge, M., Teferle, F. N., Rapid re-convergences to ambiguity-fixed solutions in precise point positioning, *Journal of Geodesy*, 84(12), 705-714, **2010**.
- [14] Li, T., Wang, J., Laurichesse, D., Modeling and quality control for reliable precise point positioning integer ambiguity resolution with GNSS modernization, *GPS Solutions*, 18(3), 429-442, **2014**.
- [15] Shi, J., Gao, Y., A comparison of three PPP integer ambiguity resolution methods, *GPS Solutions*, 18, 519:528, **2014**.
- [16] Cai, C., Gao, Y., Modelling and assessment of combined GPS/GLONASS precise point positioning, *GPS Solutions*, 17, 223-236, **2013**.
- [17] Yigit, C. O., Gikas, V., Alcay, S., Ceylan, A., Performance evaluation of short to long term GPS, GLONASS and GPS/GLONASS post-processed PPP, *Survey Review*, 46(336), 155-166, **2014**.
- [18] Li, P., Zhang, X., Integrating GPS and GLONASS to accelerate convergence and initialization times of precise point positioning *GPS Solutions*, 18(3), 461-471, **2014**.
- [19] Tøgedor, J., Øvstedal, O., Vigen, E., Precise orbit determination and point positioning using GPS, Glonass, Galileo and BeiDou, *Journal of Geodetic Science*, 4, 65-73, **2014**.
- [20] Cai, C., Gao, Y., Pan, L., Zhu, J., Precise point positioning with quad-constellations: GPS, BeiDou, GLONASS and Galileo, *GPS Solutions, Advances in Space Research*, 56, 133-143, **2015**.
- [21] GPS Official Web Site, GPS Constellation, <http://www.gps.gov/>, February, **2017**.
- [22] Gakstatter, E., The Future of High-Precision GPS/GNSS Technology, *OR: GIS pro 2012*, October 3, Portland, USA, **2012**.
- [23] Global navigation satellite system GLONASS interface control document (Version 5.1), [http://facility.unavco.org/data/docs/ICD_GLONASS_5.1_\(2008\)_en.pdf](http://facility.unavco.org/data/docs/ICD_GLONASS_5.1_(2008)_en.pdf), February, **2017**.

- [24] European GNSS (GALILEO) open service interface control document (Version 1.3), https://www.gsc-europa.eu/sites/default/files/Galileo_OS_SIS_ICD_1.3.pdf, (February, **2017**).
- [25] China Satellite Navigation Office, Report on the Development of BeiDou Navigation Satellite System (Version 2.2), <http://www.beidou.gov.cn/attach/2013/12/26/20131226fed336adf2184d52843d5bf81832e82c.pdf>, February, **2017**.
- [26] BeiDou Navigation Satellite System Signal In Space Interface Control Document (Version 2.1), <http://www.beidou.gov.cn/attach/2016/11/07/21212.pdf>, March, **2017**.
- [27] NAVSTAR GPS Space Segment/Navigaton User Segment Interface, http://www.gps.gov/technical/icwg/IRN-IS-200H-001+002+003_rollup.pdf, **2015**.
- [28] Gendt, G., Altamimi, Z., Dach, R., Söhne, W., Springer, T., The GGSP Prototype Team, GGSP: Realisation and maintenance of the Galileo Terrestrial Reference Frame, *Advances in Space Research*, 47,174-185, **2011**.
- [29] Montenbruck, O., Steinberger, P., Prange, L., Deng, Z., Zhao, Q., Perosanz, F., Romero, I., Coll, C., Stürze, A., Weber, G., Schmid, R., MacLeod, K., Schaer, S., The Multi-GNSS Experiment (MGEX) of the International GNSS Service (IGS) – Achievements, prospects and challenges, *Advances in Space Research*, 59 ,1671-1697, **2017**.
- [30] Subirana, J. S., Zornoza, J. M. J., Hernández-Pajares, M., *GNSS Data Processing, Vol. I: Fundamentals and Algorithms*, ESA, Leiden, **2013**.
- [31] Hofmann-Wellenhof, B., Lichtenegger, H., Wasle, E., *GNSS – Global Navigation Satellite Systems*, Springer, New York, **2008**.
- [32] Hatch, R., The synergism of GPS code and carrier measurements, *In: Proceedings of the third international symposium on satellite Doppler positioning at Physical Sciences of New Mexico State University*, Vol 2, 1213-1231, **1982**.
- [33] Melbourne, W.G., The case for ranging in GPS-based geodetic systems, *Proceedings of the first international symposium on precise positioning with the GPS*, 15-19 April, Rockville, **1985**.
- [34] Wübbena, G., Software developments for geodetic positioning with GPS using TI-4100 code and carrier measurements, *Proceedings of the first international symposium on precise positioning with the GPS*, 15-19 April, Rockville, **1985**.
- [35] Seepersad, G., Bisnath, S., Challenges in assessing PPP performance, *Journal of Applied Geodesy*, 8, 205-222, **2014**.

- [36] IGS Official Web Site, Products, <http://www.igs.org/products> (February, 2017).
- [37] Guo, F., Zhang, X., Real-time clock jump compensation for precise point positioning, *GPS Solutions*, 18, 41-50, 2014.
- [38] Hopfield, H. S., Two-quartic tropospheric refractivity profile for correcting satellite data, *Journal of Geophysical Research*, 74, 4487-4499, 1969.
- [39] Saastamoinen, J., Contributions to the theory of atmospheric refraction, *Bulletin Géodésique*, 107, 13-34, 1973.
- [40] Boehm, J., R. Heinkelmann, H. Schuh, Short Note: A global model of pressure and temperature for geodetic applications, *Journal of Geodesy*, 81, 679–683, 2007.
- [41] Lagler, K., Schindelegger, M., Boehm, J., Krasna, H., Nilsson, T., GPT2: Empirical slant delay model for radio space geodetic techniques, *Geophysical Research Letters*, 40, 1069-1073, 2013.
- [42] Niell, A. E., Global mapping functions for the atmosphere delay at radio wavelengths, *Journal of Geophysical Research*, 101 (B2), 3227-3246, 1996.
- [43] Boehm, J., Schuh, H., Vienna mapping functions in VLBI analyses, *Geophysical Research Letters*, 31, L01603, 2004.
- [44] Boehm, J., Niell, A., Tregoning, P., Schuh, H., Global Mapping Function (GMF): A new empirical mapping function based on numerical weather model data, *Geophysical Research Letters*, 33, L07304, 2006.
- [45] Boehm, J., Werl, B., Schuh, H., Troposphere mapping functions for GPS and very long baseline interferometry from European Centre for Medium-Range Weather Forecasts operational analysis data, *Journal of Geophysical Research*, 111, B02406, 2006.
- [46] Seeber, G., *Satellite Geodesy*, Berlin, New York, 2003.
- [47] Kouba, J., A guide to using International GNSS Service (IGS) products, <http://kb.igs.org/hc/en-us/articles/201271873-A-Guide-to-Using-the-IGS-Products>, 2015.
- [48] Bar-Sever, Y.E., A new model for GPS yaw attitude, *Journal of Geodesy*, 70:11, 714-723, 1996.
- [49] Montenbruck, O., Schmid, R., Mercier, F., Steinberger, P., Noll, C., Fatkulin, R., Kogure, S., Ganeshan, A.S., GNSS satellite geometry and attitude models, *Advances in Space Research*, 56, 1015-1029, 2015.

- [50] Schmid, R., Dach, R., Collilieux, X., Jäggi, A., Schmitz, M., Dilssner, F., Absolute IGS antenna phase center model igs08.atx: status and potential improvements, *Journal of Geodesy*, 90, 343-364, **2016**.
- [51] Wu, J., Wu, S., Hajj, G., Bertiger, W., Liechten, S., Effects of antenna orientation on GPS carrier phase, *Manuscripta Geodaetica*, 18, 91-98, **1993**.
- [52] Wahr, J., The forced nutation of an elliptical, rotating, elastic, and ocean less Earth, *Geophysical Journal of the Royal Astronomical Society*, 64, 705-727, **1981**.
- [53] Petit, G., Luzum, B., *IERS Conventions 2010*, Technical Note No. 36, <http://www.iers.org/TN36/>, Frankfurt, **2010**.
- [54] Montenbruck, O., Hauschild, A., Code biases in multi-GNSS point positioning, *In: ION ITM 2013*, pp, 616-628, **2013**.
- [55] Schaer, S.,) Overview of GNSS biases, In: Proceedings of IGS Workshop on GNSS Biases, University of Bern, Switzerland, **2012**.
- [56] Liu, Z., A new automated cycle slip detection and repair method for a single dual-frequency GPS receiver, *Journal of Geodesy*, 85, 171-183, **2011**.
- [57] Deo, M., El-Mowafy, A., Cycle Slip and Clock Jump Repair with Multi-Frequency Multi-Constellation GNSS data for Precise Point Positioning, *International Global Navigation Satellite Systems Society Symposium*, 14-16 July, Outrigger Gold Coast, Qld Australia, **2015**.
- [58] Mohinder, S. G., Lawrence, R. W., Angus, P. A., *Global Positioning Systems, Inertial Navigation, and Integration*, John Wiley & Sons, New Jersey, **2007**.
- [59] Kalman, R. E., A New Approach to Linear Filtering and Prediction Problems, *Transactions of the ASME*, 82, 36-45, **1960**.
- [60] Gelb, A., *Applied Optimal Estimation*, MIT Press, Cambridge, **1974**.
- [61] Mikhail, E. M., Ackermann, F., *Observation and Least Square*, IEP-A Dun-Donnelley Publisher, New York, **1976**.
- [62] Welch, G., Bishop, G., An introduction to the Kalman Filter, TR 95-401, University of North Carolina at Chapel Hill, Chapel Hill, NC 27599-3175, **1995**.
- [63] Bucy, R. S., Joseph, P. D., *Filtering for Stochastic Processes, with Applications to Guidance*, Wiley, New York, **1986**.
- [64] Witchayangkoon, B., Elements of GPS Precise Point Positioning, Ph.D. Thesis, University of Maine, **2000**.

- [65] Abdel-Salam, M. A., *Precise Point Positioning using un-differenced code and carrier phase observations*, Ph.D. Thesis, University of Calgary, **2005**.
- [66] Cai, C., Gao, Y., Pan, L., Zhu, J., Precise point positioning with quad-constellations: GPS, BeiDou, GLONASS and Galileo, *Advances in Space Research*, 56, 135-143, **2015**.
- [67] Teunissen, P. J. G., Salzmann, M. A., *Performance Analysis of Kalman Filters*, Reports 88.2, Delft University of Technology, Netherlands, **1988**.
- [68] Wanninger, L., Carrier-phase inter-frequency biases of GLONASS receivers, *Journal of Geodesy*, 86(2), 139-148, **2011**.
- [69] Zhao, X., Wang, S., Liu, C., Ou, J., Yu, X., Assessing the performance of multi-GNSS precise point positioning in Asia-Pacific region, *Survey Review*, 49, 186-196, **2017**.
- [70] Yang, Y., He, H., Xu, G., Adaptively robust filtering for kinematic geodetic positioning, *Journal of Geodesy*, 75, 109-116, **2001**.
- [71] Yang, Y., Song, L., Xu, T., Robust estimator for correlated observations based on bifactor equivalent weights, *Journal of Geodesy*, 76, 353-358, **2002**.
- [72] Guo, F., Zhang, X., Adaptive robust Kalman filtering for precise point positioning, *Measurement Science and Technology*, 25, 105011, **2014**.
- [73] Ding, W., Wang, J., Rizos, C., Improving adaptive Kalman estimation in GPS/INS integration, *Journal of Navigation* **2007**.
- [74] Yao, Y., Gao, J., Li, Z., Xu, C., Cao, X., A new robust Kalman filtering algorithm of unequal precision observations based on residual vectors in static Precise Point Positioning, *Acta Geodynamica et Geomaterialia*, 4(184), 397-408, **2016**.
- [75] Michel, F. C., Kp as a planetary index, *Journal of Geophysical Research*, 69(19), 4182-4183, **1964**.
- [76] Choy, S., Bisnath, S., Rizos, C., Uncovering common misconceptions in GNSS Precise Point Positioning and its future prospect, *GPS Solutions*, 21, 13-22, **2017**.
- [77] Ghoddousi-Fard, R., Dare, P., Online GPS processing services: an initial study, *GPS Solutions*, 10, 12-20, **2006**.
- [78] Tsakiri, M., GPS Processing Using Online Services, *Journal of Surveying Engineering*, 134(4), 115-125, **2008**.

- [79] El-Mowafy, A., Analysis of Web-Based GNSS Post Processing Services for Static and Kinematic Positioning Using Short Data Spans, *Survey Review*, 43:323, 535-549, **2011**.
- [80] Yigit, C. O., Experimental assessment of post processed kinematic Precise Point Positioning method for structural health monitoring, *Geomatics, Natural Hazards and Risk*, 7:1, 360-383, **2016**.
- [81] Wang, G., Soler, T., Using OPUS for Measuring Vertical Displacements in Houston, Texas, *Journal of Surveying Engineering*, 139(3), 126-134, **2013**.
- [82] Alkan, R. M., Ocalan. T., Usability of the GPS Precise Point Positioning Technique in Marine Applications, *Journal of Navigation*, 66, 579-588, **2013**.
- [83] Martin, A., Anquela, A. B., Capilla, R., Berne, J. L., PPP Technique Analysis Based on Time Convergence, Repeatability, IGS Products, Different Software Processing, and GPS+GLONASS Constellation, *Journal of Surveying Engineering*, 137(3): 99-108, **2011**.

CURRICULUM VITAE

Credentials

Name, Surname : Berkay Bahadur
Place of Birth : Yenimahalle/Ankara
Marital Status : Married
E-mail : berkaybahadur@hacettepe.edu.tr
Address : Geomatics Engineering Department of Hacettepe University,
Beytepe/ANKARA

Education

High School : Selçuklu Anatolian High School, Ankara, 2006.
BSc. : Selçuk University, Geomatics Engineering, Konya, 2013.
MSc. : -
PhD. : -

Foreign Languages

English (fluent)

Work Experience

Control Engineer BCT Engineering and Consultancy 2013-2014
Research Assistant Hacettepe University 2014-...

Areas of Experiences

Geodesy, Global Navigation Satellite Systems (GNSS), Multi-GNSS Integration,
Precise Point Positioning (PPP), Matlab Programming

Projects and Budgets

-

Publications

Bahadur, B., Üstün, A., Internet Based GNSS Processing Services, *Harita Dergisi*, 152:40-50, **2014**.

Oral and Poster Presentations

-



HACETTEPE UNIVERSITY
GRADUATE SCHOOL OF SCIENCE AND ENGINEERING
THESIS/DISSERTATION ORIGINALITY REPORT

HACETTEPE UNIVERSITY
GRADUATE SCHOOL OF SCIENCE AND ENGINEERING
TO THE DEPARTMENT OF GEOMATICS ENGINEERING

Date: 11/07/2017

Thesis Title / Topic: IMPROVING THE PERFORMANCE OF PRECISE POINT POSITIONING WITH MULTI-GNSS

According to the originality report obtained by myself/my thesis advisor by using the *Turnitin* plagiarism detection software and by applying the filtering options stated below on 11/07/2017 for the total of 89 pages including the a) Title Page, b) Introduction, c) Main Chapters, d) Conclusion sections of my thesis entitled as above, the similarity index of my thesis is 10 %.

Filtering options applied:

1. Bibliography/Works Cited excluded
2. Quotes excluded
3. Match size up to 5 words excluded

I declare that I have carefully read Hacettepe University Graduate School of Science and Engineering Guidelines for Obtaining and Using Thesis Originality Reports; that according to the maximum similarity index values specified in the Guidelines, my thesis does not include any form of plagiarism; that in any future detection of possible infringement of the regulations I accept all legal responsibility; and that all the information I have provided is correct to the best of my knowledge.

I respectfully submit this for approval.

11/07/2017

Name Surname: Berkay Bahadur
Student No: N14129754
Department: Geomatics Engineering
Program: Geomatics Engineering
Status: Masters Ph.D. Integrated Ph.D.

ADVISOR APPROVAL

APPROVED.

Asst. Prof. Dr. Metin Nohutcu

